Western Graduate&PostdoctoralStudies

Western University
Scholarship@Western

Electronic Thesis and Dissertation Repository

1-17-2013 12:00 AM

X-ray Absorption Fine Structure and X-ray Excited Optical Luminescence Studies of Gallium Nitride - Zinc Oxide Solid Solution Nanostructures

Matthew J. Ward, *The University of Western Ontario*

Supervisor: Dr. Tsun-Kong Sham, *The University of Western Ontario*

A thesis submitted in partial fulfillment of the requirements for the Doctor of Philosophy degree in Chemistry

© Matthew J. Ward 2013

Follow this and additional works at: https://ir.lib.uwo.ca/etd

Part of the Physical Chemistry Commons

Recommended Citation

Ward, Matthew J., "X-ray Absorption Fine Structure and X-ray Excited Optical Luminescence Studies of Gallium Nitride - Zinc Oxide Solid Solution Nanostructures" (2013). *Electronic Thesis and Dissertation Repository*. 1081.
https://ir.lib.uwo.ca/etd/1081

This Dissertation/Thesis is brought to you for free and open access by Scholarship@Western. It has been accepted for inclusion in Electronic Thesis and Dissertation Repository by an authorized administrator of Scholarship@Western. For more information, please contact wlswadmin@uwo.ca.

X-RAY ABSORPTION FINE STRUCTURE AND X-RAY EXCITED OPTICAL LUMINESCENCE STUDIES OF GALLIUM NITRIDE – ZINC OXIDE SOLID SOLUTION NANOSTRUCTURES

(Spine title: XAFS AND XEOL STUDIES OF GaN – ZnO SOLID SOLUTION NANOSTRUCTURES)

(Thesis format: Integrated Article)

by

Matthew James Ward

Graduate Program in Chemistry

A thesis submitted in partial fulfillment
of the requirements for the degree of
Doctor of Philosophy

The School of Graduate and Postdoctoral Studies
The University of Western Ontario
London, Ontario, Canada

© Matthew James Ward 2013

THE UNIVERSITY OF WESTERN ONTARIO
School of Graduate and Postdoctoral Studies

CERTIFICATE OF EXAMINATION

Supervisor

_____
Dr. Tsun-Kong Sham

Supervisory Committee

_____

_____

Examiners

_____
Dr. David Shoesmith

_____
Dr. Oleg Semenikhin

_____
Dr. Mahi Singh

_____
Dr. Arthur Mar

The thesis by

Matthew James Ward

entitled:

X-ray Absorption Fine Structure and X-ray Excited Optical Luminescence Studies of Gallium Nitride – Zinc Oxide Solid Solution Nanostructures

is accepted in partial fulfillment of the
requirements for the degree of
Doctor of Philosophy

_____
Date

_____
Chair of the Thesis Examination Board

Abstract

Gallium nitride – zinc oxide (GaN-ZnO) solid solutions have been realized as potential photocatalysts for overall water splitting due to a narrowing of the band-gap into the visible region of the solar spectrum. Although there has been much experimental and theoretical work on this novel class of semiconductors many questions about the nature of their electronic and chemical properties remain unanswered. In particular the mechanism of band-gap reduction in these materials is not clearly understood. It is also unclear what the local chemical environment of gallium, zinc, nitrogen, and oxygen is in both the surface and bulk of these solid solutions. These materials have unusual optical emission properties exhibiting broad visible emission bands that are substantially red-shifted from observed band-gap energies. Since crystallinity, electronic structure, defects, and local chemical environments (both bulk and surface) all affect photocatalytic efficiency further understanding of the aforementioned properties of these materials is necessary.

The focus of this thesis is on the analysis of GaN-ZnO nanostructures by X-ray absorption fine structure (XAFS), including the near edge region, X-ray absorption near edge structure (XANES) and the extended region, extended X-ray absorption fine structure (EXAFS) to further the understanding of the local chemical environment (both bulk and surface) and structure of these materials using tunable X-rays from a synchrotron light source. X-ray excited optical luminescence (XEOL) has also been used to study the optical emission and near-band-gap (NBG) properties of these materials.

From XANES it has been shown that there is local chemical disorder of gallium nitride and zinc oxide phases upon solid solution formation, but, there is also strong short-range order which is evident in the EXAFS. XEOL studies have revealed that optical luminescence observed from these materials is of complex origins including zinc-related acceptor levels in the bulk and defects in the complex surface oxide. Preliminary results from time-resolved XEOL experiments have provided evidence of two NBG emission components related to GaN and ZnO phases in the material respectively. These results suggest that band-gap reduction observed in these materials is due to repulsion between conduction band onsets at phase interfaces within a disordered solid solution.

Keywords

X-ray absorption near edge structure, extended X-ray absorption fine structure, X-ray excited optical luminescence, time-resolved X-ray excited optical luminescence, two-dimensional X-ray absorption fine structure – X-ray excited optical luminescence, gallium nitride – zinc oxide solid solutions, gallium nitride – zinc oxide nanostructures, optical streak camera

Co-Authorship Statement

This thesis contains both material from previously published manuscripts and unpublished results. Dr. Tsun-Kong Sham is a co-author on all published papers and unpublished chapters presented in this thesis. With the exception of chapter 3, which will be addressed below, M. J. Ward wrote the first draft of the manuscript presented in each chapter, and Tsun-Kong Sham played a major role in the editing and revisions of the contents.

Ward obtained all of the X-ray absorption near edge structure (XANES), extended X-ray absorption fine structure (EXAFS), and X-ray excited optical luminescence (XEOL) data presented in this thesis, and was responsible for all of the subsequent data processing and analysis.

The first draft of chapter three was collaboratively written by Dr. Wei-Qiang Han of the Center for Functional Nanomaterials (CFN), Brookhaven National Laboratory, and M. J. Ward. Dr. Han was responsible for synthesis and conventional analysis, including scanning electron microscopy (SEM), transmission electron microscopy (TEM), X-ray diffraction (XRD), and UV-visible (UV-vis) diffuse reflectance spectroscopy, of the gallium nitride – zinc oxide solid solution (GaN-ZnO) nanostructures studied in this manuscript. M. J. Ward was responsible for all X-ray absorption and X-ray excited optical luminescence measurements in this manuscript. Writing was done collaboratively with Dr. Han responsible for writing the introduction, synthesis, and conventional characterization sections and M. J. Ward responsible for writing XANES and XEOL sections. Discussion of experimental findings was written by both authors. All authors were responsible for editing and revision of the final manuscript.

All experimental X-ray absorption and XEOL data for the manuscript in chapter 4 was collected by M. J. Ward. SEM images were provided by Dr. Han (CFN). Ward wrote the first draft of chapter 4 and subsequent editing was done by all authors. Final revision of the manuscript was done by Ward. In chapter 5 synthesis and conventional characterization of GaN-ZnO solid solution nanocrystals was performed by Dr. Han (CFN). Ward wrote the first draft of the manuscript presented in chapter 5. In chapter 6 Ward and Dr. Tom Regier of the

Canadian Light Source (CLS) collected time-resolved (TR) XEOL data used in this manuscript. Dr. Johannes Vogt (CLS) provided technical details of timing electronics and bunch cleaning in chapter 6. The GaN-ZnO nanoparticle sample for chapter 6 was provided by Dr. Han (CFN). Ward wrote the first draft of the manuscript in part I of chapter 6, development of the optical streak camera technique, and it was edited by all co-authors. Ward wrote the first draft of part II of chapter 6. Technical support with XANES, EXAFS, and XEOL was provided by the following individuals: Tom Regier and David Chevrier for experiments conducted at the Spherical Grating Monochromator (SGM) beam-line at the CLS, Robert Gordon for experiments conducted at the Pacific Northwest Consortium – X-ray Sciences Division (PNC/XSD) beam-line 20-BM at the Advanced Photon Source (APS), and Tom Regier, David Chevrier, and Johannes Vogt for time-resolved XEOL experiments performed at the SGM beam-line of the CLS.

To Alaura and Skylyn

Acknowledgments

First I would like to thank Dr. Tsun-Kong Sham for his supervision, support, and encouragement, without which my graduate studies would not have been possible. I am grateful for having had the opportunity to work under someone who is an expert in the field of synchrotron X-ray absorption spectroscopy, and is also well liked and respected by many of his peers and colleagues. His excitement and enthusiasm about research are something I will always remember and admire.

I would also like to thank Dr. Wei-Qiang Han of the Center for Functional Nanomaterials (CFN) at Brookhaven National Laboratory for providing me with exciting novel materials for X-ray absorption studies presented in this thesis. I am also very thankful for the time I spent at the CFN under the supervision of Dr. Han; he was a very knowledgeable and gracious host.

I would also like to thank my collaborators, Dr. Wei-Qiang Han, Dr. Tom Regier, Dr. Johannes Vogt, and Dr. Robert Gordon, for all of their input and helpful discussions.

Additionally, I am very grateful for all of the technical support I received at synchrotron facilities from: Tom Regier (CLS), David Chevrier (CLS), Johannes Vogt (CLS), Dale Brewe (APS), and Robert Gordon (PNC/APS). Their immense level of expertise, enthusiasm, and professionalism made my experiences at these facilities much more enjoyable.

I would also like to thank members of Dr. Sham's research group, both past and present, Dr. Lijia Liu, Dr. Michael Murphy, Dr. J. Y. Peter Ko, Dr. Yun-Mui Yiu, Dr. Zhiqiang Wang, Dr. Yongji Tang, Dr. Yuanhong (Terry) Tang, Mr. Dongniu (David) Wang, Mr. Xiaoxuan (Vince) Guo, Mr. Ankang Zhao, Mrs. Olga Lobacheva, Mr. Fuyan Zhao, and Ms. Dong Zhao for all of their helpful discussions and feedback. In particular I would like to thank Dr. Lijia Liu, Dr. Michael Murphy, and Dr. J. Y. Peter Ko for their companionship and camaraderie on many research trips to synchrotron facilities, without you the long hours at the beam-line would have not been as enjoyable.

Synchrotron research was carried out at the Canadian Light Source (CLS) and PNC/XSD at the Advanced Photon Source (APS). Research at CLS is supported by NSERC,

NRC, CIHR, and the University of Saskatchewan. PNC/XSD at the APS, and research at these facilities, is supported by the US DOE - Basic Energy Sciences, NSERC, the University of Washington, Simon Fraser University and the Advanced Photon Source. Use of the Advanced Photon Source is also supported by the US DOE, Office of Science, Office of Basic Energy Sciences, under Contract DE-AC02-06CH11357. Research at UWO is supported by NSERC, CRC, CFI, and OIT. Part of this research was carried out at the Center for Functional Nanomaterials, Brookhaven National Laboratory, which is supported by the U.S. Department of Energy, Office of Basic Energy Sciences, under Contract No. DE-AC02-98CH10886. MJW acknowledges the financial support of the Ontario Graduate Scholarship (OGS) and the Queen Elizabeth II Graduate Scholarship in Science and Technology (QEIIGSST) programs and the ASPIRE and Graduate Thesis Research Award (GTRA) programs of The University of Western Ontario (UWO).

I would like to thank my parents, family, and friends for all of their support and encouragement, without which I would not be where I am today.

Finally I would like to thank my wife Alaura for all of her support, encouragement, and love, without which the completion of my Ph.D. would not have been possible.

Table of Contents

CERTIFICATE OF EXAMINATION ii

Abstract iii

Co-Authorship Statement v

Dedication vii

Acknowledgments viii

Table of Contents x

List of Tables xv

List of Figures xvi

List of Abbreviations xxii

List of Appendices xxv

Chapter 1 1

1 Introduction 1

1.1 Overall Water Splitting Under Visible Light 1

1.2 Gallium Nitride – Zinc Oxide Solid Solutions for Overall Water Splitting Under Visible Light 5

1.3 Objective and Arrangement of Thesis 26

1.4 References 28

Chapter 2 32

2 Introduction to Synchrotron Radiation Spectroscopy 32

2.1 Synchrotron Radiation and Synchrotron Light Sources 32

2.1.1 Synchrotron Radiation 32

2.1.2 Synchrotron Light Sources 34

2.2 X-ray Absorption Spectroscopy 37

2.2.1 X-ray Absorption Near Edge Structure (XANES) 40

2.2.2 Extended X-ray Absorption Fine Structure (EXAFS) 42

2.2.3 De-excitation Processes 46

2.2.4 X-ray Excited Optical Luminescence (XEOL) 48

2.3 Synchrotron Facilities 52

2.3.1 Canadian Light Source (CLS) 52

2.3.2 Advanced Photon Source (APS) 53

2.4 Beam-lines 54

2.4.1 Spherical Grating Monochromator (SGM) Beam-Line 54

2.4.2 Pacific Northwest Consortium – X-ray Sciences Division (PNC/XSD) Beam-Line 20-BM 56

2.5 Detection Modes 57

2.6 References 59

Chapter 3 61

3 Soft X-ray XANES and XEOL Study of Indium Doped $Ga_{1-x}Zn_xN_{1-x}O_x$ Ultra-thin Nanosheets 61

3.1 Introduction 61

3.2 Experimental 63

3.2.1 Synthesis of indium doped $Ga_{1-x}Zn_xN_{1-x}O_x$ ultra-thin nanosheets 63

3.2.2 Conventional Characterization 63

3.2.3 Synchrotron Radiation Spectroscopy 64

3.3 Results and Discussion 64

3.3.1 XRD, SEM, TEM, and UV-vis diffuse reflectance 64

3.3.2 XANES 68

3.3.3 XEOL 72

3.4 Conclusions 76

3.5 References 78

Chapter 4 80

4 2D XAFS–XEOL Mapping of $Ga_{1-x}Zn_xN_{1-x}O_x$ Nanostructured Solid Solutions 80

4.1 Introduction 80

4.2 Experimental 83

4.2.1 Synthesis 83

4.2.2 2D XAFS–XEOL Spectroscopy 84

4.2.3 XANES and EXAFS Spectroscopy 84

4.3 Results and Discussion 85

4.3.1 2D XAFS–XEOL of GZNO 85

4.3.2 2D XAFS-XEOL of GIZNO 88

4.3.3 Zn, Ga, and In *K*-edge XANES of GZNO and GIZNO 89

4.3.4 In *K*-edge EXAFS of GIZNO 94

4.4 Conclusions 96

4.5 References 98

Chapter 5 100

5 Effects of Nitridation Temperature on $Ga_{1-x}Zn_xN_{1-x}O_x$ Solid Solution Nanocrystal Growth: An XAFS and XEOL Study 100

5.1 Introduction 100

5.2 Experimental 102

5.2.1 Synthesis 102

5.2.2 Synchrotron Radiation Spectroscopy 102

5.3 Results and Discussion 103

5.3.1 TEM, XRD, and UV-Vis diffuse reflectance of $Ga_{1-x}Zn_xN_{1-x}O_x$ Nanocrystals 103

5.3.2 Zinc and Gallium *K*-edge XANES 106

5.3.3 Zinc and Gallium *K*-edge EXAFS 110

5.3.4 Zinc and Gallium $L_{3,2}$-edge XANES 112

5.3.5 Nitrogen and Oxygen *K*-edge XANES 115

5.3.6 XEOL 117

5.4 Conclusion 119

5.5 References 122

Chapter 6 125

6 Time Resolved X-ray Excited Optical Luminescence (TR-XEOL) of $Ga_{1-x}Zn_xN_{1-x}O_x$ Nanoparticles Using an Optical Streak Camera 125

6.1 Introduction 125

6.2 Part I: Development of Optical Streak Camera TR-XEOL Technique 126

6.3 Part II: TR-XEOL Study of $Ga_{1-x}Zn_xN_{1-x}O_x$ Nanoparticles 129

6.3.1 Experimental 129

6.3.2 Results and Discussion 130

6.4 Conclusions 140

6.5 References 142

Chapter 7 144

7 Summary, Conclusions, and Future Directions 144

7.1 Summary 144

7.2 Conclusions 144

7.2.1 Local Chemical Environment 145

7.2.2 Electronic Structure 146

7.2.3 Surface Composition 147

7.2.4 Origin of Band-Gap Narrowing 148

7.2.5 General Conclusions 149

7.3 Future Directions 149

7.4 References 151

Appendices 152

Appendix A: Copyright Release for Chapter 3 from the American Chemical Society .. 152

Appendix B: Copyright Release for Chapter 4 from the American Chemical Society .. 153

Appendix C: Copyright Release for Chapter 6 from the Institute of Physics..... 154

Curriculum Vitae 156

List of Tables

Table 6-1 Representative XEOL decay lifetime fitting results for GZNO collected using an excitation energy above the N and O *K*-edges and the Zn and Ga L_3-edges with integration windows centered on the 471 nm (fast) and 512 nm (slow) emission bands. 138

List of Figures

Figure 1-1 General processes in semiconductor photocatalytic water splitting; (a) photon with energy greater than band-gap is absorbed creating hole in VB and electron in CB, (b) electrons and holes separate and migrate to surface, (c) electrons and holes reduce and oxidize water to produce H_2 and O_2, (d) electrons and holes recombine suppressing catalytic activity..... 2

Figure 1-2 Intermediate band-gap formed when wide-gap and narrow-gap semiconductors alloy to form a solid solution. 5

Figure 1-3 Band-gap narrowing and band-edge position in GaN-ZnO solid solutions. 6

Figure 2-1 Schematic of a (a) Bending magnet, (b) Wiggler, and (c) Undulator. 32

Figure 2-2 Opening angle and flux (vs. E_{photon}) of (a) bending magnets, (b) wigglers, and (c) undulators..... 34

Figure 2-3 Layout of typical synchrotron facility. 35

Figure 2-4 Log-log plot of the mass photoabsorption coefficient σ of platinum as a function of X-ray photon energy. 38

Figure 2-5 (a) X-ray absorption in a single atom system, and (b) X-ray absorption fine structure (XAFS) in a multi-atom system. 39

Figure 2-6 Multiple scattering process, where *n* represents the number of atoms in each scattering pathway χ_n. 41

Figure 2-7 (a) Ga *K*-edge XAFS of GaN. (b) k^2-weighted (black line) and k^3-weighted (red dashed line). 43

Figure 2-8 X-ray excitation of a core-level electron and subsequent de-excitation processes: (a) photoionization of a core-level electron producing a photoelectron and core-hole; core-hole decay (b) producing fluorescent X-rays, (c) Auger electrons, and (d) secondary electrons. 46

Figure 2-9 Diagram of electron-hole pair formation and radiative recombination processes. (a) Core-level electron is excited by X-ray photon with subseqent electron-hole thermalization. (b) Examples of radiative recombination; (i) direct recombination, (ii) indirect (i.e. phonon assisted, $\Delta k \neq 0$) recombination, and (iii) defect (i.e. traps, vacancies, impurities, etc.) recombination. 49

Figure 2-10 Schematic of a TR-XEOL experiment. 51

Figure 2-11 Counts vs. time decay curve of X-ray excited optical luminescence in a TR-XEOL experiment. 52

Figure 2-12 Layout of the Canadian Light Source. 53

Figure 2-13 Layout of the Advanced Photon Source. 54

Figure 2-14 Optical layout of SGM beam-line at CLS. 55

Figure 2-15 Optical layout of PNC/XSD beam-line 20-BM at APS. 56

Figure 2-16 Detection modes for XAFS; (a) transmission, (b) fluorescence yield (FY) and total electron yield (TEY), and (c) photoluminescence yield (PLY). 57

Figure 3-1 (a) XRD spectrum of the GIZNO nanosheets. (b) SEM image of the GIZNO nanosheets. 64

Figure 3-2 (a) Low-magnification TEM image of a large GIZNO nanosheet; (b) the corresponding electron-diffraction patterns from a large area indexed to a single-crystalline hexagonal-wurtzite phase; (c) high-magnification TEM image from the area enclosed by the square in Figure 3-2 (a); (d) high-magnification image of a nine-layered nanosheet, 2.3 nm thick; (e) EDS spectrum; (f) UV-vis diffuse reflectance spectrum. 65

Figure 3-3 GZNO sample: (a) XRD spectrum; (b) SEM image; (c) EDS spectrum; (d) UV-vis diffuse reflectance spectrum. 67

Figure 3-4 GZNO and GIZNO XANES at the (a) zinc and (b) gallium $L_{3,2}$-edges. 69

Figure 3-5 GZNO and GIZNO XANES at the (a) nitrogen and (b) oxygen *K*-edge. 70

Figure 3-6 Indium M_2-edge XANES of GIZNO..... 71

Figure 3-7 Zinc L_3-edge threshold energy (E_0) aligned to gallium L_3-edge (a) GIZNO; (b) GZNO. 72

Figure 3-8 XEOL of GZNO: (a) across the nitrogen and oxygen *K*-edges; (b) across the zinc and gallium $L_{3,2}$-edges; (c) fine structure..... 73

Figure 3-9 XEOL of GIZNO: (a) across the nitrogen and oxygen *K*-edges; (b) across the indium $M_{3,2}$-edges; (c) across the zinc and gallium $L_{3,2}$-edges..... 75

Figure 3-10 Oxygen *K*-edge XANES of GZNO and GIZNO..... 76

Figure 4-1 SEM of (a) GZNO nanoparticles and (b) GIZNO nanosheets..... 81

Figure 4-2 GZNO XAFS–XEOL: a) 2D XAFS-XEOL scan across N and O *K*-edges, TEY overlaid on scan (blue), black horizontal line denotes the window where optical-XAFS were collected. b) Wavelength window selected PLY (red) vs TEY across N and O *K*-edges. c) 2D XAFS-XEOL scan across Zn and Ga $L_{3,2}$-edge, TEY overlaid on scan (blue). d) Wavelength window selected PLY (red) vs TEY across Zn and Ga $L_{3,2}$-edges. 85

Figure 4-3 XEOL cuts taken across (a) N and O *K* and (b) Zn and Ga $L_{3,2}$ edges of GZNO. 87

Figure 4-4 GIZNO XAFS–XEOL results: a) 2D XAFS–XEOL scan across N and O *K*-edges, TEY overlaid on scan (red), black horizontal line denotes the window where optical-XAFS were collected; b) PLY (black) vs TEY across N and O *K*-edges; c) 2D XAFS–XEOL scan across In $M_{3,2}$-edges, TEY overlaid on scan (light blue); d) PLY (black) vs TEY across In $M_{3,2}$-edges; e) 2D XAFS–XEOL scan across Zn and Ga $L_{3,2}$-edges, TEY overlaid on scan (red); f) PLY (black) vs TEY across Zn and Ga $L_{3,2}$-edges..... 88

Figure 4-5 XEOL cuts taken across N and O *K* (a) and Zn and Ga $L_{3,2}$ (b) edges of GIZNO respectively. 89

Figure 4-6 GZNO and GIZNO XANES at the Zn (a) and Ga (b) *K*-edge..... 91

Figure 4-7 GZNO and GIZNO E_0 set to 0 eV: (a) Zn *K*-edge, near edge region;vertical line a and d marks the energy position of the first and second resonance of ZnO, respectively; vertical line b and c marks the second resonance of GaN, and GZNO and GIZNO respectively (b) Ga *K*-edge, near-edge region; vertical dashed line denotes the position of the multiple scattering resonance. 91

Figure 4-8 GIZNO In *K*-edge: (a) GIZNO, In_2O_3, and InN; (b) GIZNO and reference standards, E_0 set to 0 eV. 92

Figure 4-9 GIZNO In *K*-edge EXAFS: (a) in *k*-space, *k* weighted; (b) in *R* space, k^3 weighted. 94

Figure 5-1 TEM images of nanocrystal samples GZNO-2, 3, and 4 synthesized at (a) 650 ℃ and (b) 750 ℃ and (c) 850 ℃ respectively. (d) XRD spectra of samples GZNO-2, 3, and 4. (e) Shift in the position of the (101) diffraction peak with respect to wurtzite ZnO and GaN. 104

Figure 5-2 UV-Vis diffuse reflectance of GZNO-2, 3, and 4. 105

Figure 5-3 (a) Zinc *K*-edge XANES of GZNO-2, 3, and 4 and ZnO. (b) Gallium *K*-edge XANES of GZNO-2, 3, and 4, GaN and Ga_2O_3. 107

Figure 5-4 Near-edge region of: (a) zinc *K*-edge of GZNO-2, 3, 4 and ZnO; (b) gallium *K*-edge of GZNO-2, 3, 4, GaN, and Ga_2O_3. 108

Figure 5-5 Linear combination fitting of GZNO-2 at the Ga *K*-edge using GaN and Ga_2O_3 as fitting standards. 109

Figure 5-6 Gallium *K*-edge EXAFS of GZNO-2, 3, 4, and GaN (not phase-shift corrected): (a) k^3-weighted to emphasize second (Ga-Ga) coordination shell; (b) *k*-weighted to emphasize first (Ga-N) coordination shell; (c) Zinc *K*-edge EXAFS *k*-weighted to emphasize first (Zn-O) coordination shell (not phase-shift corrected). 111

Figure 5-7 (a) Zn and (b) Ga $L_{3,2}$-edge XANES of GZNO-2, 3, and 4 (normalized to unit edge jump). 113

Figure 5-8 Zn and Ga L_3-edge XANES of (a) GZNO-2, (b) GZNO-3, and (c) GZNO-4 (E_0 set to 0 eV). 114

Figure 5-9 (a) Nitrogen and (b) oxygen *K*-edge XANES of GZNO-2, 3, and 4. Near-edge region of (a) nitrogen and (d) oxygen *K*-edge of GZNO-2, 3, and 4. All spectra are normalized to unit edge jump. 116

Figure 5-10 (a) XEOL of GZNO-2, 3, and 4 excited with 580 eV X-rays (above O *K*-edge). (b) Expanded view of NBG emission from ZnO phase in GZNO-2. All spectra are normalized to unit intensity. 118

Figure 6-1 Schematic of streak camera TR-XEOL apparatus. 127

Figure 6-2 (a) 5 ns streak image of XEOL emission (340-640 nm) from GZNO excited at 550 eV (see O *K*-edge XANES inset). (b) XEOL decay lifetime windows taken from blue (400 nm) and red (550 nm) regions of the streak image respectively. (c) Fast and slow XEOL spectral windows taken from 0.5-0.6 ns and 1.45-1.55 ns (both raw data and Gaussian fits are displayed). 131

Figure 6-3 XEOL spectra of GZNO, normalized to unity, recorded un-gated and using 0.5-0.6, 1.45-1.55, and 0.5-5.0 ns time windows respectively (Gaussian fit of raw TR data displayed). 132

Figure 6-4 TR-XEOL spectra of GZNO collected with excitation energies above the N and O *K*-edges and Zn and Ga L_3-edges using (a) 0.5-0.6 ns and (b) 1.45-1.55 ns time windows respectively (Gaussian fit of raw data displayed). XEOL lifetime decay spectra of GZNO collected with excitation energies above the N and O *K*-edges and Zn and Ga L_3-edges using (c) 466-475 nm and (d) 507-517 nm wavelength windows respectively. 134

Figure 6-5 XEOL lifetime decay of GZNO collected using an excitation energy of (a) 550 eV (above the O *K*-edge) and (b) 1130 eV (above the Ga L_3-edge) with integration windows centered on the 471 nm (fast) and 512 nm (slow) emission bands. 136

Figure 6-6 XEOL decay lifetimes (a) τ_1 and (b) τ_2 as a function of excitation energy taken below, at resonance, and above the N and O *K*-edges and Zn and Ga L_3-edges using integration windows of 505-515 nm and 465-475 nm. 139

List of Abbreviations

APS:	Advanced Photon Source
BG:	Band Gap
BM:	Bending Magnet
CB:	Conduction Band
CBM	Conduction Band Minimum
CCD:	Charge Coupled Device
CLS:	Canadian Light Source
DAP:	Donor-Acceptor Pair
DC:	Direct Current
DCM:	Double Crystal Monochromator
DFT:	Density Functional Theory
EDS:	Energy Dispersive X-ray Spectroscopy
EDX:	Energy Dispersive X-ray Spectroscopy
EELS:	Electron Energy Loss Spectroscopy
EPR:	Electron Paramagnetic Resonance
ESRF:	European Synchrotron Radiation Facility
EXAFS:	Extended X-ray Absorption Fine Structures
FWHM:	Full Width Half Maximum
FY:	Fluorescence Yield
GaN-ZnO:	Gallium Nitride – Zinc Oxide Solid Solution
GHG:	Green House Gas
GIZNO:	Gallium Indium Zinc Oxynitride Solid Solution
GIZO:	Gallium Indium Zinc Mixed Oxide
GZNO:	Gallium Nitride – Zinc Oxide Solid Solution
GZO:	Gallium Zinc Mixed Oxide
HPHT:	High Pressure High Temperature
IMFP:	Inelastic Mean Free Path
IR:	Infrared
IRF:	Instrument Response Function

LINAC:	Linear Accelerator
MCA:	Multi-Channel Analyzer
MCP:	Multi-Channel Plate
MS:	Multiple Scattering
NBG:	Near Band Gap
NHE:	Normal Hydrogen Electrode
NIR:	Near Infrared
NSLS:	National Synchrotron Light Source
PL:	Photoluminescence
PLE:	Photoluminescence Excitation
PLY:	Photoluminescence Yield
PMT:	Photon Multiplier Tube
PNC:	Pacific Northwest Consortium
RF:	Radio Frequency
RMS:	Root Mean Square
RT:	Room Temperature
SEM:	Scanning Electron Microscopy
SGM:	Spherical Grating Monochromator
SR:	Synchrotron Radiation
TAC:	Time to Amplitude Converter
TEM:	Transmission Electron Microscopy
TEY:	Total Electron Yield
TGA:	Thermogravimetric Analysis
TR-PL:	Time Resolved Photoluminescence
TR-XEOL:	Time Resolved X-ray Excited Optical Luminescence
UV-Vis:	Ultraviolet - Visible
UV-Vis-NIR:	Ultraviolet - Visible - Near-Infrared
XAS:	X-ray Absorption Spectroscopy
XAFS:	X-ray Absorption Fine Structures
XANES:	X-ray Absorption Near Edge Structures
XEOL:	X-ray Excited Optical Luminescence
XES:	X-ray Emission Spectroscopy

XPS:	X-ray Photoelectron Spectroscopy
XRD:	X-ray Diffraction
XSD:	X-ray Science Division
ZGON:	Zinc Gallium Oxynitride

List of Appendices

Appendix A: Copyright Release for Chapter 3 from the American Chemical Society 152

Appendix B: Copyright Release for Chapter 4 from the American Chemical Society 153

Appendix C: Copyright Release for Chapter 6 from the Institute of Physics..... 154

Chapter 1

1 Introduction

This thesis is concerned with the investigation of the structural, electronic, and optical properties of gallium nitride – zinc oxide solid solutions in nanostructured systems. The methodologies include X-ray absorption fine structure (XAFS), especially X-ray absorption near edge structure (XANES), X-ray excited optical luminescence (XEOL), and time-resolved XEOL using synchrotron radiation. The relevance of the system of interest and background information is presented below in section 1.1 and the organization of the thesis is summarized in section 1.2.

1.1 Overall Water Splitting Under Visible Light

Hydrogen has been identified as a potential energy carrier in many low greenhouse gas (GHG) scenarios due to its high energy capacity and environmental friendliness vs. traditional energy sources [1,2]. Currently fossil fuels, such as natural gas, are the primary source of hydrogen production using processes like steam reforming.

$$CH_{4(g)} + H_2O_{(g)} \rightarrow CO_{(g)} + 3H_{2(g)} \tag{1-1}$$

$$CO_{(g)} + H_2O_{(g)} \rightarrow CO_{2(g)} + H_{2(g)} \tag{1-2}$$

The use of hydrocarbons such as fossil fuels or biomass to generate hydrogen requires subsequent capture and sequestration of the CO_2 produced (Equations 1-1 and 1-2), and therefore these are not attractive as sources of hydrogen for clean, environmentally friendly, and low GHG energy production [3-5]. Hydrogen produced from water, however, does not suffer from the same challenge of unwanted point of conversion emissions but does require that energy be supplied from an external source. The water splitting reaction (Equation 1-3) is a typical “uphill reaction” with a large positive change in Gibbs free energy (ΔG^0 = 237 kJ/mol or 1.23 eV) [3].

$$H_2O \rightarrow \tfrac{1}{2}O_2 + H_2;\ \Delta G^0 = 237\ \text{kJ/mol} \tag{1-3}$$

The half-reactions are described below as

$$2H^+ + 2e^- \rightarrow H_2\text{:}\ (E_{red} = 0\ \text{eV}) \tag{1-4}$$

$$H_2O + 2h^+ \rightarrow \tfrac{1}{2}O_2 + 2H^+\text{:}\ (E_{ox} = -1.23\ \text{eV}) \tag{1-5}$$

If the energy required for the production of hydrogen from water can be supplied by an environmentally friendly source, such as the sun, then hydrogen can be considered as a potential green energy alternative. Thus the photocatalytic splitting of pure water into hydrogen and oxygen is a highly coveted process for converting and storing solar energy as chemical energy. The use of semiconductor powders as photocatalysts for the catalytic splitting of water into hydrogen and oxygen is a promising method for converting solar energy into chemical energy for storage and future use due to the simplicity of this method [4,6]. The general processes in semiconductor based photocatalytic water splitting are shown in Figure 1-1.

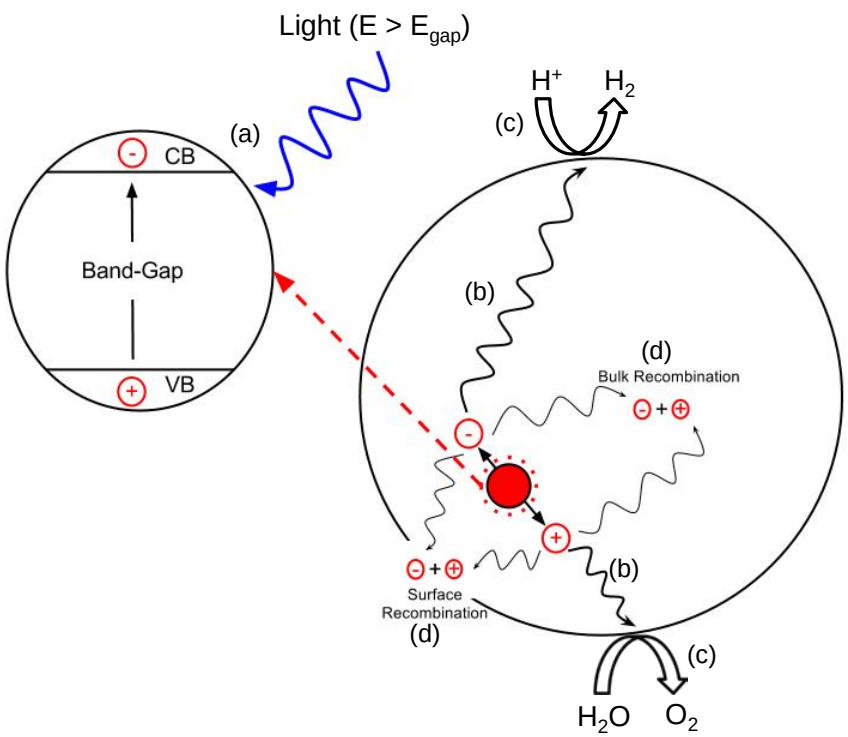

Figure 1-1 General processes in semiconductor photocatalytic water splitting; (a) photon with energy greater than band-gap is absorbed creating hole in VB and electron in CB, (b) electrons and holes separate and migrate to surface, (c) electrons and holes reduce and oxidize water to produce H_2 and O_2, (d) electrons and holes recombine suppressing catalytic activity [7].

When a semiconductor is illuminated using photons with energy greater than or equal to the band-gap energy an electron is excited into the conduction band leaving a hole in the valence band (Figure 1-1(a)). Migration of electrons and holes to the surface of the semiconductor (Figure 1-1(b)) provides photogenerated carriers for use in subsequent surface reduction and oxidation reactions respectively (Figure 1-1(c)). After excitation charge recombination (Figure 1-1(d)), both bulk and surface, and charge separation/migration (Figure 1-1(b)) are the two primary competitive processes that have a large effect on photocatalytic efficiency. Separation of excited electrons and holes may be required to overcome an energy barrier such as the binding energy of the electron–hole pair, or exciton. Charge migration is an activation process which results in the availability of surface charges to participate in the desired surface chemical reactions, in this case the reduction and oxidation of water to produce hydrogen and oxygen respectively. Both surface and bulk charge recombination result in either the emission of optical photons or phonon generation, which reduces the number of available charge carriers and thus acts as a deactivation process. Thus it is critical to have efficient charge separation/migration while avoiding any bulk/surface charge recombination in order to produce an effective photocatalyst for overall water splitting. According to Equation 1-3 the band-gap energy of the semiconductor photocatalyst should be >1.23 eV (or <1100 nm), however, in order to make use of visible light it should be <3.0 eV (or >400 nm). The pioneering work by Fujishima and Honda [8], in which they demonstrated photoelectrochemical water splitting using a rutile TiO_2 photoanode and a platinum cathode with an external bias, and the subsequent work by Bard to design a photocatalytic system using semiconductor powders or particles as photocatalysts [9-11], has led to intense research in this field over the past decades [4,5]. Although many semiconductors have been reported to be active for the water splitting reaction, none have been capable of demonstrating stable and reproducible overall water splitting capabilities under irradiation with visible light. In order for a semiconductor to be a suitable candidate for overall water splitting using visible light it must meet the following three requirements: (1) to facilitate the reduction (Equation 1-4) and oxidation (Equation 1-5) of water the band-edge potentials must be positioned such that the bottom level of the conduction band is more negative than the reduction potential of H^+/H_2 (0 eV vs. normal hydrogen electrode (NHE)) and the top of

the valence band is more positive than the oxidation potential of O_2/H_2O (1.23 eV vs. NHE), (2) the semiconductor must be stable in the photocatalytic region, and (3) the band-gap energy must be lower than 3 eV (>400 nm). Therefore in order to produce a suitable semiconductor photocatalyst for overall water splitting using visible light band-gap energy, stability to photo-corrosion, and position of the band-edge potentials must all be taken into account.

Generally, most efficient photocatalytic materials are often metal oxide, nitride, and sulfides which contain cations with either a d^0 electron configuration (i.e. Ti^{4+}, Zr^{4+}, Nb^{5+}, Ta^{5+}, W^{6+}, and Mo^{6+}) or a d^{10} electron configuration (i.e. In^{3+}, Ga^{3+}, Ge^{4+}, Sn^{4+}, and Sb^{5+}) [5]. The bottom of the conduction band of d^0 and d^{10} metal cations are formed by empty d and hybridized s and p orbitals respectively. Thus d^{10}-semiconductors have an advantage over d^0-semiconductors for use as photocatalysts due to the larger dispersion of the hybridized s–p orbitals (vs. empty d-orbitals in d^0-semiconductors) in the conduction band which increases the mobility of photogenerated electrons promoting photocatalytic activity [12,13]. The top of the valence band of metal oxides, nitrides, and sulfides is composed of O 2p, N 2p, and S 3p orbitals respectively. Although some sulfides, such as CdS, have suitably positioned band-edge potentials and band-gap energies that are in the visible region, their susceptibility to photo-corrosion renders them inactive as photocatalysts for water splitting. Since N 2p orbitals have a higher potential energy (with respect to the Fermi level) than O 2p orbitals the use of metal nitrides, or metal oxynitrides, as visible light photocatalysts seems to be an attractive option as they should exhibit narrower band-gaps than the analogous metal oxides. Although Ta_3N_5 [14,15], TaON [16-18], and $LaTiO_2N$ [19,20], have all been investigated as potential photocatalysts for visible light driven water splitting none have been successfully implemented due in part to relatively high defect densities in the bulk and at the surfaces of these materials.

As mentioned in the preceding discussion d^{10}-semiconductors have an advantage as photocatalysts over d^0-semiconductors due to the large dispersion of hybridized s–p orbitals in the conduction band of these materials. It follows that oxynitrides with a d^{10} electron configuration are potential candidates as photocatalysts for water splitting. The

d^{10} oxynitride β-Ge_3N_4 has been previously demonstrated as an active photocatalyst for overall water splitting, but, the band-gap of β-Ge_3N_4 is 3.8 eV which makes it responsive only to UV light [21-24]. Thus it follows that an oxynitride d^{10}-semiconductor that is active under irradiation with visible light could be an ideal candidate as a photocatalyst for overall water splitting.

1.2 Gallium Nitride – Zinc Oxide Solid Solutions for Overall Water Splitting Under Visible Light

Since the first report of a gallium nitride – zinc oxide $(Ga_{1-x}Zn_x)(N_{1-x}O_x)$ solid solution by Maeda et al. in 2005 [25] as d^{10}-oxynitride photocatalysts for visible-light driven overall water splitting there has been an intense research focus into the study of these novel materials [26- 54]. Solid solutions are commonly formed using mixtures of wide and narrow band-gap semiconductors, where both the band-gap energy and the position of band-edge potentials can be controlled by varying the ratio of wide / narrow BG semiconductor (Figure 1-2).

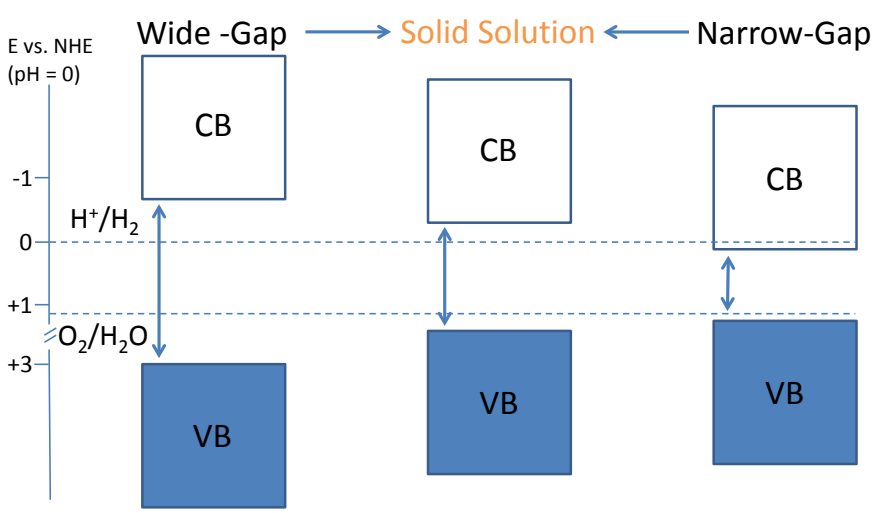

Figure 1-2 Intermediate band-gap formed when wide-gap and narrow-gap semiconductors alloy to form a solid solution.

Solid solutions of $Cd_xZn_{1-x}S$, $(AgIn)_xZn_{2(1-x)}S_2$, $Sr_2(Ta_{1-x}Nb_x)_2O_2$, $BiTa_{1-x}Nb_xO_4$, and $Bi_xIn_{1-x}TaO_4$ have all been prepared in this manner but none of them have demonstrated overall water splitting capabilities: (1) with photocatalytic activity in the visible region of the solar spectrum, and (2) without the need for an additional electrolyte or electron donor [5]. Although both GaN and ZnO are wide band-gap semiconductors with band-gap energies, E_{gap}, of 3.4 eV [55] and ≈ 3.3 eV [56] respectively, the similarity of their lattice parameters ($a = b = 3.19$ Å, $c = 5.19$ Å for GaN and $a = b = 3.25$ Å, $c = 5.21$ Å for ZnO), and their wurtzite structure make them ideal for solid solution formation. We would expect that the band-gap energy of the resultant $(Ga_{1-x}Zn_x)(N_{1-x}O_x)$ (GaN-ZnO) solid solution would lie somewhere between that of the two parent materials, but, Maeda et al. found that the band-gap of these $(Ga_{1-x}Zn_x)(N_{1-x}O_x)$ solid solutions narrows below that of both GaN and ZnO, with $E_{gap} < 3$ eV, exhibiting absorption edges in the visible and a red-shift in the absorption edge with increasing ZnO (or x) content [25]. It was hypothesized that the band-gap narrowing observed in GaN-ZnO solid solutions may be due to p–d repulsion in the valence band between N 2p and Zn 3d orbitals when Zn^{2+} is incorporated into the GaN lattice causing the top of the valence band (formed by N 2p orbitals) to rise to higher potential energy and subsequently narrowing the band-gap of the GaN host (Figure 1-3).

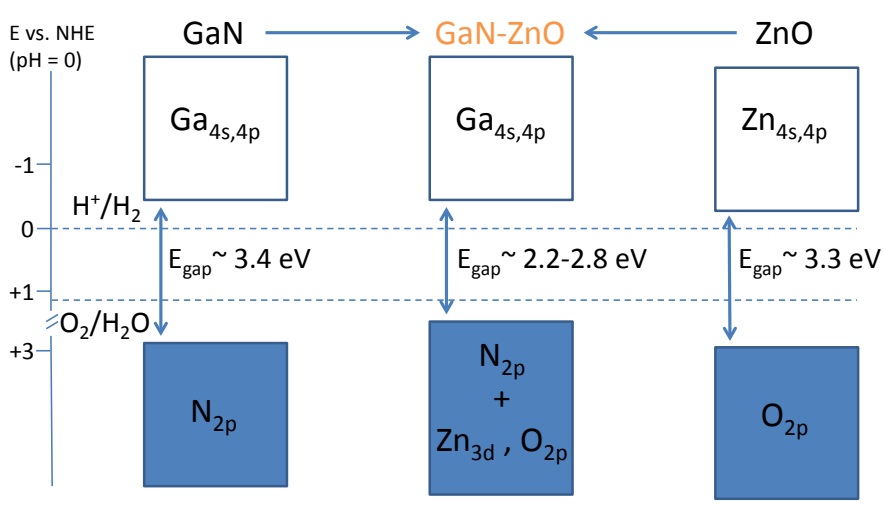

Figure 1-3 Band-gap narrowing and band-edge position in GaN-ZnO solid solutions.

This has been reported previously for II-VI semiconductors containing Zn^{2+} ions as a principal component and has been assigned to p–d repulsion in the valence band (e.g., O 2p–Zn 3d repulsion in $ZnAl_2O_4$) which results in an upward shift of the valence band-maximum (VBM) without changing the position of the conduction band-minimum (CBM) [57].

Maeda and co-workers studied the relationships between the physical properties of $(Ga_{1-x}Zn_x)(N_{1-x}O_x)$ solid solutions and their photocatalytic activity by varying the nitridation time of the β-Ga_2O_3 and ZnO and the ratio of ZnO / β-Ga_2O_3 in the nitridation precursor mixture [26]. Using X-ray diffraction (XRD) they discovered that the positions of the (100) and (101) diffraction peaks were successively shifted to higher angles (2θ) with an increase in nitridation time indicating the formation of a solid solution of GaN and ZnO. The *a* and *c* lattice constants were observed to increase almost linearly as a function of zinc concentration (x) in the resultant solid solutions, with the slight deviation in the linearity of the *c*-axis lattice constant attributed to the smaller difference in *c*-axis lengths between GaN and ZnO. From X-ray photoelectron spectroscopy (XPS) of Ga $2p_{3/2}$, Zn $2p_{3/2}$, O 1s, and N 1s in GaN-ZnO solid solutions prepared using different nitridation times they found that oxygen species exist around both Zn and Ga atoms on the surface, lattice O atoms at the surface possess less negative charge than those in ZnO, and nitrogen species on the surface have an electronic state similar to that of GaN. Using a combination of XPS and energy dispersive X-ray spectroscopy (EDS) they were able to determine the ratios of Zn/Ga in the surface and bulk respectively. It was found that both the surface and bulk ratio of Zn/Ga decreased with increasing nitridation time and that Zn(s) volatilization occurs more readily on the GaN-ZnO surface. The surface O/Ga ratio was observed to gradually increase with increasing nitridation time while the bulk oxygen concentration decreased suggesting that removal of surface oxygen is difficult under these reaction conditions. From UV-Vis diffuse reflectance spectroscopy it was determined that the absorption edges, which are located at longer wavelengths than those of either GaN or ZnO, shift to shorter wavelength with increasing nitridation time indicating a resultant increase in the band-gap energy of the resultant GaN-ZnO solid solution. This increase in band-gap energy coincides with the decrease in Zn content (x) as Zn(s) is volatilized from the solid solution. Preliminary density functional theory

(DFT) work showed that the bottom of the conduction band for GaN-ZnO is composed primarily of Ga 4s and 4p orbitals while the top of the valence band is made up of N 2p orbitals followed by Zn 3d and O 2p orbitals. Thus it is possible that the increase in band-gap energy associated with an increase in nitridation time is a result in a reduction in the dispersion of Zn 3d states in the valence band and a subsequent reduction in p–d repulsion, and thus a reduction in BG narrowing, as Zn(s) is removed from the GaN-ZnO solid solution.

The effects of nitridation time on photocatalytic activity were also studied and it was determined that the largest increase in activity was obtained over the range of 5 to 15 h with a maximum activity of 58 $\mu mol \cdot h^{-1}$ (H_2) and 29 $\mu mol \cdot h^{-1}$ (O_2) for a GaN-ZnO solid solution (loaded with RuO_2 nanoparticle co-catalysts for H_2 evolution) synthesized using a nitridation time of 15 h. The increase in activity over this range of nitridation times was attributed to an increase in crystallinty which would reduce the number of defects acting as recombination centers for electrons and holes. This increase in crystallinity was observed as a strengthening and narrowing of the (101) diffraction peak. Nitridation for longer than 15 h had a negative effect on photocatalytic activity which was attributed to the loss of surface zinc through the reduction of ZnO to Zn metal, which in turn results in vacancies at zinc sites on the surface of the catalyst that can subsequently act as recombination centers for photogenerated electrons and holes. Since it is well known that ZnO is reduced to Zn metal upon exposure to a reducing atmosphere the effects of the ZnO ratio in the starting material were also studied. It was determined that a ratio of Zn/Ga = 1 in the staring materials produced a GaN-ZnO solid solution with the highest activity (and lowest BG energy). The Zn/Ga ratio in the product was also observed to decrease gradually as the Zn/Ga ratio in the staring materials was increased. The increase in activity from Zn/Ga = 0.25 to 1 appeared to be due to a concomitant increase in crystalinity of the resultant solid solution. Above a Zn/Ga ratio of 1, however, the photocatalytic activity was found to decrease which was attributed to a decrease in zinc concentration and is consistent with previous findings that the activity of GaN-ZnO for overall water splitting is strongly dependent on the Zn concentration. The highest activity for overall water splitting was obtained for a GaN-ZnO sample with $x = 0.12$ with a nitridation time of 15 h. The structural and electronic analysis of GaN-ZnO solid

solutions for overall water splitting revealed that the photocatalytic activity was heavily dependent on crysallinity and zinc concentration, both in the starting material and the final product.

Yashima et al. studied the crystal structure and optical properties of a $(Ga_{1-x}Zn_x)(N_{1-x}O_x)$ oxynitride photocatalyst with $x = 0.13$ using neutron diffraction, and photoluminescence (PL) and UV-Vis diffuse reflectance spectroscopy respectively [27]. They determined that the refined unit cell parameters of the solid solution were $a = b =$ 3.18986(7) and $c = 5.18367(8)$ Å, and the refined positional parameter z for the (Ga,Zn) cation (0.3775(3)) was in good agreement with that of GaN (0.3771(1)). The (Ga,Zn) cation was found to coordinate with four (N,O) anions to form $(Ga,Zn)(N,O)_4$ tetrahedrons as expected for a wurtzite structure. The range of interatomic distances between the cation and the anions was determined to be 1.9478(4)–1.95710(13) Å, with an estimated quadratic elongation of 1.000 and an angle variance of 0.24 deg^2 indicating that the $(Ga,Zn)(N,O)_4$ tetrahedron is regular. The refined occupancies of nitrogen and oxygen atoms were determined to be 0.84(2) and 0.16(2) respectively resulting in a chemical formula of $Ga_{0.87}Zn_{0.13}N_{0.84(2)}O_{0.16(2)}$ which is in good agreement with that determined by chemical analysis ($Ga_{0.87}Zn_{0.13}N_{0.83}O_{0.16}$) and indicates that oxygen substitutes for nitrogen in the material. Although the substitution of oxygen for nitrogen in the formation of GaN-ZnO solid solutions has been previously suggested by the variation of the XRD profile and diffuse reflectance spectra as a function of x this was the first direct experimental evidence of this substitution. Diffuse reflectance spectroscopy estimated the band-gap of the GaN-ZnO solid solution to be ~2.5 eV (~500 nm), i.e. in the visible, and PL spectroscopy revealed a broad optical emission band at ~1.9 eV (650 nm).

Hirai et al. studied the origin of visible light absorption in $(Ga_{1-x}Zn_x)(N_{1-x}O_x)$ solid solutions [36]. UV-Vis diffuse reflectance spectra of GaN-ZnO solid solutions with $x =$ 0.05, 0.10, and 0.20 showed absorption edges that appear in the visible region at wavelengths longer than the intrinsic absorption edges of GaN and ZnO. It was determined that with decreasing wavelength the absorption strength gradually increased from ~500 nm to a maximum close to 370 nm and the absorption edge is shifted to

slightly longer wavelengths with increasing ZnO (*x*) composition. Since the absorption coefficient should increase abruptly at the intrinsic absorption edge in a direct band-gap semiconductor the gradual increase in absorption strength (coefficient) for GaN-ZnO solid solutions was interpreted to imply that the absorption edges observed in the visible region do not represent the intrinsic absorption edges in these materials.

Very broad low temperature (10 K) photoluminescence (PL) bands were observed for all samples with the peak wavelength red shifted (from ~500 to 650 nm) with increasing *x* composition. The PL bands appeared to be composed of several narrower bands which suggested that the red-shift observed in the peak wavelength with an increase in *x* may be due to the enhancement of narrower bands on the longer wavelength side of the PL emission spectra. These narrower bands were assigned to Zn-related acceptor levels above the conduction band maximum in the solid solution. With an increase in *x* there should be a corresponding increase in the dispersion of Zn acceptor states above the conduction band resulting in a red-shift in the peak wavelength of the PL emission bands. It was also suggested that oxygen substituting for nitrogen was likely to act as a donor impurity creating an electron donor level below the valence band minimum. Thus the broad PL bands observed for these GaN-ZnO solid solutions have been assigned to donor-acceptor pair (DAP) recombination between electrons on O donor levels and holes on Zn-related acceptor levels. Photoluminescence excitation (PLE) spectra in the 300 to 450 nm range were detected at 500 nm ($x = 0.05$), 600 nm ($x = 0.10$), and 650 nm ($x = 0.20$) at 10 K corresponding to the observed wavelengths of maximum emission in the PL spectra. The intensity of the PLE was found to increase strongly with decreasing wavelength at ~380 nm up to a plateau at ~360 nm for the three different *x* compositions. The strong increase in the PLE spectra observed near 370 nm was assigned to the intrinsic absorption edge in GaN-ZnO, which was not observed to shift with composition (*x*). The PL and PLE spectra observed for these GaN-ZnO materials suggested that visible light absorption arises from the excitation of electrons filling Zn-related acceptor levels into the conduction band or unfilled donor levels just below the conduction band minimum.

This explanation for the observed PL and PLE spectra is, however, in contradiction with previous DFT calculations which suggest that visible light absorption is in these materials is due to p–d repulsion between N 2p orbitals at the top of the valence band with Zn 3d orbitals in the valence band resulting in an upward shift of the valence band maximum with no corresponding change in the position of the conduction band minimum and thus a subsequent narrowing of the band-gap energy. Although this model should still be valid for solid solutions with stoichiometric unit cells it is likely that the observed experimental results were due to local inhomogeneity of Zn and O densities in these dilute ($x \leq 0.20$) GaN-ZnO materials. These results are consistent with the previous work of Maeda and co-workers who suggested that the photocatalytic activity in these materials is strongly dependent on Zn concentration (or x) [26].

The effect of post-calcination on the photocatalytic activity of $(Ga_{1-x}Zn_x)(N_{1-x}O_x)$ solid solutions was studied by Maeda et al. [38]. Post-calcination in air at temperatures of 573, 773, 873, 973, 1073, and 1173 K was performed on a GaN-ZnO solid solution with $x = 0.12$. All samples calcined at temperatures below 973 K were found to exhibit single-phase diffraction patterns indicative of a hexagonal wurtzite structure similar to that of GaN and ZnO. Above 973 K an additional phase, assigned to spinel $ZnGa_2O_4$, was observed in XRD pattern of the solid solution. At 1173 K diffraction peaks assigned to the wurtzite GaN-ZnO phase disappeared and new peaks assignable to β-Ga_2O_3 and GaN were observed to appear with the concomitant increase in the intensity of $ZnGa_2O_4$ peaks. These observations suggested that the crystal structure of GaN-ZnO is retained under calcination in air up to temperatures of 973 K, and then decomposition of the crystal structure begins at calcination temperatures above 1073 K. These results were consistent with thermogravimetric analysis (TGA) findings which demonstrated a marked increase in sample mass at temperatures above 1023 K due to the replacement of nitrogen with oxygen in the solid solution. Post-calcination at temperatures below 973 K was observe to result in no change in intensity and peak position of the diffraction peaks, in Zn/Ga atomic ratios (from EDX), and no marked change in particle size/morphology (from SEM). Additional study of the post-calcination samples by XPS revealed no change in surface atomic composition up to 873 K indicating that no surface oxidation takes place at these temperatures.

A gallium *K*-edge X-ray absorption near edge structures (XANES) study of the post-calcined samples showed that the Ga *K*-edge was identical to that of GaN for both the as-prepared sample and samples calcined at temperatures below 873 K indicating that the local structure and valence state of gallium atoms in the GaN-ZnO solid solution is close to that in GaN. For sample calcined at or above 973 K the spectral shape of the Ga *K*-edge was observed to change exhibiting absorption peaks at 10368 eV and 10384 eV in samples calcined at 1173 K. This change in spectral shape was observed to coincide with a small shift of the absorption edge threshold to higher X-ray photon energies, and the sample calcined at 1173 K exhibited a Ga *K*-edge spectrum with spectral features similar to that of $ZnGa_2O_4$ and β-Ga_2O_3. A similar effect was observed in the zinc *K*-edge XANES of the post-calcination samples. The Zn *K*-edge spectrum for the as prepared sample and samples post-calcined at temperatures below 973 K were similar to that of ZnO indicating a local structure and valence for Zn that is primarily ZnO-like. There was, however, a small shift in the position of the absorption edge threshold to lower photon energy vs. ZnO was observed in both the as-prepared and samples calcined below 973 K which was attributed to the difference in bonding polarity between Zn-N and Zn-O (i.e. Zn-N bonding is more covalent than Zn-O bonding), and suggested the presence of Zn-N bonding in this material. There were slight differences observed in the Zn *K*-edge spectrum of the sample calcined at 1073 K vs. both the as-prepared sample and samples calcined below 973 K. The Zn *K*-edge spectrum of the sample calcined at 1173 K was found to be identical to that of the $ZnGa_2O_4$ reference and markedly different from samples calcined at temperatures below 1073 K. The results of the XANES study were consistent with the change observed in the XRD patterns of the post-calcination samples and indicated that the structural characteristics remain almost unchanged for samples calcined at temperatures of 873 K or below. When the calcination temperature was 973 K or higher there were structural changes observed in the material and at sufficiently high calcination temperature (i.e. $\geq$ 1173 K) complete oxidative decomposition of the GaN-ZnO solid solution was observed.

The UV-Vis diffuse reflectance spectra were measured for all samples and the as-prepared standard. Samples calcined at temperatures $\leq$ 973 K were observed to have absorption edges in the visible (~470 nm) and exhibited a slight red-shift in the onset of

the absorption edge with increasing calcination temperature up to a maximum at 973 K. Above 973 K there a blue shift was observed in the onset of the absorbion edge reaching a minmum (~400 nm) for the sample calcined at 1173 K. There was no explanation given for the observation of a red-shift upon increasing calcination temperature up to 973 K, however, the significant blue-shift in the absorption edge after post-calcination at 1173 K was attributed to the collapse of the GaN-ZnO structure. PL of the as-prepared sample and samples post-calcined at temperatures up to 873 K exhibited a broad emission band at ~650 nm with the peak position shifting to slightly longer wavelengths and the intensity of the emission band decreasing as a function of increasing calcination temperature. The decrease observed in PL intensity with increasing calcination temperature indicated that post-calcination of GaN-ZnO reduces the density of photogenerated carrier traps in the material suggesting potential for improved photocatalytic activity. The photocatalytic activity of the samples calcined at temperatures below 973 K was observed to increase with an increase in post-calcination temperature up to a maximum at 873 K followed by a significant decrease at temperatures ≥ 973 K. It was concluded that post-calcination improves photocatalytic activity in GaN-ZnO by eliminating zinc- and/or oxygen-related defects, which act as photogenerated electron and hole carrier traps. Post-calcination at excessively high temperatures, however, was determined to result in destruction of the $(Ga_{1-x}Zn_x)(N_{1-x}O_x)$ structure and subsequently decrease photocatalytic activity.

Kamata and co-workers attempted to prepare a solid solution of $(Ga_{1-x}Zn_x)(N_{1-x}O_x)$ and InN in order to extend the absorption edge further into the visible region [40]. The as obtained Ga-In-Zn-O-N powder was brown and showed a decrease in the atomic ratio of Zn/Ga and In/Ga vs. the starting precursor which was attributed to the volatilization of zinc and indium species under the reductive ammonolysis conditions. The nitrogen content was observed to be lower than that expected from the formation of an ideal solid solution of GaN, InN, and ZnO, which was indicative of incomplete nitridation at the synthesis temperature of 873 K, and suggested the formation of a mixed oxynitride as opposed to a solid solution. This was found to be in agreement with XRD results which showed that the Ga-In-Zn-O-N powder had a wurtzite-like structure, however, the very broad diffraction peaks suggested a low degree of crystallinity. The

local structure and valence state of gallium, zinc, and indium were studied via Ga, Zn, and In *K*-edge XANES. The Ga and Zn *K*-edge XANES spectra were observed to be very different from those of GaN and ZnO respectively demonstrating that the local structure and valence state of gallium and zinc in the resultant mixed oxynitride is not the same as that in either GaN and ZnO or a $(Ga_{1-x}Zn_x)(N_{1-x}O_x)$ solid solution. The In *K*-edge XANES of the mixed oxynitride was significantly different from that of InN. It is this author's opinion that the near-edge region of the In *K*-edge is, however, consistent with that of the In_2O_3 reference standard and thus suggests segregation of an In_2O_3 phase. The absorption edge of the Ga-In-Zn mixed oxynitride was found to be ~600 nm by UV-Vis diffuse reflectance spectroscopy, which is at longer wavelength than a GaN-ZnO sample with the same Zn/Ga ratio (0.72). It was suggested that the red-shift observed in the absorption edge is due to the presence of both In and N species in the mixed oxynitrde. The Ga-In-Zn-O-N product modified with a nanoparticulate rhodium co-catalyst was found to be active as a photocatalyst for visible-light driven hydrogen and oxygen evolution from water containing sacrificial reagents.

The formation of wurtzite $(Ga_{1-x}Zn_x)(N_{1-x}O_x)$ solid solutions during the solid-state reaction of ammonia with Ga_2O_3/ZnO mixtures was studied by Chen et al. using in situ time-resolved XRD and ex situ X-ray absorption fine structures (XAFS) [41]. It was determined from in situ XRD that GaN-ZnO solid solutions form through an intermediate spinel $ZnGa_2O_4$ phase. In spinel $ZnGa_2O_4$ Zn atoms are in tetrahedral sites and Ga atoms are in octahedral sites, whereas in wurtzite ZnO and GaN both Zn and Ga atoms occupy tetrahedral sites in the crystal lattice. Thus in a spinel to wurtzite phase transition the Zn atoms do not need to undergo a large geometric rearrangement, however, the Ga atoms at octahedral sites must be transformed into tetrahedral sites. In order to form a wurtzite GaN-ZnO solid solution from the spinel $ZnGa_2O_4$ intermediate at least two of the Ga-O bonds must be broken and the oxygen atoms removed and replaced with nitrogen atoms. The conversion of spinel $ZnGa_2O_4$ to wurtzite $(Ga_{1-x}Zn_x)(N_{1-x}O_x)$ was monitored via in situ XRD using isothermal heating under ammonia at 850 ℃ and a linear decrease of the spinel phase and increase of the wurtzite phase was observed with an increase in nitridation time indicative of a zeroth-order reaction of a surface or interface nature. The activation energy for the spinel to wurtzite phase transformation was determined to be 3.7

± 0.3 eV which is close in energy to the bond enthalphy of Ga-O (3.66 eV). Thus it was suggested that Ga-O bond breaking in spinel $ZnGa_2O_4$ may be the rate-limiting step in the formation of GaN-ZnO from the reaction of $ZnGa_2O_4$ with ammonia.

The nitridation of a mixture of β-Ga_2O_3 with ZnO to produce a $(Ga_{1-x}Zn_x)(N_{1-x}O_x)$ solid solution was studied using in situ XRD under non-isothermal conditions from ~500 to 850 ℃. At low temperatures characteristic diffraction peaks for wurtzite ZnO and β-Ga_2O_3 were observed. As the nitridation temperature increased the peak intensity of ZnO was observed to decrease while the 2θ angle was observed to shift to lower values indicating a thermal expansion of the ZnO phase. When the reaction was held at an isothermal annealing temperature of 850 ℃ as the intensity of diffraction peaks associated with ZnO decreased the intensity of peaks assigned to spinel $ZnGa_2O_4$ increased and no zinc nitride phase was detected. The ZnO phase was observed to be completely consumed when the intensity of the spinel peaks reached a maximum. Diffraction peaks associated with the formation of a wurtizite GaN-ZnO solid solution were observed after the formation of the intermediate $ZnGa_2O_4$ phase. After the spinel phase was consumed the growth of the solid solution was observed to slow down, the peak position shifted to higher 2θ, and the peak widths became narrower with increasing nitridation time. Since no diffraction peaks were observed for wurtzite GaN it was determined that due to its slow kinetics GaN formation likely cannot compete with the formation of the GaN-ZnO solid solution. The transformation of β-Ga_2O_3 and ZnO to wurtzite $(Ga_{1-x}Zn_x)(N_{1-x}O_x)$ under nitridation with ammonia was described as follows:

$$Ga_2O_3 + ZnO \rightarrow ZnGa_2O_4 \tag{1-6}$$

$$\tfrac{1}{2}(1-x)ZnGa_2O_4 + \tfrac{2}{3}(2-3x)NH_3 \rightarrow (Ga_{1-x}Zn_x)(N_{1-x}O_x) + (2-3x)H_2O + \tfrac{1}{2}(1-3x)Zn + \tfrac{1}{6}(1-3x)N_2 \tag{1-7}$$

From Equation 1-7 it is clear that the maximum bulk Zn/(Zn + Ga) ratio in the wurtzite $(Ga_{1-x}Zn_x)(N_{1-x}O_x)$ product synthesized by the nitridation of β-Ga_2O_3 and ZnO will be 1/3 regardless of the Zn/Ga ratio in the starting material since the ratio of Zn/Ga in spinel $ZnGa_2O_4$ is 0.5. It was determined that when the starting ratio of Zn/Ga is less than 0.5 excess β-Ga_2O_3 reacts with NH_3 and is converted to GaN and when the starting ratio of

Zn/Ga is greater than 0.5 the excess ZnO is reduced to Zn by hydrogen from the pyrolysis of NH_3 and sublimes. The presence of excess ZnO was, however, determined to affect the reaction kinetics resulting in a more rapid formation of the spinel phase and subsequent conversion to the wurtzite phase.

From Ga *K*-edge XANES the local structure and valence of gallium in GaN-ZnO was found to closely resemble that of GaN. The Zn *K*-edge XANES spectra were also observed to be similar to that of ZnO but the position of the absorption edge threshold was found to shift to slightly lower X-ray photon energy in the solid solution which was attributed to a lower oxidation state for Zn in the GaN-ZnO solid solution. A distortion of the second coordination shell (Ga–Ga absorbers) was observed in the gallium *K*-edge extended X-ray absorption fine structures (EXAFS) for a GaN-ZnO sample with $x = 0.22$ (nitridated for 2 h at 850 ℃) vs. the GaN reference standard, however there was no change in peak position of both first and second coordination shells (Ga–O and Ga–Ga absorbers respectively). Shifts in peak position and a reduction in back-transformed FT amplitude were observed in the first and second coordination shells (Zn–O, Zn–Zn, absorbers respectively) vs. the ZnO reference standard. From the Zn *K*-edge EXAFS the Zn–O interatomic distance was observed to expand slightly and the Zn–Zn interatomic distance was observed to contract slightly in the GaN-ZnO solid solution vs. ZnO. This distortion in the local structure of ZnO observed in the EXAFS was interpreted as an effect of the low zinc content in the solid solution ($Zn \leq 0.22$) and thus the subsequent substitution of N for O and Ga for Zn in the crystal lattice. An increase in the Debye-Waller factor (σ^2 Å^2) was observed as a function of decreasing zinc content and was interpreted as an increase in chemical disorder of ZnO in the solid solution when Zn is dilute. Nitrogen and oxygen *K*-edge XANES were measured for a mixed sample containing primarily spinel $ZnGa_2O_4$ with some wurtzite $(Ga_{1-x}Zn_x)(N_{1-x}O_x)$ and a sample containing a pure wurtzite phase of $(Ga_{1-x}Zn_x)(N_{1-x}O_x)$. It was determined that the N *K*-edge for both samples was consistent with the GaN reference, however, a slight broadening of all absorption features was observed in the mixed phase sample. This was attributed to the wurzite $(Ga_{1-x}Zn_x)(N_{1-x}O_x)$ phase being on top of the spinel $ZnGa_2O_4$ phase and implies that the phase transformation starts at the surface of the material. The oxygen *K*-edge XANES for both the mixed phase sample and the pure wurtzite phase

sample were found to differ greatly from that of the ZnO reference standard. In the mixed phase sample there was a strong reduction observed in the intense ZnO multiple-scattering peak and a new pre-edge feature observed that could not be attributed to either ZnO or β-Ga_2O_3. In the pure wurtzite phase sample the intense ZnO multiple-scattering peak was observed to be reduced further in intensity and the pre-edge feature became more intense. The pre-edge feature was attributed to O atoms substituting for N atoms in the $(Ga_{1-x}Zn_x)(N_{1-x}O_x)$ lattice and subsequently acting as holes since O^{2-} is deficient by one electron from N^{3-}. It was also determined that once $(Ga_{1-x}Zn_x)(N_{1-x}O_x)$ forms it is critical to minimize its exposure to NH_3 if the Zn and O content (x) is to be retained. Additionally in order to produce highly crystalline $(Ga_{1-x}Zn_x)(N_{1-x}O_x)$ solid solutions with an atomic zinc content higher than 1/3 other synthesis methods should be explored.

Mapa et al. studied ZnO-rich $(Zn_{1-z}Ga_z)(O_{1-x}N_x)$ (z and $x \leq 0.15$) solid solutions synthesized using a simple combustion method reacting zinc and gallium nitrate precursors with urea [43]. The ratio of Zn/Ga in the resultant solid solutions was found to vary between 49 and 6 resulting in non-stoichiometric compositions varying between $(Zn_{0.98}Ga_{0.02})(O_{0.91}N_{0.09})$ and $(Zn_{0.85}Ga_{0.15})(O_{0.93}N_{0.08})$. All solid solutions products were found to exhibit wurtzite structures with a space group of $P6_3mc$ from Rietveld refinement of the XRD patterns. Both the a and c lattice parameters were observed to systematically decrease from a = 3.2504 Å (c = 5.2052 Å) to 3.2239 Å (5.1924 Å) with an increase in gallium concentration from 2 to 15 % respectively which was attributed to substitution of Ga^{3+} for Zn^{2+} in the crystal lattice since the ionic radius of Ga^{3+} (0.62 Å) is smaller than that of Zn^{2+} (0.74 Å). The incorporation of N^{3-} was found to offset lattice distortion due to Ga^{3+} incorporation in the ZnO lattice, and thus minimize lattice strain. A study of the effect of post-calcination in ambient air on the material demonstrated that there was a weight gain using calcination temperatures greater than 600 ℃ which was attributed to the formation of Ga_2O_3.

From UV-Vis diffuse reflectance measurements the onset of the absorption edge was found to be at longer wavelength than either ZnO or GaN and vary from 410 to 450 nm with the red-shift coinciding with an increase in Ga content from 2–12%. This result is highly significant because a red-shift in the onset of the absorption edge has previously

been observed in GaN-rich $(Ga_{1-x}Zn_x)(N_{1-x}O_x)$ solid solutions and has been attributed to an increase in zinc concentration (x) and a subsequent increase in the dispersion of Zn-related acceptor levels in the resultant material [26,36]. This suggests that visible light absorption in these materials may be due to an increase in the dispersion of Ga-related acceptor levels in the $(Zn_{1-z}Ga_z)(O_{1-x}N_x)$ solid solution. The band-gap of the sample with 12% Ga concentration was estimated to be 2.5 eV from the diffuse reflectance spectrum which is much narrower than that of wurtzite ZnO (3.37 eV). The band-gap narrowing observed in these solid solutions was attributed to the hybridization of N and O 2p states in the valence band and 4s and 4p states of Ga and Zn in the conduction band which could result in an upward shift of the valence band maximum and a corresponding downward shift in the conduction band minimum. Physically mixing ZnO and GaN did not produce a material that showed any absorption in the visible region and gave additional support for the solid solution nature of $(Zn_{1-z}Ga_z)(O_{1-x}N_x)$.

Electron paramagnetic resonance (EPR) studies of the resultant $(Zn_{1-z}Ga_z)(O_{1-x}N_x)$ solid solutions showed the presence of interstitial zinc and oxygen vacancies and it was suggested that these vacancies compensate for the excess anionic charge from the significantly large nitrogen content (in relation to the Ga content) and maintain charge neutrality. From N 1s and Ga $2p_{3/2}$ XPS it was determined that nitrogen exists as N^{3-} and gallium exists as Ga^{3+} as in GaN. XPS measurements of Zn $2p_{3/2}$ core levels of $(Zn_{1-z}Ga_z)(O_{1-x}N_x)$ showed a decrease in binding energy vs. ZnO indicative of a higher electron density on Zn. XPS of the O 1s core level in $(Zn_{1-z}Ga_z)(O_{1-x}N_x)$ showed a narrow O 1s peak at a binding energy consistent with that of ZnO. Peaks assigned to both ZnO and GaN were observed in the Raman spectra of $(Zn_{1-z}Ga_z)(O_{1-x}N_x)$ solid solutions. A broad feature in the Raman spectra at ~575 cm^{-1} was observed for Ga compositions of $z \leq 5\%$ in $(Zn_{1-z}Ga_z)(O_{1-x}N_x)$ and was attributed to heterogeneous near-neighbor environments, however, this feature became sharper and narrower at higher z values ($z > 5\%$) suggesting the formation of a more homogeneous solid solution. Although the catalytic activity of these materials for overall water splitting was not tested they were found to be active photocatalysts for nitrogen fixation.

A new high pressure – high temperature (HPHT) synthetic route for producing zinc-rich $(Ga_{1-x}Zn_x)(N_{1-x}O_x)$ solid solutions using GaN and ZnO as precursors was investigated by Chen et al. using in situ XRD and ex situ XRD and XAFS [44]. Under ambient conditions distinct (100) and (101) diffraction peaks were observed for a 1:1 mixture of ZnO and GaN respectively. When the pressure was increased from ambient to 7.0 GPa the XRD peaks were observed to broaden and the peak positions shifted to lower *d*-spacings. At 600 ℃ under constant press loading at ~3 GPa two distinct wurtizite phases were observed in the XRD pattern, however, at 800 ℃ the peak intensity of ZnO diffraction peaks was significantly decreased which was interpreted as signaling the onset of ZnO lattice disruption or the the diffusion of Zn and O into the GaN lattice. A single wurtzite phase was observed at 1000 ℃ and remained stable upon temperature increase which indicated the formation of a GaN-ZnO solid solution. The high pressure wurtzite phase was found to be quenchable to ambient conditions by XRD analysis at RT and ambient temperature. EDX analysis of the resultant solid solution showed that the sample contained 49% Zn and 51% Ga which was almost identical to the 1:1 ratio of the ZnO and GaN staring materials. It was observed that pressure was not a determining factor for the reaction to occur but was necessary to prevent GaN from decomposing at elevated temperatures. GaN-ZnO solid solutions synthesized via this method at lower pressures were found to require higher synthesis temperatures which was attributed to the possibility of slower mixing kinetics at lower pressure. The wurtzite structure of the HPHT $(Ga_{1-x}Zn_x)(N_{1-x}O_x)$ product was found to be thermally stable upon repeated heating and cooling cycles up to 1000 ℃ at ambient pressure suggesting that the material had adopted its most stable structure. In a typical synthesis of $(Ga_{1-x}Zn_x)(N_{1-x}O_x)$ solid solutions from the ammonolysis of β-Ga_2O_3 and ZnO there is a reducing atmosphere due to the pyrolysis of NH_3 which results in a subsequent volatilization of zinc as ZnO is reduced to Zn metal, and thus a decrease in ZnO concentration (x) in the resultant solid solution. Additionally, as discussed previously GaN-ZnO solid solutions synthesized via the ammonolysis route go through an intermediate spinel $ZnGa_2O_4$ growth phase putting a theoretical limit on the ratio of Zn/Ga of 1/3 [41]. This new HPHT synthetic route does not suffer from the same limitations as there is no ammonolysis step, and thus no reducing environment and subsequent loss of Zn, and there does not appear to be an

intermediate spinel growth phase requirement. Thus it was hypothesized that $(Ga_{1-x}Zn_x)(N_{1-x}O_x)$ solid solutions at all Zn/Ga compositions could be synthesized via this HPHT route. It was determined that using Zn/Ga starting ratios of 1:1 and 3:1 lead to the formation of GaN-ZnO solid solutions with compositions of 49:51 % and 76:24 % Zn/Ga respectively confirming that the final Zn/Ga composition of the product could be controlled via this synthetic route.

Zinc *K*-edge XANES of the HPHT synthesis products showed spectra that closely resembled that of ZnO suggesting that zinc is in a local structural and electronic environment similar to ZnO. The back-transformed FT amplitude of the Zn *K*-edge EXAFS was found to decrease in both the first and second coordination shells (Zn–O and Zn–Zn absorbers respectively) vs. ZnO, however, no change in peak position was observed suggesting little distortion in the interatomic distances of Zn–O and Zn–Zn in the resultant $(Ga_{1-x}Zn_x)(N_{1-x}O_x)$ solid solution. An increase in the intensity of the white line was observed in the gallium *K*-edge spectrum of the HPHT samples vs. GaN which was interpreted as indicative of a higher presence of O atoms at N atom sites in the GaN lattice. As the ratio of Zn/Ga was increased to ~3:1 the distortion in the Ga *K*-edge XANES was observed to become more pronounced which was consistent with changes observed in the structural parameters observed via XRD. The onset of the absorption edge of HPHT synthesized GaN-ZnO samples was measured using UV-Vis diffuse reflectance spectroscopy and was observed to red-shift into the visible vs. GaN and ZnO, however, the red-shift was found to be largest (~140 nm vs. GaN) for the sample with Zn/Ga ratio of 1:1. Thus the $(Ga_{1-x}Zn_x)(N_{1-x}O_x)$ solid solution with 1:1 Zn/Ga ratio was observed to exhibit visible light absorption above 500 nm (2.48 eV) extending into the range of the peak maximum for the solar spectrum. Therefore the HPHT synthesis method was determined to be a promising route for producing $(Ga_{1-x}Zn_x)(N_{1-x}O_x)$ solid solutions with a wide range of Zn/Ga compositions.

Recent photoluminescence spectroscopic and computational investigations of GaN-rich $(Ga_{1-x}Zn_x)(N_{1-x}O_x)$ solid solutions were done by Yoshida et al. in an attempt to determine the origin of the visible light response in these materials [46]. From UV-Visible diffuse reflectance spectroscopy the onset of the absorption edge was

observed in the visible region and was slightly red-shifted with an increase in ZnO concentration (*x*). The gradual increase in absorption intensity from ~500 to 370 nm suggested that the GaN-ZnO samples were not direct band-gap semiconductors with intrinsic absorption edges. PLE spectra of the solid solutions were observed in the UV region and found to increase with decreasing wavelength from 400 to 350 nm. Since the PLE edges of the samples were observed in the UV but the absorption edges were observed in the visible the intrinsic band-gap of GaN-ZnO was attributed to the GaN component while visible light absorption was assigned to Zn-related acceptor levels. Low temperature PL emission spectra were recorded for these samples under excitation at 410 nm and showed broad emission bands around 650 nm. Under excitation at 325 nm both the emission band at ~650 nm and a new band at ~480 nm, which red-shifted slightly with increasing ZnO concentration (*x*), were observed. The PL band observed at 650 nm was assigned to radiative recombination between electrons on O donor levels below the conduction band minimum with holes on deep Ga vacancies. The PL band observed at ~480 nm was assigned to radiative recombination between electrons on O donor levels below the conduction band minimum with holes on Zn-related acceptor levels above the valence band maximum. The red-shift observed with increasing ZnO concentration in the PL band at 480 nm was attributed to a wider energy distribution of Zn-related acceptor levels as Zn doping increases. Increasing the intensity of the 325 nm excitation light was observed to enhance the emission intensity of the 480 nm PL band which was interpreted as more photogenerated holes remaining at Zn-related acceptor levels. No concomitant increase in the intensity of the PL band at 650 nm was observed which was explained as an effect of the lower density of states of energy levels associated with Ga vacancies which are thus more easily filled. From the above results the origin of visible light absorption, and thus visible light-driven photocatalytic activity, in GaN-rich $(Ga_{1-x}Zn_x)(N_{1-x}O_x)$ solid solutions was assigned to Zn-related acceptor levels while deep native Ga vacancies were identified as possible recombination centers for photogenerated electrons and holes which could decrease photocatalytic efficiency. DFT studies of non-stoichiometric models for GaN-ZnO solid solutions provided some theoretical support for the presence of Ga vacancies and/or Zn-related acceptor levels and O-derived donor levels in these materials.

The growth and electronic properties of $(Ga_{1-x}Zn_x)(N_{1-x}O_x)$ solid solution nanowires were investigated by Han et al. [49]. The nanowires were grown on Au coated (~2 nm) silicon wafers via the nitridation of $ZnGa_2O_4$ nanocrystals using NH_3 as both the nitridation source and a carrier gas for the precursor. The nanowires were observed to exhibit a wurtzite structure determined by HR-TEM with their long axis along the (100) crystal direction. The composition of the nanowires was determined to be $(Ga_{0.88}Zn_{0.12})(N_{0.88}O_{0.12})$ using a combination of EDS and electron energy loss spectroscopy (EELS). From EDS measurements spherical particles at the tip of each nanowire were found to be composed of Au containing small amounts of Ga and Zn suggesting a vapour-liquid-solid growth mechanism. The electron mobility was found to be considerably smaller than previously reported values for GaN and ZnO which was attributed to chemical distortion caused by the non-isovalent substitution of Zn^{2+} for Ga^{3+} and O^{2-} for N^{3-}. It was also suggested that the low electron mobility may have been due to Zn acting as a substitutional impurity creating deep mid-gap acceptor levels which in turn act as charge traps. The existence of charge traps in the GaN-ZnO nanowire was further supported by a slow increase and subsequent very slow decrease in photocurrent in response to illumination with UV light at 365 nm. The band-gap of the nanowires was estimated to be between 2.64 – 2.76 eV which was found to be consistent with values of the band-gap energy of 2.75 and 2.64 eV previously reported for $(Ga_{1-x}Zn_x)(N_{1-x}O_x)$ solid solutions with x = 0.1 and 0.2 respectively.

The formation of spinel zinc gallium oxy-nitrides via sol-gel synthesis at relatively low (~550 ℃) nitridation temperatures was studied by Boppana et al. [48]. It was observed that a pure spinel phase of the resultant Zn-Ga-O-N (ZGON) material was produced at a nitridation temperature of 550 ℃, however, at higher nitridation temperatures a mixture of wurtzite and spinel phases were observed, and at a synthesis temperature of 850 ℃ there was full conversion from spinel to wurtzite. ZGON samples synthesized via this method were found to absorb in the visible spectrum with band-gap energies of ~2.4–2.7 eV estimated from UV-Vis diffuse reflectance measurements. The band-gap of the resultant ZGON was observed to narrow from the pure spinel phase to the mixed spinel / wurtzite phase and then slowly widen with increasing nitridation

temperature, with all mixed phase samples exhibiting a lower band-gap than the pure spinel phase.

A shortening of the Ga-O/N interatomic distance was observed in ZGON's vs. $ZnGa_2O_4$ from Ga *K*-edge EXAFS measurements, whereas the Ga–Ga/Zn distance was found to hold constant. Shortening of the Ga–O/N interatomic distance upon nitridation of the $ZnGa_2O_4$ precursor was interpreted as Ga^{3+} occupying tetrahedral sites in a predominantly octahedral Ga^{3+} spinel structure. Subsequent neutron diffraction measurements, however, ruled out an inversion from a normal to inverse spinel (in this case via simultaneous migration of Zn^{2+} into octahedral sites and Ga^{3+} into tetrahedral sites in the crystal lattice). It was determined that Ga^{3+} ions migrated into empty interstitial tetrahedral positions from further Rietveld refinement of the neutron diffraction data which explained the decrease in Ga–O/N interatomic distance observed from Ga *K*-edge EXAFS measurements. The migration of Ga^{3+} from regular octahedral sites to interstitial tetrahedral sites was suggested to result from the formation of oxygen vacancies in the reducing ammonia synthesis environment and additionally would provide charge compensation for N^{3-} anions in the resultant ZGON. Thus it is also possible that this explains the mechanics of phase transformation from an intermediate spinel $ZnGa_2O_4$ phase to a wurtzite $(Ga_{1-x}Zn_x)(N_{1-x}O_x)$ phase solid solution upon nitridation of β-Ga_2O_3 and ZnO as previously observed by Chen et al. [41].

The synthesis of Zn-rich $(Ga_{1-x}Zn_x)(N_{1-x}O_x)$ solid solutions using layered double hydroxides as precursors was studied by Wang et al. [51]. The layered double hydroxide $Zn^{2+}/Ga^{3+}/CO_3^{2-}$ ($Zn/Ga/CO_3$ LDH's) precursors were nitridated at 800 ℃ for 30 minutes to produce $(Ga_{1-x}Zn_x)(N_{1-x}O_x)$ solid solutions. The resultant materials were found to have Zn/(Zn + Ga) ratios that were nearly identical to those of the $Zn/Ga/CO_3$ LDH precursors producing $(Ga_{1-x}Zn_x)(N_{1-x}O_x)$ solid solutions with x ranging from ~0.46 to ~0.81. The synthesis products were observed to have absorption edges in the visible and exhibited a red-shift to longer wavelength with increasing ZnO content (x) with band-gaps estimated to range from 2.37 eV (x = 0.81) to 2.60 eV (x = 0.46). This is inconsistent with previous work by Chen et al. that found a minimum in the band-gap energy of 2.48 eV at $x \approx 0.5$ for Zn-rich GaN-ZnO solid solutions synthesized via a HPHT method [44]. The XRD

patterns for $(Ga_{1-x}Zn_x)(N_{1-x}O_x)$ solid solutions synthesized using Zn/Ga/CO_3 LDH precursors exhibited very broad and weak wurtzite diffraction pattern between that of GaN and ZnO which shifted towards ZnO with increasing x suggesting poor crystallinity of the resultant synthesis products. Varying the nitridation time from 0.5 to 5 h was observed to result in an increase in crystallinity (observed as a narrowing and intensity increase of the main diffraction peaks) but a decrease in Zn content. Although it was claimed that the decrease in Zn content was much lower than that observed using the traditional synthesis method (nitridation of β-Ga_2O_3 and ZnO) a much shorter nitridation time was used. Thus although this appears to be a good method for the synthesis of Zn-rich $(Ga_{1-x}Zn_x)(N_{1-x}O_x)$ solid solutions it is possible that poor crystallinity, due to the very short nitridation time, could lead to lower photocatalytic activity due to an expected high density of photogenerated charge carrier traps and recombination centers.

Lee et al. recently reported the synthesis of $(Ga_{1-x}Zn_x)(N_{1-x}O_x)$ nanocrystals with composition (x) tunable from 0.30 to 0.87 via nitridation of a $ZnGaO_4$ and ZnO nanocrystal precursor [54]. The tunable composition was determined to be a function of the ratio of $ZnGa_2O_4$ and ZnO nanocrystals in the starting material. The synthesis products were observed to be highly crystalline from HR-TEM and XRD for compositions of $x < 0.30$. Lattice constants were observed to deviate from the linear ideal solid solution behaviour described by Vegard's law with an upward bowing of both a and c lattice parameters. The largest deviation from ideal behavior in the c lattice parameter was observed for a sample with $x = 0.54$, which is in contrast to the findings of Chen et al. for GaN-ZnO solid solutions synthesized via a HPHT method, where the smallest deviation in c from ideal behaviour was observed for a sample with $x = 0.49$ [44]. This was attributed to the difference in synthesis conditions and interpreted as a reflection of relatively long chemical bonds in the c direction of $x \sim 0.5$ samples synthesized under atmospheric conditions vs. relatively short chemical bonds in samples synthesized at high pressure and high temperature. It is also possible that this is a reflection of greater chemical disorder in these materials vs. those synthesized at high pressure and temperature. The band-gap of these materials was found to range from 2.7 eV ($x = 0.30$) to 2.2 eV ($x = 0.87$) which is consistent with the findings of Wang et al. for Zn-rich $(Ga_{1-x}Zn_x)(N_{1-x}O_x)$ solid solutions synthesized using Zn/Ga/CO_3 LDH's as precursors [51],

however, it is in contrast to the findings of Chen an co-workers for Zn-rich solid solutions produced via HPHT synthesis using GaN and ZnO precursors [44]. Since visible light absorption in GaN-ZnO solid solutions has been previously attributed to the formation of Zn-related acceptor levels, where an increase in dispersion of these levels results in a further narrowing of the band-gap, it is possible that these differences are a reflection of an increase in Zn-related acceptor levels in materials synthesized at ~atmospheric pressure [36,46].

In an attempt to provide a physical model the experimentally observed band-gap properties of these $(Ga_{1-x}Zn_x)(N_{1-x}O_x)$ solid solutions much theoretical work has been done [58- 66]. Preliminary work by Jensen et al. using DFT modeling for stoichiometric $(Ga_{1-x}Zn_x)(N_{1-x}O_x)$ solid solutions found a bowing of the band-gap over the entire compositional range with a minimum estimated at $x \approx 0.5$ [58]. It was also suggested from analysis of the computed density of states that the observed band-gap narrowing is due to both the strong 2p–3d coupling, and subsequent repulsion, between Zn and N(O) atoms in the valence band and delocalization in the bottom of the conduction band caused by volume deformation and structural relaxation. This model was further supported by Wei et al. who also suggest that band-gap narrowing in these materials is due to strong p–d repulsion between N 2p and Zn 3d states resulting in an upward shift of the valence band maximum and a subsequent narrowing of the band-gap [59].

It was also found that the substitution of Zn for Ga and N for O in GaN would cause the formation of Zn acceptor levels above the valence band and O donor levels below the conduction band providing some theoretical evidence for models previously proposed to explain the origins of visible light absorption and photoluminescence in these materials [36,46]. Work by Huda and co-workers suggests that a random alloy system is more favorable than a stoichiometric superlattice system in terms of light absorption at longer wavelengths (lower energy) [60]. They also found that because of the type-II band offset between GaN and ZnO incorporating GaN into ZnO would lead to a much more effective band-gap reduction than incorporating ZnO into GaN. Further support for this model was provided by Wang and Wang who found that although a uniform GaN/ZnO alloy can be formed it would exhibit very short range order and thus the type-II band

alignment random alloy picture more accurately describes this system [61]. Theoretical work by Di Valentin found that in dilute, i.e. ZnO-poor, $(Ga_{1-x}Zn_x)(N_{1-x}O_x)$ systems local inhomogeneity must be invoked to reproduce a red-shift in the absorption edge as experimentally observed [62]. At high ZnO concentrations, however, random alloy systems which although enthalpically more expensive are entropically more favourable were theoretically determined to be preferred and produce large reductions in band-gap energy. Work by Li et al. predicts a phase diagram for $(Ga_{1-x}Zn_x)(N_{1-x}O_x)$ with a wide miscibility gap and an ordered compound at $x = 0.5$, where the disordered phase displays strong short-range order [65]. Strong short-range order was also found to be responsible for a blue-shift in the band-gap.

Despite the numerous experimental and theoretical studies of $(Ga_{1-x}Zn_x)(N_{1-x}O_x)$ solid solutions the nature of their visible absorption properties, local chemical bonding, electronic structure, surface composition, visible emission properties, and the balance between the enthalpic cost of having a mixed valence state vs. the entropic benefit of mixing are all still unclear. There is even disagreement in both experimental and theoretical observations about the origin of band-gap narrowing as a function of ZnO concentration, or x, in $(Ga_{1-x}Zn_x)(N_{1-x}O_x)$ solid solutions where both band-gap bowing and continuous narrowing have been observed [44,51,54,58,60,62,65]. Additionally since the presence of traps and radiative recombination centers for photogenerated carriers is known to have a negative effect on photocatalytic activity it is critical to understand the origin of these defects in $(Ga_{1-x}Zn_x)(N_{1-x}O_x)$ solid solutions.

1.3 Objective and Arrangement of Thesis

It is the aim of this research to address some of the questions about the nature of $(Ga_{1-x}Zn_x)(N_{1-x}O_x)$ solid solutions, and in particular solid solution nanomaterials. This will be achieved through the use of synchrotron radiation spectroscopy, including the development of new synchrotron based techniques and their subsequent application to study the physical properties of these novel materials. Chapter two provides background information on synchrotron radiation, synchrotron-based X-ray absorption spectroscopy techniques, and relevant information about the synchrotron facilities used for this study. In chapter three soft X-ray spectroscopy is applied to study the electronic structure and

optical emission properties of a new class of ultra-thin indium doped $(Ga_{1-x}Zn_x)(N_{1-x}O_x)$ nanosheets. In chapter four a new 2-dimensional (2D) X-ray absorption – X-ray excited optical luminescence technique is described and applied to study optical luminescence properties and hard X-ray spectroscopy is used to study the electronic structure and chemical nature of both indium doped and un-doped $(Ga_{1-x}Zn_x)(N_{1-x}O_x)$ nanomaterials. Chapter five details the use of both hard and soft X-ray absorption techniques to study the nature of chemical bonding, electronic structure effects of solid solution formation, and optical luminescence properties of $(Ga_{1-x}Zn_x)(N_{1-x}O_x)$ solid solutions synthesized using different nitridation temperatures. In the first part of chapter six the development of new time-resolved X-ray excited optical luminescence (TR-XEOL) technique employing the use of an optical streak camera is described. The second part of chapter six discusses the application of this new streak camera based TR-XEOL technique to directly study the optical band-gap of $(Ga_{1-x}Zn_x)(N_{1-x}O_x)$ nanocrystals. Chapter seven provides general conclusions about the application of synchrotron radiation spectroscopy to the study of $(Ga_{1-x}Zn_x)(N_{1-x}O_x)$ nanomaterials and gives future directions for this research.

1.4 References

[1] J. A. Turner *Science*, **305**, 972, (2004)

[2] N. Z. Muradov, and T. N. Veziroglu *Int. J. Hydrogen Energy*, **33**, 6804 (2008)

[3] A. Kudo, H. Kato, and I. Tsuji *Chem. Lett.*, **33**, 1534 (2004)

[4] A. Kudo, and Y. Miseki *Chem. Soc. Rev.*, **38**, 253 (2009)

[5] X. Chen, S. Shen, L. Guo, and S. S. Mao *Chem. Rev.*, **110**, 6503 (2010)

[6] K. Maeda, and K. Domen. *J. Phys. Chem. C*, **111**, 7851 (2007)

[7] Modified from: X. Chen, S. Shen, L. Guo, and S. S. Mao *Chem. Rev.*, **110**, 6503 (2010)

[8] A. Fujishima, and K. Honda *Nature*, **238**, 37 (1972)

[9] A.J. Bard *J. Photochem.*, **10**, 59 (1979)

[10] A. J. Bard *Science*, **207**, 139 (1980)

[11] A.J. Bard *J. Phys. Chem.*, **86**, 172 (1982)

[12] J. Sato, N. Saito, H. Nishiyama, and Y. Inoue *J. Phys. Chem. B*, **105**, 6061 (2001)

[13] J. Sato, H. Kobayashi, K. Ikarashi, N. Saito, H. Nishiyama, and Y. Inoue *J. Phys. Chem. B*, **108**, 4369 (2004)

[14] G. Hitoki, A. Ishikawa, T. Takata, J. N. Kondo, M. Hara, M. Yoshimura, and K. Domen *Chem. Lett.*, **31**, 736 (2002)

[15] Y. Lee, K. Nukumizu, T. Watanabe, T. Takata, M. Hara, M. Yoshimura, and K. Domen *Chem. Lett.*, **35**, 352 (2006)

[16] G. Hitoki, T. Takata, J. N. Kondo, M. Hara, H. Kobayashi, and K. Domen *Chem. Commun.*, 1698 (2002)

[17] M. Hara, J. Nunoshige, T. Tkata, J. N. Kondo and K. Domen *Chem. Commun.*, 3000 (2003)

[18] S. Banerjee, S. K. Mohapatra, and M. Misra *Chem. Commun.*, 7137 (2009)

[19] A. Kasahara, K. Nukumizu, G. Hitoki, T. Takata, J. N. Kondo, M. Hara, H. Kobayashi, and K. Domen *J. Phys. Chem. A*, **106**, 6750 (2002)

[20] A. Kasahara, K. Nukumizu, T. Takata, J. N. Kondo, M. Hara, H. Kobayashi, and K. Domen *J. Phys. Chem. B*, **107**, 791 (2003)

[21] J. Sato, N. Saito, Y. Yamada, K. Maeda, T. Takata, J. N. Kondo, M. Hara, H. Kobayashi, K. Domen, and Y. Inoue *J. Am. Chem. Soc.*, **127**, 4150 (2005)

[22] Y. Lee, T. Watanabe, T. Takata, M. Hara, M. Yoshimura, and K. Domen *J. Phys. Chem. B*, **110**, 17563 (2006)

[23] K. Maeda, N. Saito, D. Lu, Y. Inoue, and K. Domen *J. Phys. Chem. C*, **111**, 4749 (2007)

[24] K. Maeda, N. Saito, Y. Inoue, and K. Domen *Chem. Mater.*, **19**, 4092 (2007)

[25] K. Maeda, T. Takata, M. Hara, N. Saito, Y. Inoue, H. Kobayashi, and K. Domen, *J. Am. Chem. Soc.*, **127**, 8286 (2005)

[26] K. Maeda, K. Teramura, T. Takata, M. Hara, N. Saito, K. Toda, Y. Inoue, H. Kobayashi, and K. Domen, *J. Phys. Chem.* B, **109**, 20504 (2005)

[27] M. Yashima, K. Maeda, K. Teramura, T. Takata, and K. Domen, *Chem. Phys. Lett.*, **416**, 225 (2005)

[28] M. Yashima, K. Maeda, K. Teramura, T. Takata, and K. Domen, *Mater. Trans.*, **47**, 295 (2006)

[29] K. Teramura, K. Maeda, T. Saito, T. Takata, N. Saito, Y. Inoue, and K. Domen, *J. Phys. Chem. B*, **109**, 21915 (2005)

[30] K. Maeda, K. Teramura, D. Lu, T. Takata, N. Saito, Y. Inoue, and K. Domen, *Nature*, **440**, 295 (2006)

[31] K. Maeda, K. Teramura, N. Saito, Y. Inoue, and K. Domen, *J. Catal.*, **243**, 303 (2006)

[32] K. Maeda, K. Teramura, D. Lu, T. Takata, N. Saito, Y. Inoue, and K. Domen, *J. Phys. Chem. B*, **110**, 13753 (2006)

[33] K. Maeda, K. Teramura, D. Lu, T. Takata, N. Saito, Y. Inoue, and K. Domen, *J. Phys. Chem. B*, **110**, 13107 (2006)

[34] K. Maeda, K. Teramura, D. Lu, T. Takata, N. Saito, Y. Inoue, and K. Domen, *Angew. Chem. Int. Ed.*, **45**, 7806 (2006)

[35] K. Maeda, K. Teramura, D. Lu, T. Takata, N. Saito, Y. Inoue, and K. Domen, *J. Phys. Chem. C*, **111**, 7554 (2007)

[36]T. Hirai, K. Maeda, M. Yoshida, J. Kubota, S. Ikeda, M. Matsumura, and K. Domen, *J. Phys. Chem.* C, **111**, 18853 (2007)

[37] K. Maeda, K. Teramura, D. Lu, and K. Domen, *J. Mater. Chem.*, **18**, 3539 (2008)

[38] K. Maeda, K. Teramura, and K. Domen, *J. Catal.*, **254**, 198 (2008)

[39] K. Maeda, H. Hashiguchi, H. Masuda, R. Abe, and K. Domen, *J. Phys. Chem. C*, **112**, 3447 (2008)

[40] K. Kamata, K. Maeda, D. Lu, Y. Kako, and K. Domen *Chem. Phys. Lett.*, **470**, 90 (2009)

[41] H. Chen, W. Wen, Q. Wang, J. C. Hanson, J. T. Muckerman, E. Fujita, A. I. Frenkel, and J. A. Rodriguez, *J. Phys. Chem. C*, **113**, 3650 (2009)

[42] T. Hisatomi, K. Maeda, K. Takanabe, J. Kubota, and K. Domen *J. Phys. Chem. C*, **113**, 21458 (2009)

[43] M. Mapa, K. S. Thushara, B. Saha, P. Chakraborty, C. M. Janet, R. P. Viswanath, C. M. Nair, K. V. G. K. Murty, and C. S. Gopinath, *Chem. Mater.*, **21**, 2973 (2009)

[44] H. Chen, L. Wang, J. Bai, J. C. Hanson, J. B. Warren, J. T. Muckerman. E. Fujita, and J. A. Rodriguez *J. Phys. Chem. C*, **114**, 1809 (2010)

[45] M. Yashima, H. Yamada, K. Maeda, and K. Domen *Chem. Commun.*, **46**, 2379 (2010)

[46] M. Yoshida, T. Hirai, K. Maeda, N. Saito, J. Kubota, H. Kobayashi, Y. Inoue, and K. Domen, *J. Phys. Chem.* C, **114**, 15510 (2010)

[47] W. Q. Han, Z. X. Liu, and H.G. Yu *Appl. Phys. Lett.*, **96**, 183112 (2010)

[48] V. B. R. Boppana, D.J. Doren, and R. F. Lobo, *J. Mater. Chem.*, **20**, 9787 (2010)

[49] W.Q. Han, Y. Zhang, C.Y. Nam, C.T. Black, and E.E. Mendez, *App. Phys. Lett.*, **97**, 083108 (2010)

[50] Y. C. Lee, T.Y. Lin, C. W. Wu, H. Teng, C. C. Hu, S. Y. Hu, and M. D. Yang, *J. Appl. Phys.*, **109**, 073506 (2011)

[51] J. Wang, B. Huang, Z. Wang, P. Wang, H. Cheng, Z. Zheng, X. Qin, X. Zhang, Y. Dai, and M. H. Whangbo, *J. Mater. Chem.*, **21**, 4562 (2011)

[52] E.J. McDermott, E.Z. Kurmaev, T.D. Boyko, L.D. Finkelstein, R.J. Green, K. Maeda, K. Domen, and A. Moewes, *J. Phys. Chem.* C, **116**, 7694 (2012)

[53] T. Ohno, L. Bai, T. Hisatomi, K. Maeda, and K. Domen *J. Am. Chem. Soc.*, **134**, 8254 (2012)

[54] K. Lee, B. M. Tienes, M. B. Wilker, K. J. Schnitzenbaumer, and G. Dukovic, *Nano Lett.*, **12**, 3268 (2012)

[55] E. Ejder, *Phys. Status Solidi* , **6**, 445 (1971)

[56] V. Srikant, and D. R. Clarke, *J. Appl. Phys.*, **83**, 5447 (1998)

[57] S. H. Wei, and A. Zunger *Phys. Rev. B*, **37**, 8958 (1998)

[58] L. L. Jensen, J. T. Muckerman, and M. D. Newton *J. Phys Chem. C*, **112**, 3439 (2008)

[59] W. Wei, Y Dai, K Yang, M. Guo, B. Huang *J. Phys Chem. C*, **112**, 15915 (2008)

[60] M. N. Huda, Y. Yan, S. H. Wei, and M. M. Al-Jassim *Phys. Rev. B*, **78**, 195204 (2008)

[61] S. Wang, and L. W. Wang *Phys. Rev. Lett.*, **104**, 065501 (2010)

[62] C. Di Valentin *J. Phys Chem. C*, **114**, 7054 (2010)

[63] S. Wang, and L. W. Wang *Phys. Rev. B*, **83**, 115208 (2011)

[64] H. G. Yu *Chem. Phys. Lett.*, **512**, 213 (2011)

[65] L. Li, J. T. Muckerman, M. S. Hybertsen, and P. B. Allen *Phys. Rev. B*, **83**, 134202 (2011)

[66] M. Dou, G. Baldissera, and C. Persson *J. Cryst. Growth*, **350**, 17 (2012)

Chapter 2

2 Introduction to Synchrotron Radiation Spectroscopy

Synchrotron radiation spectroscopy is a powerful tool for the study of complex semiconducting nanostructures such as $(Ga_{1-x}Zn_x)(N_{1-x}O_x)$ solid solutions. In section 2.1 the basics of synchrotron radiation and synchrotron light sources, including a brief historical perspective, are discussed. Section 2.2 provides a description of X-ray absorption and de-excitation processes and discusses related spectroscopic techniques. In section 2.3 the synchrotron facilities used in this thesis work, the Canadian Light Source and the Advanced Photon Source are briefly described. The beam-lines used to collect all of the X-ray absorption data presented in this thesis are discussed in section 2.4. Modes of detection are briefly discussed in section 2.5.

2.1 Synchrotron Radiation and Synchrotron Light Sources

2.1.1 Synchrotron Radiation

Synchrotron radiation is the highly collimated intense light that is emitted when charged particles (electrons, positrons, and protons etc.) are travelling around an orbit at relativistic speeds (close to the speed of light ~3 x 10^8 m/s) [1]. This radiation is produced by transverse acceleration of the charged particles due to the magnetic field in bending magnets (which form the circular orbit for the charged particles, Figure 2-1(a)) or by period acceleration of the charged particles due to the alternating magnetic field in insertion devices such as undulators and wigglers (Figure 2-1(b) and (c) respectively).

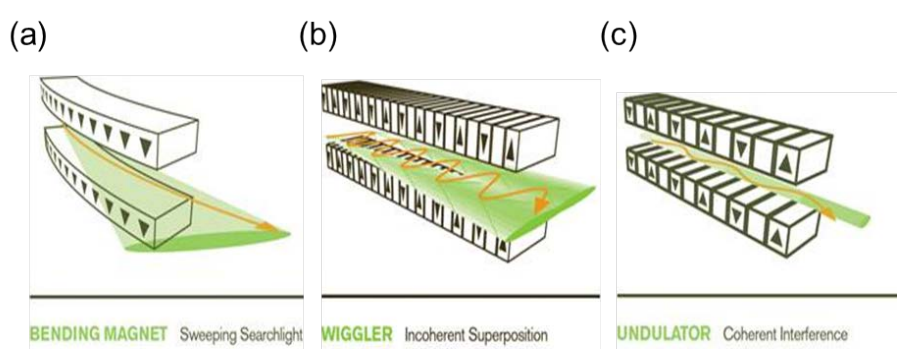

Figure 2-1 Schematic of a (a) Bending magnet, (b) Wiggler, and (c) Undulator [2].

Synchrotron radiation emitted tangentially to the orbit of an electron on a circular path was described by Larmor using a classical treatment of an accelerated charged particle [3]. The acceleration of electrons, either in bend magnets, wigglers or undulators, causes a perturbation of their electric fields which travel away from the electrons at close to the speed of light producing the electromagnetic "synchrotron" radiation that is observed. The power radiated by a relativistic electron is given by

$$P = \frac{2e^2 c E_e^4}{3(m_0 c^2)^4 \rho^2} \tag{2-1}$$

where e is the charge of the electron, c is the speed of light, E_e is the energy of the electron in GeV, and ρ is the radius of curvature of the electron orbit. The ratio γ of the mass, m, of a relativistic electron to its rest mass, m_0, is given by

$$\gamma = \frac{E_e}{m_0 c^2} = \frac{1}{\sqrt{1 - \frac{v^2}{c^2}}} = \frac{1}{\sqrt{1 - \beta^2}};\ \beta = \frac{v}{c};\ (1 - \beta) \cong \frac{1}{2\gamma^2} \tag{2-2}$$

where v is the speed of the electron. Thus for non-relativistic electrons $\beta \sim 0$ and $\gamma = 1$ and for relativistic electrons $\beta \sim 1$ and $\gamma = 1957\ E$ (GeV). Bending magnet radiation is produced when a relativistic electron experiences centripetal acceleration as it passes through a uniform magnetic field producing a broad fan of radiation directed tangentially (with respect to the orbit of the electron) outward in a narrow cone which gives the appearance of a sweeping "searchlight". The conical shape of synchrotron radiation is due to the relativistic Lorentz contraction (a relativistic Doppler shift) experienced by the electric field of the electron as its speed approaches the speed of light. The spectrum of bending magnet radiation is very broad, analogous to a "white light" X-ray light bulb covering most of the radiation spectrum from infra-red (meV) to gamma rays (MeV). For a bending magnet the opening angle of the radiation cone is typically on the order of $1/\gamma$, where γ is the Lorentz contraction factor (Figure 2-2(a)). Undulator radiation is produced when a relativistic electron passes through a periodic magnetic field in the undulator limit (relatively weak field) causing the electron to undulate through excursions smaller than the angular width of the natural cone of synchrotron radiation, $1/\gamma$, to produce a characteristic emission angle of $1/\gamma\sqrt{N}$ (where N is typically of the order of 100). The resultant frequency spread of undulator radiation is very narrow and can be extremely

bright and partially coherent (Figure 2-2(b)). Wiggler radiation is also produced using a periodic magnetic structure but in the strong magnetic field limit which produces wiggles in the photon beam that are significantly greater than the natural cone of synchrotron radiation (1/ γ). Since the acceleration of the electrons is stronger in this limit wiggler radiation produces peaks at higher photon energies in greater abundance which results in a higher photon flux and more radiated power (Figure 2-2(c)).

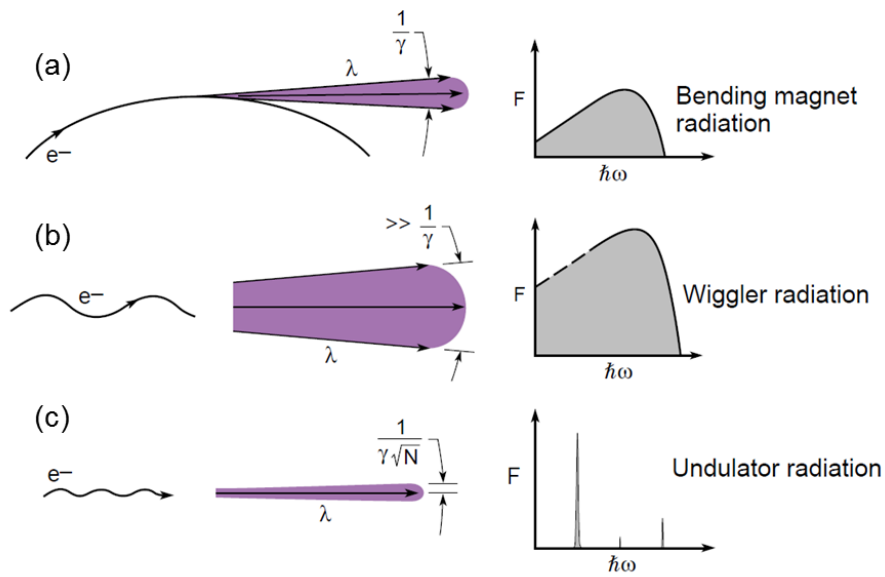

Figure 2-2 Opening angle and flux (vs. E_{photon}) of (a) bending magnets, (b) wigglers, and (c) undulators [4].

From the preceding discussion it is implied that the higher the electron energy (E_e) in the storage ring, the higher the power radiated, the brighter the synchrotron light, and the smaller the opening angle of the emitted radiation.

2.1.2 Synchrotron Light Sources

Synchrotron radiation (SR) was first observed experimentally in 1946 at the General Electric Laboratories in Schenectady NY by Elder et al. [5]. This radiation was at first considered a nuisance because its emission limited the energy achievable by electron accelerators, such as the betatron accelerator [6]. The potential of synchrotron

radiation as a powerful tool for ultraviolet, soft X-ray, and hard X-ray experiments was not recognized until the 1950's [7,8]. Due to the immense cost involved with building a synchrotron radiation facility early experiments were carried out in a "parasitic" mode on high energy physics accelerators. These so called first generation sources were not ideal as their operational parameters were set by the requirements of the elementary-particle physics research that they were designed for. The first dedicated electron synchrotron storage ring, Tantalus I, was commissioned in 1968. The introduction of a dedicated electron storage ring was a great advancement in the field as it provided a continuous source of photons that could be used in synchrotron radiation experiments. Second generation sources such as Aladdin (USA), NSLS (USA), and Bessy I (Germany) soon followed. With the development of insertion devices (undulators and wigglers) came third generation sources such as the 7 GeV Advanced Photon Source at Argonne National Laboratory, Argonne, IL and the 2.9 GeV Canadian Light Source in Saskatoon, SK where research for this thesis was conducted. Figure 2-3 shows the layout of a typical synchrotron radiation facility.

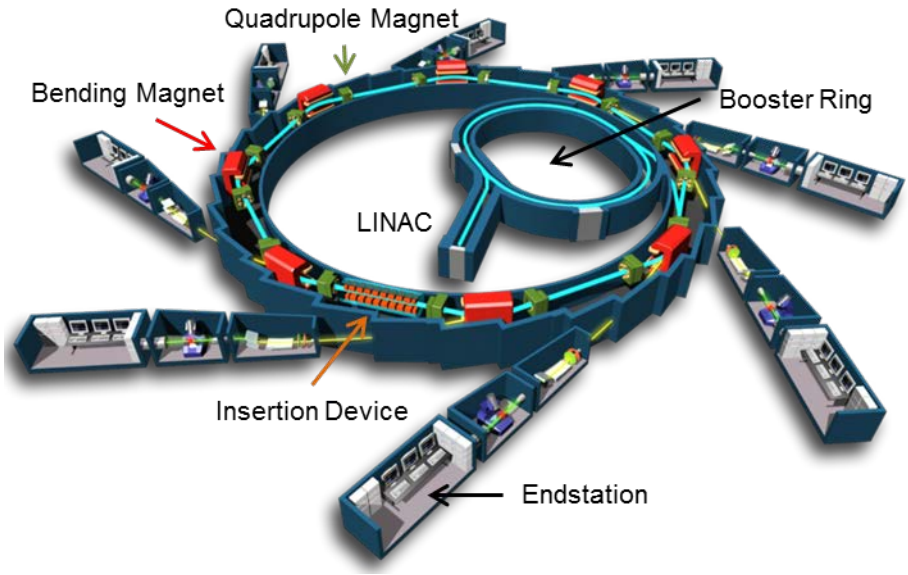

Figure 2-3 Layout of typical synchrotron facility [9].

Electrons, which are emitted by heating a cathode to ~1000 ℃ using high voltage DC, are fed into a linear accelerator (LINAC). In the LINAC electrons are accelerated to a velocity nearing the speed of light with energy of hundreds of MeV (250 MeV at CLS). The electrons are then injected into a booster synchrotron where they are accelerated further by a radio frequency (RF) cavity to 99.9999985% the speed of light with energy on the order of GeV (2.9 GeV at CLS) [10]. The high energy relativistic electrons are then injected into the storage ring where they circulate producing photons. Bending magnets are used both to maintain the circular orbit of the electrons in the storage ring and to produce SR radiation for use in experiments. Quadrupole magnets are used to "squeeze" the electron beam to maintain its transverse dimensions. An RF cavity in the storage ring restores energy that is lost by the electrons through the emission of SR by "pushing" the electrons using an alternating electric field much like a surfer gaining energy from a wave which allows electrons to be stored in the ring for a period of hours. Insertion devices, such as undulators and wigglers, are placed in straight sections of the storage ring to produce SR radiation for use in experiments. The SR radiation produced by bending magnets, wigglers, and undulators is then directed into beam-line optics for use at experimental endstations. The beam-lines used for this research will be discussed in section 2.4 of this chapter. Synchrotron radiation (SR) has many advantages over conventional X-ray sources [11]: (1) SR is highly tunable using monochromators from IR (meV) to γ-rays (~MeV); (2) SR has high flux, up to 10^{12} times greater than conventional sources; (3) SR is bright, that is the flux per unit area per solid angle is large; (4) SR is highly focused and can be partially coherent giving increased spatial resolution; (5) SR is linearly polarized in the plane of orbit and elliptically polarized above and below the plane; and (6) the pulsed and ultra-stable time structure of SR (electrons travel in tight bunches forming nanosecond or sub-nanosecond pulses with microsecond to nanosecond gaps between pulses) makes it suitable for time-resolved studies.

2.2 X-ray Absorption Spectroscopy

When X-rays interact with matter they can either be totally or partially absorbed. In this process, which is known as the *photo-electric effect*, an X-ray photon with energy greater than the binding energy of a tightly bound deep core-level electron is absorbed and an electron is ejected from the atom. The ejected electron has kinetic energy equal to the energy of the incident X-ray minus the binding energy of the electron. The probability that X-rays will be absorbed is described by Beer's Law

$$I = I_0 e^{-\mu t} \tag{2-3}$$

where I_0 is the intensity of the incident X-rays, I is the intensity of X-rays transmitted through the sample, t is the sample thickness, and μ (cm^{-1}) is the absorption coefficient. Beer's Law (Equation 2-3) can be rewritten in terms of μ as a function of X-ray energy E as

$$\mu(E)t = \log\left(\frac{I_0}{I}\right) \tag{2-4}$$

The X-ray absorption coefficient is a smooth function of energy that is dependent on the sample density ρ (g/cm^3), the atomic number Z, the atomic mass A, and the energy of the X-ray E as

$$\mu \approx \frac{\rho Z^4}{AE^3} \tag{2-5}$$

The strong dependence of the absorption coefficient on both the atomic number and the energy of the X-ray is one of the fundamental properties of X-rays and this defines why X-ray absorption spectroscopy is such a powerful tool. The absorption coefficient can also be written as a function of the X-ray cross section, σ (cm^2/g), as

$$\mu = \sigma \cdot \rho \tag{2-6}$$

As the energy of the incident X-rays approaches the binding energy of a core level electron there is a sharp rise in the absorption coefficient as the cross section of the X-ray increases. This gives rise to experimentally observed absorption edges when an X-ray has sufficient energy to promote a core level electron into unoccupied bound states, quasi-

bound states, or the continuum (*photoelectric effect*). The atomic mass photoabsorption cross section of platinum metal as a function of X-ray energy is shown in Figure 2-4. The appearance of several absorption edges, labeled L_3, L_2, L_1, and K respectively, corresponding to core level electrons at different energy levels is observed. The K-edge refers to the excitation of 1s electrons, the L_1-edge refers to excitation of 2s electrons, and the L_3- and L_2-edges refer to the excitation $2p_{3/2}$ and $2p_{1/2}$ electrons respectively. Due to the high degree of sensitivity of μ to the atomic number Z each element has characteristic absorption edges at different X-ray energies. This allows almost all elements in the periodic table to be probed using this technique since as mentioned in section 2.1.1 synchrotrons are capable of producing intense X-rays with energies in the range of far IR to gamma rays.

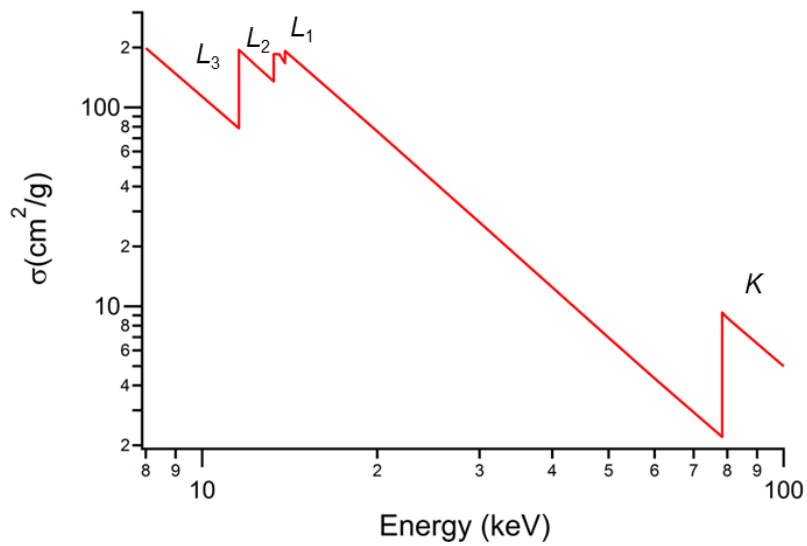

Figure 2-4 Log-log plot of the mass photoabsorption coefficient σ of platinum as a function of X-ray photon energy [12].

When core level electrons in an atom are excited with X-ray energies at the binding energy, or absorption threshold (E_0), there is a sharp rise in the absorption probability, or μ, followed by a monotonic decrease until the next core level is excited (Figure 2-5(a)).

The wavelength of the outgoing photoelectron can be expressed as

$$\lambda \sim \sqrt[-1]{(E - E_0)} \tag{2-7}$$

In a diatomic system, however, fine structures are observed in μ when outgoing photoelectrons of the absorbing atom interact with neighbouring atoms resulting in scattering and subsequent constructive and destructive interference of the outgoing and scattered wavefunctions (Figure 2-5(b)). The modulation of the absorption coefficient as a function of X-ray excitation energy when the absorbing atom is in a chemical environment is known as X-ray absorption fine structure (XAFS). XAFS is further divided into two regions; (1) the near-edge region which extends from ~20 eV below to 50 eV above the absorption edge is referred to as X-ray absorption near edge structure (XANES), and (2) the extended region which extends from ~ 50 eV to 1000 eV above the absorption edge is referred to as extended X-ray absorption fine structure (EXAFS). This division is due to the difference in scattering behavior of the electron as a function of its kinetic energy. In the near-edge region electronic transitions into bound and quasi-bound states and multiple scattering off of neigbouring atoms all contribute to the modulation of the absorption coefficient μ.

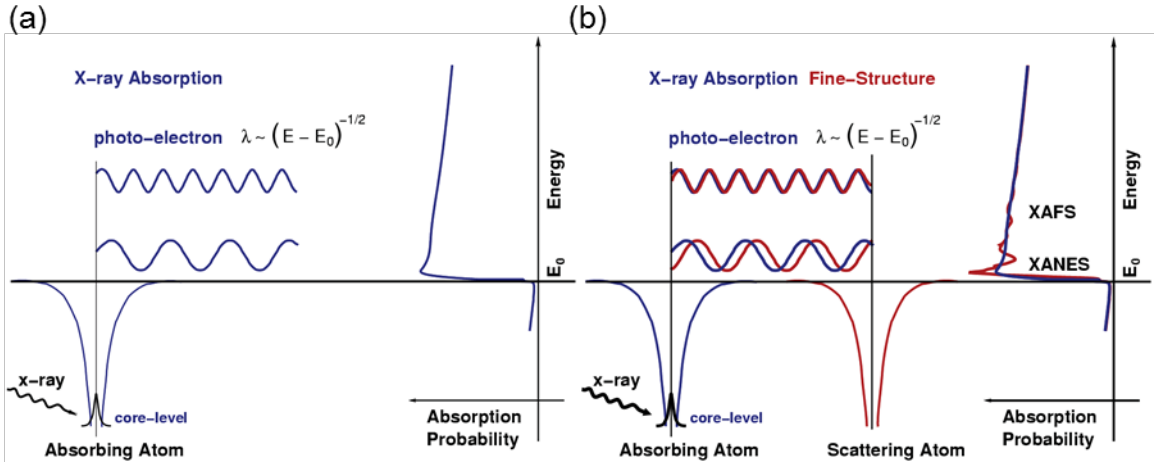

Figure 2-5 (a) X-ray absorption in a single atom system, and (b) X-ray absorption fine structure (XAFS) in a multi-atom system [13].

This makes XANES a very sensitive probe of the local chemical environment (oxidation state, unoccupied density of states, and local symmetry) of the absorbing atom. In the extended region single scattering dominates the modulation of μ which makes EXAFS a local probe (within ~5 Å or the first two or three atomic shells) of bond length and short range order. Therefore XAFS is a powerful tool for the study of both the chemical environment and local structure of an absorbing atom. In this thesis most of the work presented is focused on the XANES region but EXAFS is also used in both chapter 4 and chapter 5 as a qualitative probe of local chemical environment. A description of both of these processes follows.

2.2.1 X-ray Absorption Near Edge Structure (XANES)

In the XANES region the incident X-ray photon energy is equal to or just above (~10's of eV) the absorption threshold E_0 resulting in transitions of the core-level electron into previously bound and quasi-bond states. In a multi-atom system there are scattering contributions to the absorption coefficient μ from all the neighbouring atoms resulting in multiple scattering pathways. The total absorption coefficient μ can be written as a function of energy as

$$\mu(E) = \mu_0 \left[1 + \sum_{n\geq 2} \chi_n(E)\right] \tag{2-8}$$

where μ_0 is the atomic absorption coefficient, n is the number of atoms, and $\chi_n(E)$ contains contributions to the absorption coefficient from all scattering pathways of $n - 1$ neighbouring atoms. A cartoon representation of the multiple scattering processes in a multi-atom system is shown in Figure 2-6. Thus there is a strong effect on the amplitude and spectral shape of the XANES spectrum by the local symmetry, crystal structure, and type of the absorbing atoms.

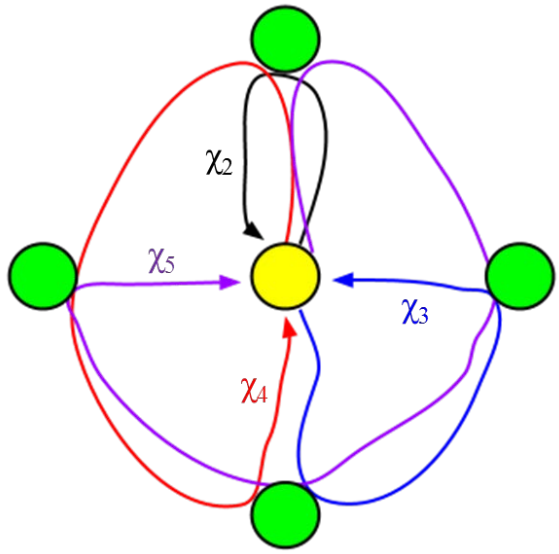

Figure 2-6 Multiple scattering process, where *n* represents the number of atoms in each scattering pathway χ_n.

The absorption coefficient, $\mu(E)$, is in theory proportional to the probability that an X-ray photon will be absorbed by an electron in the absorbing atom producing a transition between initial and final quantum states as described by Fermi's Golden Rule

$$\mu(E) \approx \left|\langle\psi_i|H|\psi_f\rangle\right|^2; H = (\hat{\varepsilon}\cdot\vec{r})e^{\left(i(\hat{k}\cdot\vec{r})\right)} \tag{2-9}$$

where ψ_i is the initial state function which describes a core-level electron, X-ray photon, and no photoelectron; ψ_f is the final state function which describes a photoelectron, *core-hole*, and no X-ray; and H is the interaction Hamiltonian between the electromagnetic field of the X-ray and the electron. The Hamiltonian expression includes the electric field vector of the X-ray ε, the forward scattering vector k, and the electron coordinate vector r. If we further expand the Hamiltonian we get

$$H = (\hat{\varepsilon}\cdot\vec{r}) + (\hat{\varepsilon}\cdot\vec{r})\left(\hat{k}\cdot\vec{r}\right) + \cdots \tag{2-10}$$

XANES is dominated by the first term in Equation 2-10 which is the dipole component, giving rise to transitions of core-level electrons from 1s to p final states (K-edge) and 2p to s + d final states ($L_{3,2}$-edges), etc. which follow the dipole selection rule ($\Delta l = \pm 1$ and

$\Delta j = 0$). Although the quadrupole component (the second term of Equation 2-10) is several orders of magnitude weaker it is highly sensitive to metal d-electron–ligand hybridization and gives a strong contribution to the *K*-edge XANES of transition metals which are observed as weak pre-edge features before the main absorption edge [14,15].

An alternative description of XANES is given by the band structure theory approach described by Muller and Wilkins [16], where the X-ray energy dependence of the absorption coefficient μ can be described as

$$\mu(E) = \frac{4\pi^2\alpha}{\Omega/_{v}} F(E) \tag{2-11}$$

where α is the inverse fine structure constant ($\alpha^{-1} = 137.036$), Ω is the primitive cell volume, v is the number of atoms that contribute to the primitive cell, and $F(E)$ is the spectral distribution of the oscillator strength. $F(E)$ contains contributions from both atomic and solid state terms. The observed magnitude and shape of the XANES spectrum is determined by the atomic transition of a core-level electron and fine structure in the spectrum is determined by the solid state term which is proportional to the projected density of states.

2.2.2 Extended X-ray Absorption Fine Structure (EXAFS)

In EXAFS we are concerned with oscillations in the absorption coefficient that are well above the absorption edge (~50 to 1000 eV above) where single scattering dominates. The EXAFS fine-structure function $\chi(E)$ can be defined as

$$\chi(E) = \frac{\mu(E) - \mu_0(E)}{\Delta\mu_0(E)} \tag{2-12}$$

where $\mu(E)$ is the experimentally measured absorption coefficient, $\mu_0(E)$ is a smooth background function representing the absorption of the X-ray by an isolated atom, and $\Delta\mu_0(E)$ is the measured jump in absorption at the threshold energy (the binding energy of the core-level electron) E_0 [17].

Since EXAFS is best described by the wave behavior of the photoelectron created in the X-ray absorption process it is common to convert the X-ray energy to *k* which is the wave number of the photoelectron in dimensions of Å^{-1} which is defined as

$$k = \sqrt{\frac{2m_e(E - E_0)}{\hbar^2}} \tag{2-13}$$

where m_e is the electron mass. Thus the primary quantity for EXAFS is $\chi(k)$ which is a measure of the oscillations in the absorption coefficient as a function of the photoelectron wave number *k*, and $\chi(k)$ is often referred to as "the EXAFS". A typical gallium *K*-edge XAFS spectrum of GaN is shown in Figure 2-7(a). The EXAFS region (well above the absorption threshold) is oscillatory and decays rapidly as a function of *k*. To emphasize the oscillations, $\chi(k)$ is usually multiplied by a power of *k*. Weighting $\chi(k)$ with lower powers of *k* emphasizes oscillations in the low *k* region and with higher powers of *k* emphasizes oscillations in the high *k* region (Figure 2-7(b)).

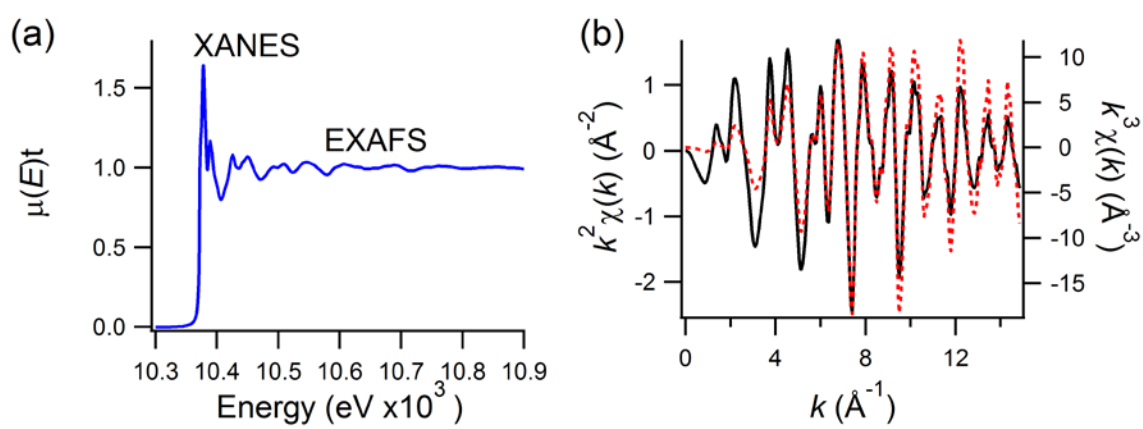

Figure 2-7 (a) Ga *K*-edge XAFS of GaN. (b) k^2-weighted (black line) and k^3-weighted (red dashed line).

The final state ψ_f, which describes a *core-hole* and a photoelectron, however, will be affected by the neigbouring atom because the outgoing photoelectron will be able to "see" it [18]. We can thus further expand ψ_f into two parts, one that represents the final

state of the "bare atom" (ψ_0), and one that represents the change in the final state of the photoelectron due to backscattering from the neigbouring atom (ψ_{scatt})

$$\left|\psi_f\right\rangle = |\psi_0\rangle + |\psi_{scatt}\rangle \tag{2-14}$$

We can then expand Equation 2-9 to give

$$\mu(E) \propto \ |\langle\psi_i|H|\ \psi_0\ \rangle|^2 \left[1 + \frac{\langle\psi_i|H|\ \psi_{scatt}\ \rangle\langle\psi_0|H|\ \psi_i\ \rangle^*}{|\langle\psi_i|H|\ \psi_0\ \rangle|^2} + C.C.\right] \tag{2-15}$$

where *C.C.* is the complex conjugate. From Equation 2-15 we can see that the fine structure,$\chi(E)$, can be rewritten as

$$\chi(E) \propto \ \langle\psi_i|H|\ \psi_{scatt}\ \rangle \tag{2-16}$$

Since the initial state for a tightly bound core-level electron can be approximated by a delta function we can get an expression for the EXAFS

$$\chi(E) \propto \int dr\delta(r)\, e^{ikr}\psi_{scatt}(r) = \ \psi_{scatt}(0) \tag{2-16}$$

We can describe Equation 2-16 in words simply as "The EXAFS $\chi(E)$ is proportional to the amplitude of the scattered photoelectron at the absorbing atom" [18]. The outgoing photoelectron wave-function $\psi(k,r)$ can be described as a spherical wave

$$\psi(k,r) = \ \frac{e^{ikr}}{kr} \tag{2-17}$$

which travels a distance *R* to a neigbouring atom, scatters off the neighbouring atom, and then travels a distance *R* back to the absorbing atom. We can multiply all of these factors together to get

$$\chi(k) \propto \psi_{scatt}(k, r = 0) = \ \frac{e^{ikr}}{kr}\left[2kf(k)e^{i\delta(k)}\right]\frac{e^{ikr}}{kr} + C.C. \tag{2-18}$$

If we combine all of the factors in Equation 2-18 and include the complex conjugate (*C.C.*) to obtain a real function we get the following equation for the EXAFS

$$\chi(k) = \frac{f(k)}{kR^2}\sin[2kR + \delta(k)] \tag{2-18}$$

Of course in a real measurement even for atoms of the same type we must consider averaging over millions of pairs of atoms which, due to thermal and static disorder, will give a range of bond distances that will affect the EXAFS

$$\chi(k) = \frac{Ne^{-2k^2\sigma^2} f(k)}{kR^2} \sin[2kR + \delta(k)] \tag{2-19}$$

where N is the coordination number of the absorbing atom and σ^2 (Å^2) is the mean-square-displacement (also known as the Debye-Waller factor) in the bond distance R [18]. In most real systems there is usually more than one type of neighbouring atom and thus the EXAFS will be a sum of the contributions from each scattering atom type (or coordination shell)

$$\chi(k) = \sum_j \frac{N_j e^{-2k^2\sigma_j^2} f_j(k)}{kR_j^2} \sin\left[2kR_j + \delta_j(k)\right] \tag{2-19}$$

where j represents the individual coordination shell of identical scattering atoms which are at approximately the same distance R_j from the absorbing atom. In order to account for both inelastic scattering of the photoelectron (by other conduction band electrons, phonons, etc.) and the *core-hole lifetime* we should replace the spherical wave of the photoelectron with a damped spherical wave

$$\psi(k,r) = \frac{e^{ikr} e^{-2r/\lambda(k)}}{kr} \tag{2-20}$$

where λ is the mean-free-path of the photoelectron (typically ~5 to 30 Å) which has a significant but fairly universal dependence on k [18]. If we also consider an amplitude reduction term, S_0^2, which accounts for reduction in the EXAFS amplitude due to the many-body effects of the relaxation of other electrons in the absorbing atom after the creation of a *core-hole* we can get a final equation for the EXAFS [17]

$$\chi(k) = \sum_j \frac{N_j S_0^2 e^{-2k^2\sigma_j^2} e^{-2R_j/\lambda(k)} f_j(k)}{kR_j^2} \sin\left[2kR_j + \delta_j(k)\right] \tag{2-21}$$

From Equation 2-21 we can see that EXAFS is an inherently local probe which is not able to "see" much past ~5 Å from the absorbing atom due to the (k) term and the R^{-2} term. Also the EXAFS oscillations will consist of different frequencies corresponding to different distances from the absorbing atom to each coordination shell, and thus, Fourier

transformation is required to extract these distances. In this thesis EXAFS is used primarily in a qualitative fashion to identify the local short range chemical environment of an absorbing atom and to make comparisons about the short range order. Thus a detailed explanation of EXAFS data reduction to obtain accurate values of *R* and *N* will not be included.

2.2.3 De-excitation Processes

After a core-level electron is excited by the annihilation of an X-ray through the process of photoionization (Figure 2-8(a)), there is a subsequent relaxation of the excited state through de-excitation processes. The de-excitation process can be radiative in the form of X-ray fluorescence (Figure 2-8(b)) and non-radiative in the form of Auger decay (Figure 2-8(c)) followed by secondary processes (Figure 2-8(d)).

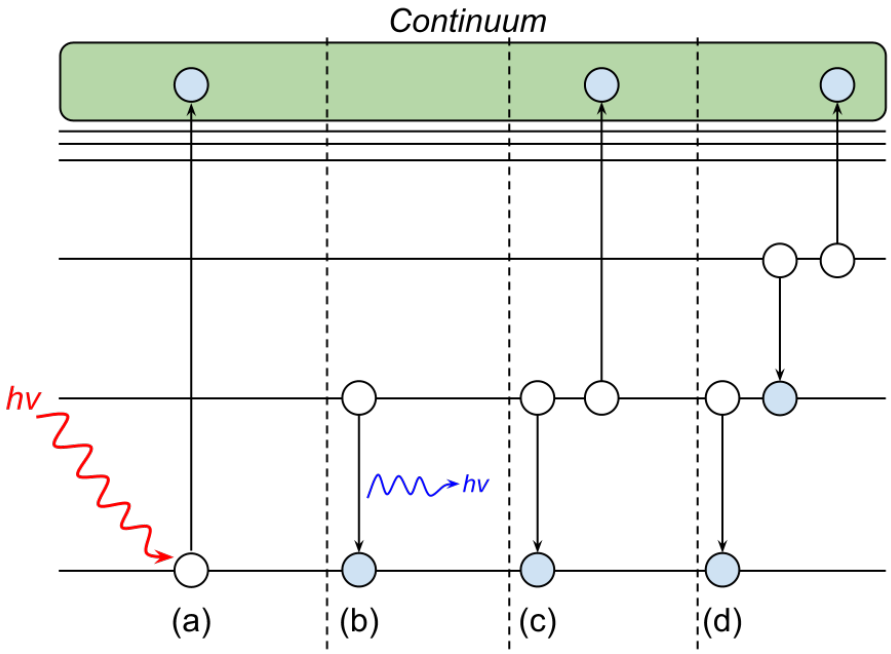

Figure 2-8 X-ray excitation of a core-level electron and subsequent de-excitation processes: (a) photoionization of a core-level electron producing a photoelectron and core-hole; core-hole decay (b) producing fluorescent X-rays, (c) Auger electrons, and (d) secondary electrons.

In X-ray fluorescence decay a shallower core-level electron fills the *core-hole* created by the photoionization process releasing energy in the form of a fluorescent X-ray (dipole selection rules). In Auger decay a shallower core-level electron fills the *core-hole* releasing energy by transferring it to another core-level or valence electron ejecting it into the continuum. In secondary processes there is a cascade of shallower level electrons filling holes created through the de-excitation process which eventually results in the transfer of energy to very shallow core-level or valence level secondary electrons which are subsequently ejected into the continuum. Unlike the direct relationship between the energy dependence of the absorption coefficient, $\mu(E)$ and the intensity of the transmitted X-rays in Beer's Law (see Equation 2-4) there is a proportional relationship between $\mu(E)$ and the yield of photoelectrons, fluorescent X-rays, Auger electrons, and secondary electrons produced in the de-excitation process. Thus we can express this mathematically as

$$\mu(E)t \propto I_{yield} \tag{2-22}$$

where μ is the absorption coefficient, E is the excitation energy, t is the sample thickness, and I_{yield} is the photoelectron, fluorescent X-ray, Auger electron, or secondary electron yield. In practice contributions to I_{yield} by photoelectrons, Auger electrons, and secondary electrons are measured simultaneously as the total electron yield (TEY). Auger and fluorescence decay are competing processes that are both proportional to the absorption coefficient μ and directly related to the probability of the creation of a *core-hole* through the absorption of an X-ray [19]. Auger decay is the dominant process for low Z elements and fluorescence X-ray decay is the dominant process for high Z elements [19]. We can write an expression for the proportional relationship between the TEY and the absorption coefficient $\mu(E)$

$$I_{TEY} \propto fcI_0\left(1 - e^{-\mu(E)t}\right) \tag{2-22}$$

where I_{TEY} is the intensity of the TEY signal, c is constant function (for a given thickness and photon energy) proportional to the X-ray photon energy, and f is the probability that an electron will be detected after being created at a distance t from the sample surface

$$f = e^{-t/\lambda(E)} \tag{2-23}$$

where $1/\lambda(E)$ is the electron attenuation coefficient (or the electron absorption coefficient), it follows that $\lambda(E)$ is the electron attenuation length [20]. Thus it can be seen that TEY is an inherently surface sensitive technique probing ~2–10 nm into the sample according to the universal curve of the inelastic mean free path (IMFP) of electrons as a function of kinetic energy. TEY can suffer from charging effects resulting in a subsequent loss of proportionality to $\mu(E)$. Fluorescence yield (FY) is also proportional to $\mu(E)$ and the same general relationship in Equation 2-21 applies, but, f is now the attenuation length of the fluorescent X-ray which is quite large in comparison to Auger and secondary electrons making FY a bulk sensitive technique. FY can suffer from self-absorption effects if the sample is too thick (i.e. if t, the sample thickness, is not much less than the absorption length, $1/\mu$, of the X-ray).

2.2.4 X-ray Excited Optical Luminescence (XEOL)

The first observation of X-ray excited optical luminescence (XEOL) coincided with the discovery of X-rays by Röntgen in 1895, and has commonly been used to “see” X-rays [21]. XEOL is an X-ray-photon in optical-photon out process which is similar to photoluminescence (PL), but, instead of measuring the de-excitation process of electrons excited from the valence band into the conduction band XEOL measures the de-excitation process after a deep core-level electron is excited by an X-ray into the conduction band. XEOL is used to monitor the optical luminescence (UV–Vis–NIR) excited using a selected X-ray photon energy, which can excite a particular core-level electron of a given element of interest to bound, quasi-bound, and continuum states, providing elemental, and in some cases site specificity [22-24]. The energy absorbed is in part transferred to optical de-excitation channels, resulting in optical luminescence (see Figure 2-9). XEOL can also be used as a mode of detection for tracking the modulation of the absorption coefficient as a function of excitation energy, $\mu(E)$ which is known as optical-XAFS or photoluminescence yield (PLY) [25], but, this method of detection is non-trivial due to both thickness and self-absorption effects. As the name suggests PLY is

a yield mode of detection (see Equation 2-22 and the discussion that follows) and thus is proportional to the absorption coefficient, $\mu(E)$.

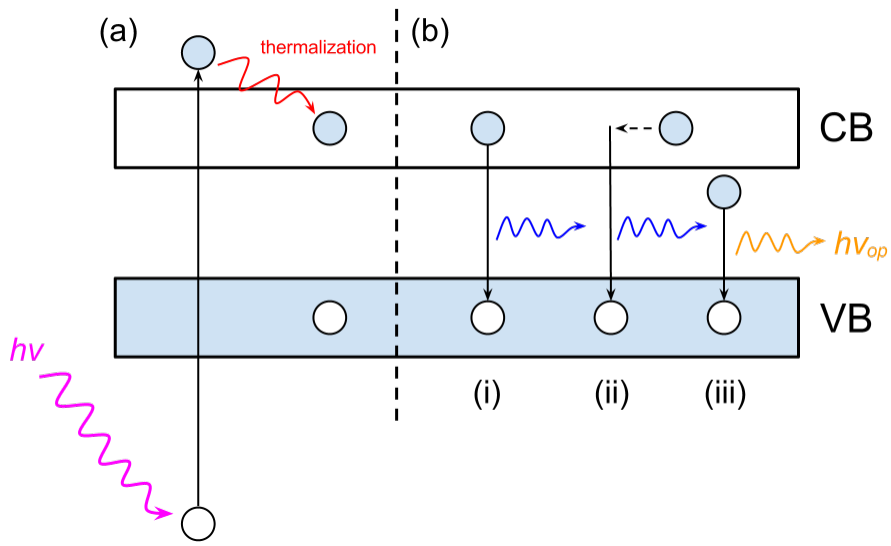

Figure 2-9 Diagram of electron-hole pair formation and radiative recombination processes. (a) Core-level electron is excited by X-ray photon with subseqent electron-hole thermalization. (b) Examples of radiative recombination; (i) direct recombination, (ii) indirect (i.e. phonon assisted, $\Delta k \neq 0$) recombination, and (iii) defect (i.e. traps, vacancies, impurities, etc.) recombination.

Due to the high-energy of the incident X-rays, and subsequently the core-level photoelectrons, the XEOL process is a complex phenomenon which can be generally described as follows [26]; (1) a *core-hole* is created within femtoseconds by the annihilation of an X-ray (Figure 2-9(a)), (2) the *core-hole* is immediately filled by electrons from shallower levels via Auger and X-ray fluorescence, (3) the new shallower *core-holes* left behind are filled by even shallower core or valence electrons which creates a cascade process, (4) the energetic photoelectrons and Auger electrons create more electrons and holes in their tracks as they travel through the absorbing medium and lose energy through inelastic scattering (thermalization), (5) electrons and holes (i.e. in semiconductors) thermalize at the bottom of the conduction band (CB) and top of the valence band (VB) respectively (still relatively fast, i.e. sub-picosecond), and (6)

electrons and holes in the CB and VB respectively radiatively recombine (Figure 2-8(b) (i) direct and (ii) indirect radiative recombination) to produce luminescence with photon energy close to the band-gap and a short lifetime (on the order of nanoseconds to sub-nanosecond). Additionally defects (Figure 2-9(b) defect recombination (iii)) can produce intense optical emission with photon energy significantly lower than the band-gap and a relatively long lifetime (hundreds of nanoseconds to microseconds). Thus XEOL is different from conventional UV-visible photoluminescence in that it can be site specific since the core-level is specific to a given element and that it involves energy transfer via secondary processes to the optical channel (thermalization of electrons and holes) in condensed matter studies. The extent of this X-ray energy conversion to optical photons depends on the nature of excitation channel (*K* or *L* shell etc.), and the nature of the material, e.g. crystallinity, morphology, size and proximity effects (surface and interface) [27].

Time resolved optical luminescence studies are an essential tool for the disentanglement of the various mechanisms involved in the creation and relaxation processes of electronic excitations [28]. Time-resolved (TR) XEOL can easily be conducted at third generation synchrotron sources due to their inherent ultra-stable pulsed time structure with up to sub-nanosecond pulse duration [28]; i.e. ESRF 75 ps root-mean-square (rms) pulse with either a 2.83 ns (multi-bunch mode) or 2.817 μs (single bunch mode) dark gap, APS 33.5 ps rms pulse with a 153 ns (in 24 bunch multi-bunch mode) dark gap, and CLS 35 ps rms pulse with a 570 ns (single bunch mode) dark gap [28,29]. A schematic drawing of a typical TR-XEOL experiment is shown in Figure 2-10. TR-XEOL measures the time dependence of the luminescence emission intensity (decay curve) following the excitation of core-level electrons after absorption of a synchrotron X-ray pulse. From the resultant decay curve it is possible to set a time window to measure the luminescence decay channel of interest. As mentioned in the preceding discussion band-gap luminescence decay in semiconductors is a fast (nanoseconds to sub-nanosecond) process which usually results in sharp excitonic emission bands with energy slightly below the band-gap (also known as near-band-gap, NBG, emission where the reduction in energy is due to the binding energy of the electron), whereas defect decay is a relatively slow process (hundreds of nanoseconds to microseconds) which gives rise to

broader lower energy luminescence emission bands. Therefore in a typical TR-XEOL measurement both short and long time windows (i.e., 0-5 and 5-150 ns) will be set to measure contributions of short- and long-lived states to various spectral features in the XEOL emission band. In a conventional TR-XEOL apparatus the optical luminescence is collected using an objective lens and then focused with a second lens onto the entrance slit of a monochromator.

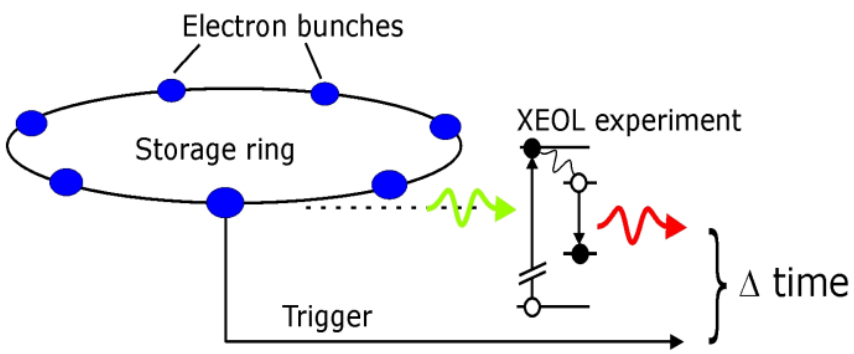

Figure 2-10 Schematic of a TR-XEOL experiment.

The monochromator is used to disperse the luminescence into individual wavelength components which are then detected with a fast photon-multiplier tube (PMT). The output signal from the PMT is then amplified and discriminated and used as a trigger for the “start” channel of a time-to-amplitude converter (TAC). A bunch clock signal, which measures the time structure of bunches in the storage ring, is used a “stop” signal for the TAC and then the output signal of the TAC is directed into a multi-channel analyzer (MCA) operating in a pulse-height analysis mode. The output of the MCA can then be used to produce a “counts vs. time” decay spectrum (Figure 2-11) which is equivalent to the luminescence decay curve. If this process is repeated for every optical emission wavelength it is possible to produce a TR-XEOL spectrum for the selected time window. This unfortunately makes collecting the full TR-XEOL spectrum a very beam-time expensive process.

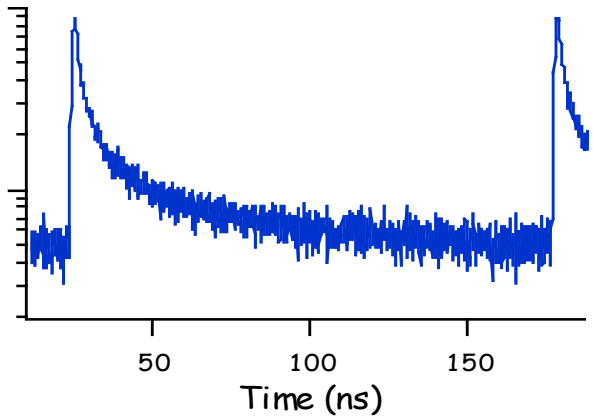

Figure 2-11 Counts vs. time decay curve of X-ray excited optical luminescence in a TR-XEOL experiment.

It is also possible to use an optical streak camera to take two-dimensional (2D) TR-XEOL measurements of luminescence decay lifetime vs. XEOL emission wavelength. Since these measurements record large segments of the TR-XEOL spectrum in each streak image it is possible to rapidly collect the full TR-XEOL spectrum using appropriate time windows to examine both fast and slow decay processes. The development and application of this technique is discussed in detail in chapter 6.

2.3 Synchrotron Facilities

2.3.1 Canadian Light Source (CLS)

The layout of the CLS is shown in Figure 2-12. The Canadian Light Source (CLS) is a third-generation synchrotron radiation source located at the University of Saskatchewan, Saskatoon, Canada. The CLS storage ring has twelve straight sections (nine of which are available for insertion devices), twenty four bending magnets, and can accommodate forty beam-lines when fully developed. There are currently fourteen beam-lines in operation providing photons in the Far IR to hard X-ray energy range. The CLS storage ring operates at 2.9 GeV and 250 mA. The storage ring has a circumference of 171 m and the beam has an emittance of 18.2 nm·rad. The superconducting RF cavity operates at 500 MHz [30].

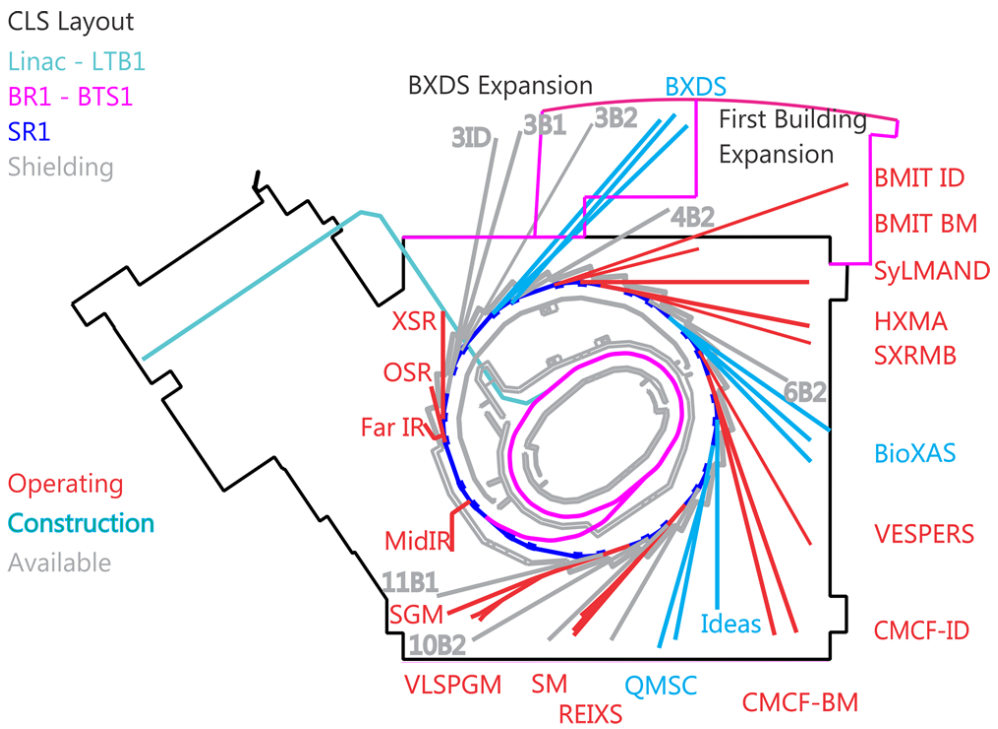

Figure 2-12 Layout of the Canadian Light Source [31].

2.3.2 Advanced Photon Source (APS)

The layout of the Advanced Photon Source (APS) is shown in Figure 2-13. The APS is a third-generation synchrotron light source located at Argonne National Laboratory, Argonne Illinois, USA. The storage ring has a circumference of 1104 m, operates at 7 GeV, and is run in a “top-up” mode with injections every two minutes to maintain a constant ring current of 102 mA. The RF cavity has a radio frequency of 351.927 MHz and the ring has an electron bean emittance of 2.514 nm·rad [32]. The APS is divided into thirty four sectors with each sector housing one or more beam-lines.

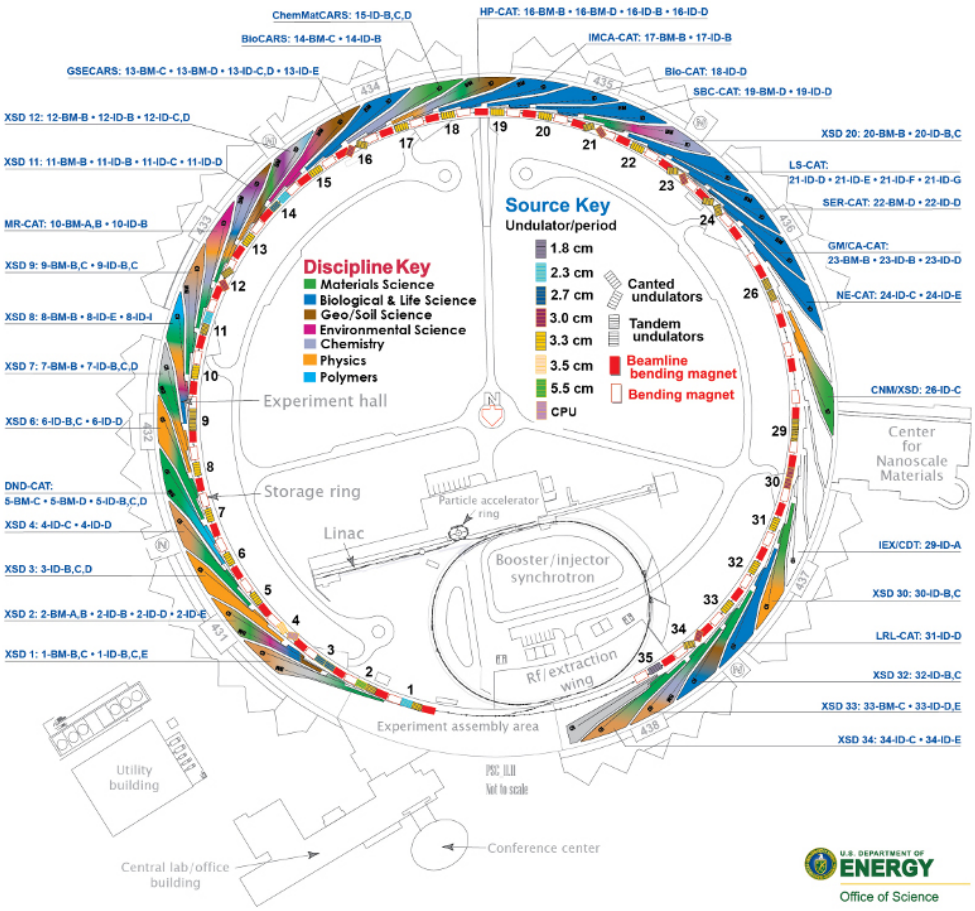

Figure 2-13 Layout of the Advanced Photon Source [33].

2.4 Beam-lines

2.4.1 Spherical Grating Monochromator (SGM) Beam-Line

The Spherical Grating Monochromator (SGM) beam-line, which is based on Chen's design [34], is a soft X-ray dragon-type beam-line (named for its characteristic dragon-like shape) at the CLS, the optical layout of which is shown in Figure 2-6 [35,36]. The instrumentation of this beam-line is described in detail elsewhere [36]. Briefly, photons are supplied to the SGM by a permanent magnet undulator with a period of 45 mm and a minimum gap of 12.5 mm. To allow for operation at higher photon energies two planar mirrors (Figure 2-14 M1 and M2) are employed to deflect the beam

horizontally, the beam then passes through a cylindrical focusing mirror (Figure 2-14 M3) where it is directed into the monochromator.

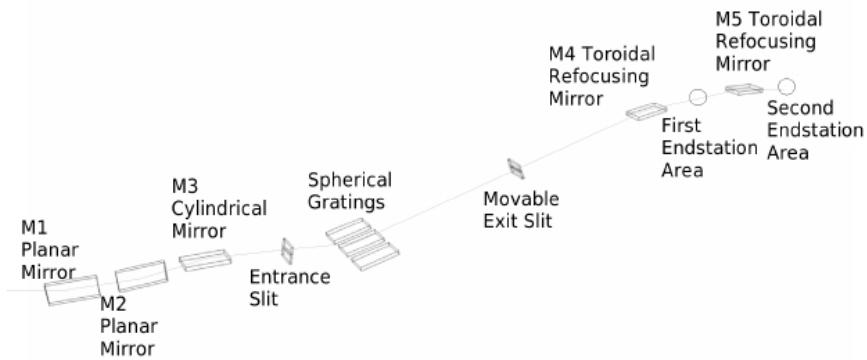

Figure 2-14 Optical layout of SGM beam-line at CLS [36].

The monochromator chamber contains three holographically etched spherical gratings with line spacings of 600, 1100, and 1700 lines/mm which are used to cover the photon energy range of 250–2000 eV with a resolving power (E/ΔE) greater than 10^4 at 800 eV and greater than 5000 at less than 1500 eV [35,36]. The SGM operates on the principle of grating diffraction

$$Nk\lambda = \sin\alpha + \sin\beta \tag{2-22}$$

where N is the grating density, which is equal to the number of lines per line-width (usually per mm), k is the diffraction order, λ is the photon wavelength, and α and β are the angles of incidence and refraction respectively. The X-ray photon energy is selected by rotation of the grating. A movable exit slit allows for the tracking of the vertical focal point of the spherical gratings. The beam is then focused at two in-line endstations through the use of torodial refocusing mirrors (Figure 2-14 M4 and M5). The SGM typically produces a spot size of 1 mm x 0.1 mm (H x V) and provides a flux of 4×10^{12} photons/s/0.1% BW at 250 eV and 1×10^{11} photons/s/0.1% BW at 1900 eV. The combination of excellent energy resolution, high flux, and wide energy range makes the SGM well suited for the study of $(Ga_{1-x}Zn_x)(N_{1-x}O_x)$ solid solutions since the N and O *K*-

edges and Zn and Ga $L_{3,2}$-edges are within the operating parameters of this beam-line. The SGM beam-line was used to collect N and O *K*-edge and Zn and Ga $L_{3,2}$-edge XANES and XEOL in chapters 3, 4, and 5. TR-XEOL streak camera measurements of $(Ga_{1-x}Zn_x)(N_{1-x}O_x)$ solid solutions at the N and O *K*-edge and Zn and Ga $L_{3,2}$-edges for chapter 6 were also performed at the SGM beam-line.

2.4.2 Pacific Northwest Consortium – X-ray Sciences Division (PNC/XSD) Beam-Line 20-BM

PNC/XSD beam-line 20BM at the APS is a double crystal monochromator (DCM) beam-line, the optical layout of which is shown in Figure 2-15.

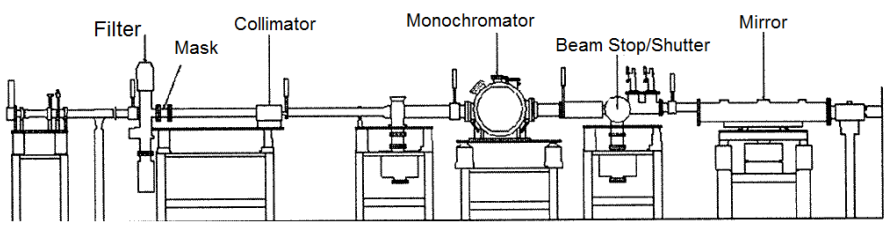

Figure 2-15 Optical layout of PNC/XSD beam-line 20-BM at APS [37].

Photons are supplied to 20-BM from a bending magnet and then passed into a Si (111) DCM which provides hard X-rays in the energy range of 2.7–32.7 keV [37]. Operation of the DCM is based on Bragg's law of diffraction

$$n\lambda = 2d\sin\theta \tag{2-22}$$

where λ is the photon wavelength, d is the lattice spacing of the crystal, and θ is the Bragg angle. The X-ray photon energy is selected by adjusting the angle of the incidence of the white beam from the bending magnet using the first crystal. The second crystal tracks the first crystal to maintain a fixed vertical exiting position for the X-ray photon beam. The energy resolution of 20-BM is 1.4×10^{-4} ($\Delta E/E$) with a flux of 1×10^{11} photons/s/0.1%BW and a spot size of 30 mm x 1 mm (H x V). Since 20-BM is a hard X-

ray beam-line it is well suited to study the *K*-edges of Zn and Ga in $(Ga_{1-x}Zn_x)(N_{1-x}O_x)$ solid solutions. Beam-line 20-BM was used to collect Zn, Ga, and In *K*-edge XANES and In *K*-edge EXAFS of in chapter 4 and Zn and Ga *K*-edge XANES and EXAFS in chapter 5. Preliminary testing of the streak camera TR-XEOL apparatus was also performed at 20-BM (chapter 6).

2.5 Detection Modes

There are three commonly used modes of detection for XAFS experiments, transmission, total electron yield (TEY), and fluorescence yield (FY) (Figure 2-16).

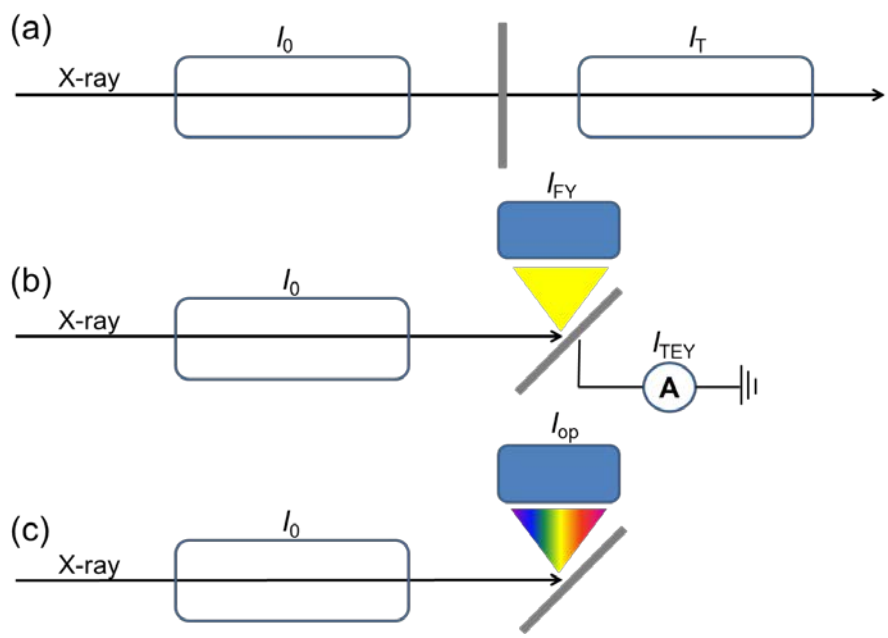

Figure 2-16 Detection modes for XAFS; (a) transmission, (b) fluorescence yield (FY) and total electron yield (TEY), and (c) photoluminescence yield (PLY).

A fourth less commonly used mode is photoluminescence yield (PLY). In a transmission measurement the intensity of the incident and transmitted X-rays are measured using ioinization chambers before and after the sample respectively (Figure 2-16 (a)). The modulation of the absorption coefficient as a function of excitation energy, $\mu(E)$ is then calculated directly from the ratio of I_0 to I_T using Beer's Law (see Equation 2-4). In a

TEY measurement the modulation of the absorption coefficient as a function of excitation energy, $\mu(E)$ is directly proportional to the yield of all electrons (photoelectrons, Auger electrons, and secondary electrons, see Equation 2-22 and the discussion that follows) escaping the samples surface. TEY is measured using the samples drain current, A (typically in picoamps) via a picoammeter (Figure 2-16(b)). In a FY measurement the modulation of the absorption coefficient as a function of excitation energy, $\mu(E)$ is directly proportional to the yield of all fluorescent X-rays escaping the sample. FY is commonly measured using either a multi-channel plate (MCP) detector or a multi-element solid state detector (Figure 2-16(b)). In a PLY measurement the modulation of the absorption coefficient as a function of excitation energy, $\mu(E)$ is directly proportional to the yield of all optical photons escaping the sample. In practice PLY is measured using either a PMT, a monochromator and PMT, or a spectrophotometer with a CCD detector (Figure 2-16(c)). The PLY can either be recorded as a total-yield or a partial-yield measurement if a monochromator or spectrophotometer is employed for wavelength selection. Finally a XEOL spectrum can be recorded by scanning the wavelength with a monochromator and PMT or collected instantaneously using a spectrophotometer with a CCD.

2.6 References

[1] H. Winick and S. Doniach, *Synchrotron Radiation Research* (Plenum Press, New York, 1980)

[2] Adapted from: http://internal.physics.uwa.edu.au/~hammond/SyncRes/making-synchrotron-light.htm

[3] J. Larmor, *Phil. Mag.*, **44**, 503 (1897)

[4] Adapted from: Intro to Synchrotron Radiation, D. Atwood 16th Jan 2007 http://ast.coe.berkeley.edu/srms/2007/Intro2007.pdf

[5] F. R. Elder, A. M. Gurewitsch, R. V. Langmuir, and H. C. Pollock, *Phys. Rev.*, **71**, 829 (1947)

[6] D. Ivanenko, and J. Pomeranchuk, *Phys. Rev.*, **65**, 343 (1944)

[7] D. H. Tomboulian, and P. L. Harman, *Phys. Rev.*, **102**, 1423 (1956)

[8] L. G. Parratt, *Rev. Sci. Instrum.*, **30**, 297 (1959).

[9] Used with permission of the copyright holder: Copyright © EPSIM 3D/JF Santarelli, Synchrotron Soleil

[10] T. Walker, *Introduction to Synchrotron Radiation*, Canadian Light Source

[11] T. K. Sham, Synchrotron Radiation: Earth, *Environmental and Materials Sciences Applications*, edited by G. S. Henderson, D. R. Baker, (Mineralogical Association of Canada, Saskatoon, 2002).

[12] Generated using data from the NIST table of mass attenuation coefficients for Pt: http://physics.nist.gov/PhysRefData/XrayMassCoef/ElemTab/z78.html

[13] Adapted from: M. Newville. *Fundamentals of XAFS*. http://www.xafs.org/tutorials/

[14] F. M. F. de Groot *Chem. Rev.*, **101**, 1779 (2001)

[15] F. M. F. de Groot, and A. Kotani, *Core-level spectroscopy of Solids* (CRC Press, Taylor & Francis Group, 2008)

[16] J. E. Müller, and J. W. Wilkins, *Phys. Rev. B*, **29**, 4331 (1984)

[17] J. J. Rehr, and J. C. Albers *Rev. Mod. Phys.*, **72**, 621 (2000)

[18] M. Newville. *Fundamentals of XAFS*. http://www.xafs.org/tutorials/

[19] M. O. Krause, J. H. Oliver, *J. Phys. Chem. Ref. Data*, **29**, 4331 (1984)

[20] T. K. Sham, and R. G. Carr, *J. Chem. Phys.*, **83**, 5914 (1985)

[21] W. C. Röntgen, *Nature* **53**, 274 (1896)

[22] T.K. Sham, D.T. Jiang, I. Coulthard, J.W. Lorimer, H.X. Feng, K.H. Tan, S.P. Frigo, R.A. Rosenberg, D.C. Houghton, and B. Bryskiewicz *Nature*, **363**, 331 (1993)

[23] R.A. Rosenberg, G.K. Shenoy, F. Heigl, S.-T. Lee, P.-S.G. Kim, X.-T. Zhou, and T.K. Sham, *Appl. Phys. Lett.*, **86**, 263115 (2005)

[24] L. Armelao, F. Heigl, S. Brunet, R. Sammynaiken, T. Reiger, R. I. Blyth, L. Zuin, R. Sankari, J. Vogt, and T. K. Sham, *ChemPhysChem*, **11**, 3625 (2010)

[25] L. Soderholm, G. K. Liu, M. R. Antonio, and F. W. Lyttle, *J. Chem. Phys.*, **109**, 6745 (1998)

[26] T.K. Sham, and R.A. Rosenberg, *ChemPhysChem*, **8**, 2557 (2007)

[27] R.A. Rosenberg, G.K. Shenoy, M.H. Chisholm, L.C. Tien, D. Norton, and S. Perton, *Nano. Lett.*, **7**, 1521 (2007)

[28] A. Rogalev, and J. Goulon, in *Chemical Applications of Synchrotron Radiation*, Part II: X-ray Applications; Sham, T.K., Ed.; World Scientific: River Edge, NJ, 2002; Vol 12B, pp 707-760.

[29] T.Z. Regier, J.M. Vogt, R. Sammynaiken, and T.K. Sham, AIP Conf. Proc. 1234, 838 (2010)

[30] http://www.lightsource.ca/operations/machinedesign.php

[31] Picture courtesy of Canadian Light Source Inc. http://www.lightsource.ca/experimental/images/ CLS_Experimental_Hall_2011.png

[32] The Advance Photon Source List of Parameters, compiled by H. M. Bizek, July 1996. http://www.aps.anl.gov/Science/Publications/techbulletins/content/files/ APS_1421579.pdf

[33] Picture courtesy of Advanced Photon Source. http://www.aps.anl.gov/Beamlines/Images/planview_11_3_11.jpg

[34] C. T. Chen, *Nucl. Instrum. Methods Phys. Res., Sect. A*, **256**, 595 (1987)

[35] T. Reiger, J. Krochak, T. K. Sham, Y. F. Hu, J. Thompson, and R. I. R. Blyth, *Nucl. Instrum. Methods Phys. Res., Sect. A*, **582**, 93 (2007)

[36] T. Reiger, J. Paulsen, G. Wright, I. Coulthard, K. Tan, T.K. Sham, and R. I. R. Blyth *AIP Conf. Proc.*, **879**, 473 (2007)

[37] S. M. Heald, D. L. Brewe, E. A. Stern, K. H. Kim, F. C. Brown,; D. T. Jiang, E. D. Crozier, and R. A. Gordon, J. Synchrotron Rad., **6**, 347 (1999)

Chapter 3

3 Soft X-ray XANES and XEOL Study of Indium Doped $Ga_{1-x}Zn_xN_{1-x}O_x$ Ultra-thin Nanosheets*

3.1 Introduction

Various GaN nanostructures, such as nanorods, nanotubes and nanobelts, are widely studied because of their potential applications in optoelectronic nanodevices [1-5]. ZnO is a well-known material similarly employed for light-emitting diodes and lasers, also in the form of various nanostructures, including nanosheets [6,7]. The band-gap of wurtzite GaN and ZnO is respectively 3.4 eV and ≈ 3.3 eV. Although GaN and ZnO absorb light well in the UV region, they are not satisfactory materials for overall solar energy applications due to their poor performance in the visible light range. Incorporating In into GaN to form $Ga_xIn_{1-x}N$ alloy shifts the material's band-gap energy to the visible-light region, and thus, improves their performance as photovoltaic cells [8]; nevertheless, the compound remains unsuitable for photochemical purposes, such as water splitting. In the past few years, Maeda and colleagues synthesized a solid-solution of $(Ga_{1-x}Zn_x)(N_{1-x}O_x)$ (GZNO) powders of submicrometer size via the nitration of a mixture of Ga_2O_3 and ZnO powders, or either $ZnGa_2O_4$ or ZnO, under NH_3 gas flow [9,10]. A solid solution forms because both GaN and ZnO can have wurtzite structures with similar lattice parameters. Solid solutions, with their highly efficient evolution of hydrogen gas, are promising as photocatalysts for water splitting [9]. Recently, Han et al. reported that in $(Ga_{1-x}Zn_x)(N_{1-x}O_x)$ nanocrystals and nanowires the type of chemical disorder of the solid solution greatly impacts their optical and electrical properties [11,12]. For example, the electron mobility of a $(Ga_{0.88}Zn_{0.12})(N_{0.88}O_{0.12})$ nanowire is about ~ 1 $cm^2/(V\ s)$ [12]. Since dimensionality is a parameter of the utmost importance in a material, changes in dimensionality may introduce dramatically different properties.

---

* Adapted with permission from *J. Phys. Chem. C* **115**, 3962 (2011). Copyright 2011 American Chemical Society

Monolayers and/or a few layers of other materials, such as graphene [13], BN [14], $NbSe_2$ [15], MoS_2 [15], and $Bi_2Sr_2CaCu_2O_x$ [15], have been previously prepared.

Dimensionality, size, morphology, and crystallinity have all been demonstrated to exhibit control on a material's physical and chemical properties; doping is another important factor for controlling these properties. Here, we describe our novel method of reacting a single Ga-In-Zn-O (GIZO) homogeneous precursor with ammonia to fabricate thin $(Ga_{1-x-y}In_yZn_x)(N_{1-x}O_x)$ (GIZNO) single-crystalline nanosheets. We discuss the results of our studies of their electronic and luminescence properties by X-ray absorption near edge structure (XANES) and X-ray excited optical luminescence (XEOL), respectively.

XANES refers to the modulation of the X-ray absorption coefficient in the near-edge region (>50 eV above the edge threshold) of a particular core level of an element in a material. By exciting the core electron of the element in a chemical environment to the previously unoccupied electronic states with a tunable synchrotron light source, one can probe the local symmetry and occupation of these states of which the characteristics are governed by the local chemistry. In the case of a $Ga_{1-x}Zn_xN_{1-x}O_x$ solid solution, the Ga/Zn $L_{3,2}$-edge probes electron transitions from Ga/Zn 2p to the conduction band of Ga/Zn 4d, 4s character (dipole selection rules), and N/O *K*-edge (1s) probes the 2p character of N/O in the conduction band. The absorption threshold (edge) and the spectral features (resonance) above the edge provide information about the unoccupied density of states. Thus XANES is a powerful tool to identify crystal phases/local chemical environment. Meanwhile, X-ray excited optical luminescence (XEOL), an X-ray photon-in, optical photon-out technique, is used to monitor the optical luminescence (UV–visible–near-IR) excited using a selected photon energy, which can excite a particular core level of a given element of interest to bound, quasi-bound, and continuum states, providing element and site specificity. The energy thus absorbed is in part transferred to optical de-excitation channels, resulting in optical luminescence. The extent of this X-ray energy conversion to optical photons depends on excitation channel and the nature of the material, e.g., crystallinity, morphology, size, and proximity effects (interface). XEOL can also be used to track XANES using photoluminescence yield (PLY), which is performed by monitoring the luminescence yield above and below an absorption edge. XANES and

XEOL can thus be used to reveal the element or the site that is responsible for the luminescence [16-18].

3.2 Experimental

3.2.1 Synthesis of indium doped $Ga_{1-x}Zn_xN_{1-x}O_x$ ultra-thin nanosheets

In the preparation of these materials, we dissolved a mixture of indium nitrate hydrate ($In(NO_3)_3.xH_2O$, 0.025 mol), gallium nitrate hydrate ($Ga(NO_3)_3)\cdot xH_2O$, 0.025mol), and zinc acetate dihydrate ($Zn(CH_3COO)_2\cdot 2H_2O$, 0.05 mol) in ethanolamine (MEA, $HOCH_2CH_2NH_2$, 4ml) and acetic acid (CH_3COOH, 0.2 ml) , stirred it at 65 °C for 2 h, and then left the GIZO solution to age for 1 week at 0 °C. Thereafter, we put the resulting GIZO gel-like precursor into an alumina boat and inserted the boat into the hot zone of a quartz tube furnace; then, the GIZO precursor was nitrated with ammonia at 850 °C for 10 h. We collected the final GIZNO product from the inner wall of the quartz tube close to the alumina boat.

3.2.2 Conventional Characterization

The sample thus obtained was explored by several techniques, viz., X-ray diffraction (XRD), high-resolution transmission electron microscopy (HRTEM), scanning electron microscopy (SEM), UV–vis diffuse reflectance spectroscopy, and energy-dispersive X-ray spectrometry (EDS). The sample's XRD patterns were recorded by a Rigaku/Miniflex-II spectrometer with Cu-Kα radiation. For the TEM observations, we dispersed an ethanol solution of the sample on a TEM copper grid covered with lacy carbon film. A JEOL-2100F microscope equipped with an EDS spectrometer and operated at 200 kV was used to detail the sample's shape, size, composition, and structure. We acquired SEM images on a Hitachi S-4800 with a field emission gun. Ultraviolet-visible diffuse reflectance spectra were collected on a Perkin-Elmer Lambda 950 UV/Vis/NIR spectrometer equipped with an integrating sphere, and converted from reflectance to the Kubelka-Munk function using a standard $BaSO_4$ plate as a reference.

3.2.3 Synchrotron Radiation Spectroscopy

Synchrotron radiation measurements were carried out at the undulator-based Spherical Grating Monochromator (SGM) beam-line of the Canadian Light Source (CLS) at the University of Saskatchewan. CLS is a 2.9 GeV third-generation source operating at 250 mA at injection. The detection modes used for the XANES measurements were total electron yield (TEY) recorded with the specimen's current and X-ray fluorescence yield (FY) recorded with a multichannel plate. We collected XEOL spectra using a dispersive optical spectrometer (Ocean Optics, QE65000) at selected excitation photon energies tuned across the relevant absorption edges (Ga and Zn $L_{3,2}$-edges, O and N K-edges, In M_2-edge). All spectra were normalized to the incident photon flux, measured with a refreshed Au mesh.

3.3 Results and Discussion

3.3.1 XRD, SEM, TEM, and UV-vis diffuse reflectance

Figure 3-1(a), shows the XRD pattern of the sample, which reveals a single-phase diffraction pattern indicative of a wurtzite structure similar to those of GaN and ZnO. The diffraction peaks are shifted to lower angles compared to those of GaN (Joint Committee on Powder Diffraction Standards (JCPDS) # 02-1078, $a = b$ =3.186 Å, c = 5.178 Å), but are higher than those of ZnO (JCPDS# 36-1451, $a = b$ = 3.250 Å, c = 5.206 Å).

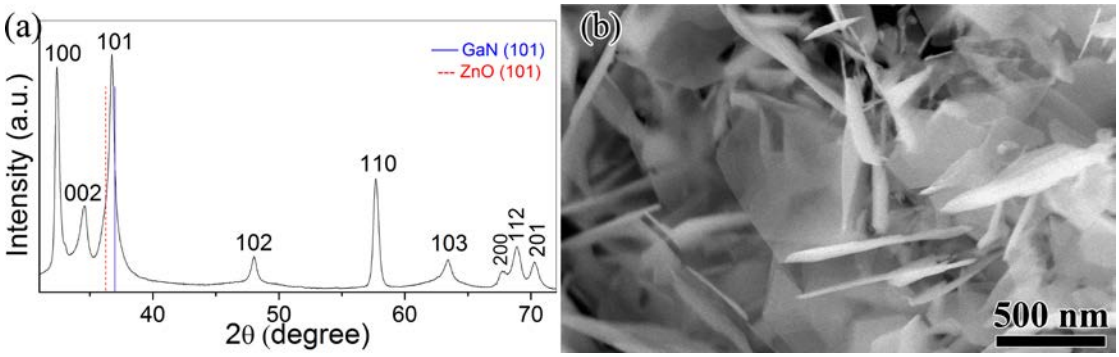

Figure 3-1 (a) XRD spectrum of the GIZNO nanosheets. (b) SEM image of the GIZNO nanosheets.

This finding denotes the formation of a solid solution, rather than a mixture of GaN and ZnO. Figure 3-1(b) is an SEM image showing that most regions of the sample are nanosheets, usually less than 10 nm thick; many are less than 5 nm. The widths of the nanosheets range from several hundred nanometers to several micrometers. They generally are flat with smooth edges, though some are rolled or folded.

Figure 3-2(a) is a low-magnification TEM image of a large nanosheet with a flat surface and smooth edges. Figure 3-2(b) is the corresponding electron diffraction pattern from a large area indexed to a single-crystalline hexagonal-wurtzite phase. The incident direction of the electron beam is along [001].

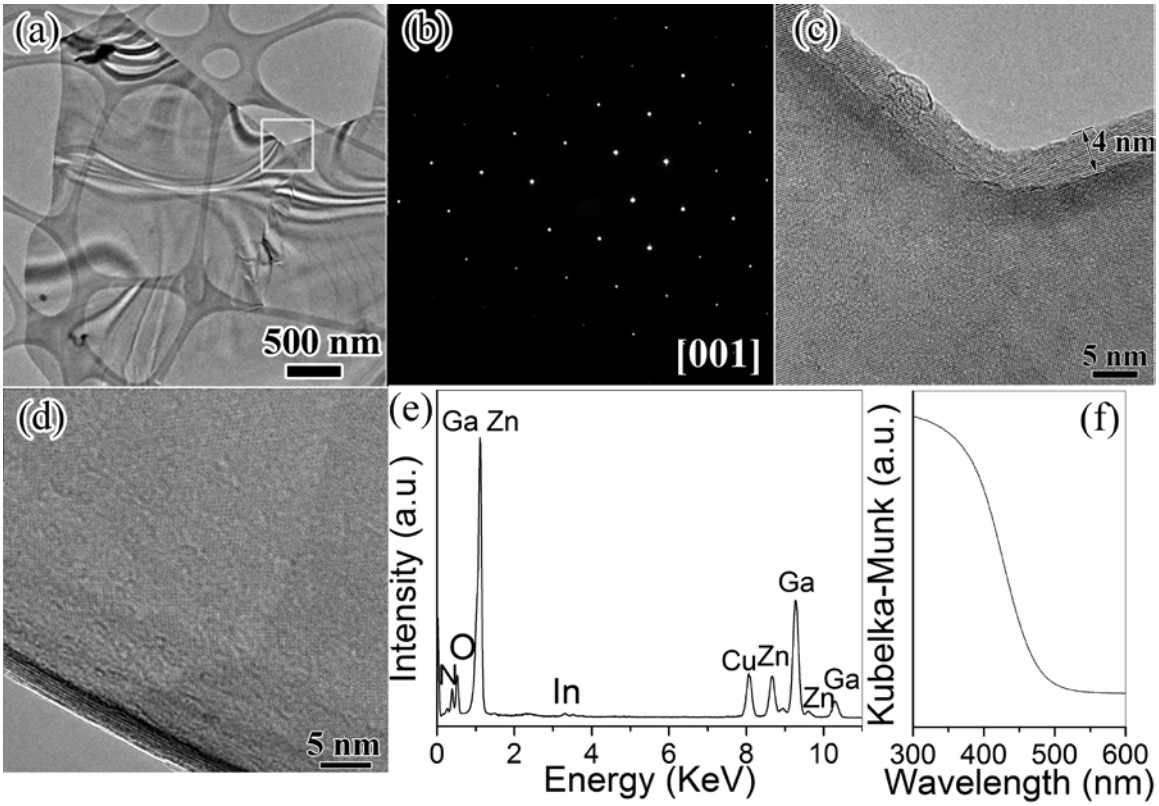

Figure 3-2 (a) Low-magnification TEM image of a large GIZNO nanosheet; (b) the corresponding electron-diffraction patterns from a large area indexed to a single-crystalline hexagonal-wurtzite phase; (c) high-magnification TEM image from the area enclosed by the square in Figure 3-2 (a); (d) high-magnification image of a nine-layered nanosheet, 2.3 nm thick; (e) EDS spectrum; (f) UV-vis diffuse reflectance spectrum.

Figure 3-2(c) shows a high-magnification TEM image from the area enclosed by the square in Figure 3-2(a). The edge of the nanosheet reveals 16 layers; its thickness is about 4.0 nm. The TEM images and the electron-diffraction patterns confirm that these nanosheets are single-crystal wurtzite structures. Figure 3-2(d) is a high-magnification image of a nine-layered nanosheet, 2.3 nm thick. Figure 3-2(e) is an typical EDS spectrum taken from a $(Ga_{0.756}In_{0.017}Zn_{0.227})(N_{0.773}O_{0.227})$ nanosheet. The atomic ratio of Zn/(Zn+Ga) of different nanosheets was relatively uniform, close to 0.23, with minor variations. The atomic ratio of indium (In/(Ga+In+Zn)) ranges from 1% to 2.1 %, i.e., much less than that (25 %) in the starting GIZO precursor. The Zn content (Zn/(Ga+In+Zn)) in the nanosheets was also lower than that (50%) in the GIZO precursor. This depletion of In and Zn in the final product suggests that most of their content in the starting GIZO precursor was volatilized by exposure to the reductive atmosphere during nitration, a finding that is consistent with the loss of Zn content in the final product of previously synthesized polycrystalline $(Ga_{1-x}\ Zn_x)(N_{1-x}O_x)$ powders [10]. Figure 3-2(f) shows the sample's UV-vis diffuse reflectance spectrum. The estimated value of the sample's band-gap energy is 2.55 eV, i.e., much narrower than that of either pure GaN or ZnO. Purportedly, N_{2p} – Zn_{3d} repulsion in the GaN-ZnO solid solution may elevate the valence band maximum to a higher potential energy as the top of the valence band is formed by N_{2p} atomic orbitals, resulting in a narrowing of the band gap vs. pure GaN [19].

For comparison, we followed a similar synthesis strategy to prepare an un-doped $Ga_{1-x}Zn_xN_{1-x}O_x$ solid solution reference standard. To prepare the Ga–Zn–O (GZO) precursor: We dissolved a mixture of gallium nitrate hydrate (0.05 mol) and zinc acetate dihydrate (0.05 mol) in MEA and, after stirring at 65 °C for 2 h, left the GZO solution to age for 1 week. Using the identical nitration process, we generated a $Ga_{1-x}Zn_xN_{1-x}O_x$ sample (GZNO). The XRD spectrum of the GZNO product exhibits a single-phase diffraction pattern indicative of the wurtzite structure, similar to those of GaN and ZnO (Figure 3-3(a)). SEM image shows that the GZNO sample is primarily nanoparticles, with sizes typically ranging from 40 to 120 nm (Figure 3-3(b)), along with some small pieces of nanosheets. From the EDS spectrum the stoichiometry of the material was determined to be $(GaN)_{0.76}(ZnO)_{0.24}$ (Figure 3-3(c)). The band-gap energy of the sample is

about 2.53 eV (Figure 3-3(d)), as measured from the UV-vis diffuse reflectance spectrum.

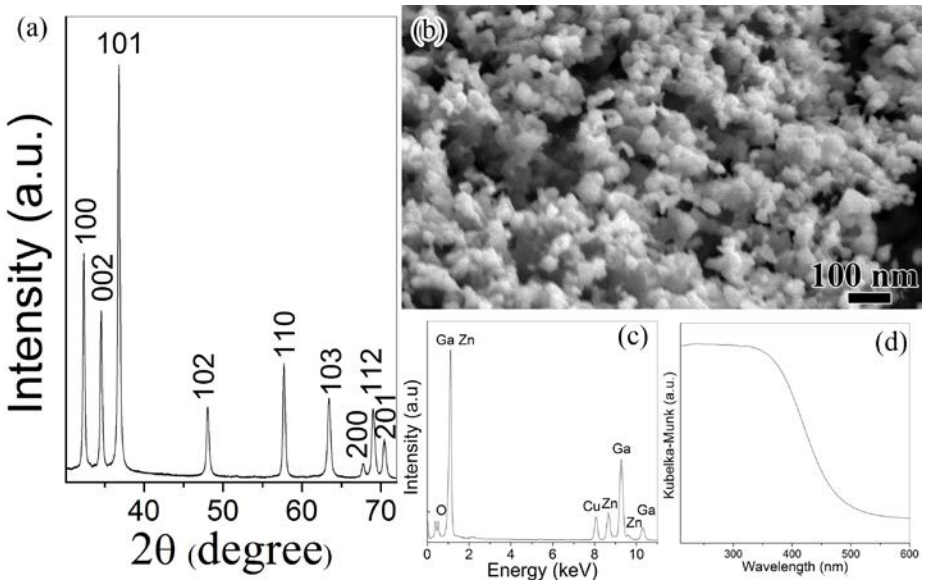

Figure 3-3 GZNO sample: (a) XRD spectrum; (b) SEM image; (c) EDS spectrum; (d) UV-vis diffuse reflectance spectrum.

In comparing both final samples with and without indium, GIZNO and GZNO, respectively, it is particularly interesting to note that their Zn/Ga atomic ratio is almost the same, even though the Zn/Ga atomic ratio in GIZO precursor doubles that in the GZO precursor. This finding suggests that reaction temperature and duration are crucial factors in determining the material's final composition. Under our experimental conditions, Zn^{2+} is easily reduced and vaporized. Although the incorporation of indium into GaN could shrink the band-gap [8], we found that the band-gap of the sample doped with In is slightly larger than that of the un-doped sample. However, the Zn concentration ratio of the doped sample is slightly higher than that in the un-doped sample, suggesting that the effect of zinc doping on band-gap narrowing is stronger than that of indium.

Undoubtedly, indium plays an important role in the formation of the 2D nanosheets, even though the indium concentration of the GIZNO product is much (~11–

25 times) lower than in the GIZO precursor. One possibility is that In offers an excessively supersaturated level of reactant vapor that apparently facilitates 2D nucleation and formation of 2D nanosheets in the vapor–solid (VS) process [20]. A remarkable feature in the XRD spectra of the GIZNO nanosheets is that the intensity ratio of (100), compared to the strongest peak (101), is much higher than that of GZNO nanoparticles (Figure 3-3(a)) and that (70%) of bulk GaN (JCPDS # 02-1078). The TEM and electron-diffraction patterns reveal that the preferred planes for the nanosheets are the low-index crystal planes, such as (100), (001) and (101), a very reasonable finding since a low-index crystal plane has lower surface energy, and thus offers a higher probability for 2D nucleation [20].

We propose here a possible self-catalyzed VS growth model of the 2D (oxy)nitride nanosheets: (1) Initially, the reduced In evaporates, forming an ultrathin In layer in a process analogous to Dai et al.'s self-catalyzed growth model for ZnO nanobelts [20]; (2) thereafter, O (from both the precursor and residual oxygen in the chamber), reduced Ga, Zn, In, and their partially reduced suboxides evaporate and dissolve into the melted In layer forming Ga–Zn–In–O, it is interesting to note that while Ga and In melt at slightly above room temperature, their vapor pressure is relative low compared to that of Zn; (3) the continuing dissolution of Ga, In, Zn, and O generates a supersaturated solution wherein the growth of GIZO nanosheets occurs via precipitation from the supersaturated liquid; and (4) these nanosheets are transformed into GIZNO during prolonged nitration. During the latter, the composition may continue to evolve producing the final GIZNO product. Thus, In acts as a catalyst and becomes one component of the sheets, resembling the role of Si during the formation of Si-doped B_4C nanorods [21]. Zn and Ga might also function as self-catalysts for growth of the 2D nanosheets, but they are much less efficient than In, at least under our experimental conditions.

3.3.2 XANES

Figure 3-4 shows the zinc and gallium $L_{3,2}$-edge TEY XANES from GZNO and GIZNO. We note that the FY spectra (not shown) exhibit similar features, demonstrating that the specimens are uniform and optically thin for these measurements. From Figure 3-

4 (a) and (b), we see that the zinc and gallium $L_{3,2}$-edge of GZNO, respectively appear to be very similar to each other and to that of gallium nitride, indicating that Zn is occupying a Ga site in a GaN-like lattice. To further verify this, the E_0 for the zinc L_3-edge of GZNO was shifted to line up with the gallium L_3-edge (see Figure 3-7(b), discussed below). One can clearly see that the first resonance features at the threshold are nearly identical. Since Ga^{3+} and Zn^{2+} are isoelectronic, they will exhibit very similar XANES if they are in the same chemical environment, e.g. Zn in a Ga site of GaN. When Ga^{3+} is replaced by Zn^{2+} charge neutrality must be preserved, this is affected by the substitution of O^{2-} for N^{3-} resulting in chemical disorder within the GaN lattice which is evident in the near-edge spectra. It should be noted that XANES is sensitive to local structures. The disorder comes about when the local environment is distorted upon alloying despite identical crystal structure. The distortion arises from (i) static disorder resulting from substitution in the first and second shell of the absorbing atom; e.g. substitution of O by N will not only change the inter-atomic distance between the absorbing atom and the backscatterer, but the back scattering amplitude as well and (ii) dynamic disorder due to the Debye-Waller term (the root mean inter-atomic displacement), which will also vary. Thus for an isoelectronic absorber with a similar ligand and the same crystal structure, the effect on the XANES is a small shift and broadening of all the resonances.

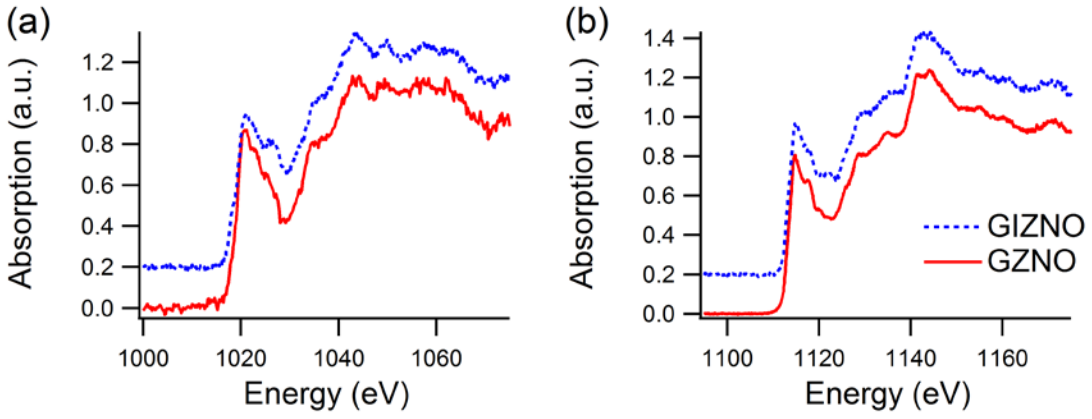

Figure 3-4 GZNO and GIZNO XANES at the (a) zinc and (b) gallium $L_{3,2}$-edges.

The oxygen *K*-edge (Figure 3-5(b)) XANES suggests that the local environment of oxygen is dissimilar to that of ZnO, but close to that of β-Ga_2O_3 [22]. The nitrogen *K*-edge (Fig. 3-5(a)) XANES of GZNO, which probes the partial density of states of N 2p character in the conduction band, is consistent with that exhibited by other gallium nitride nanostructures [23]. These observations are consistent with previous neutron diffraction results obtained by Yashima et al., which demonstrated that when these solid solutions are GaN rich, as is the case in our sample, the (Ga, Zn) cation coordinates with four (N,O) anions to form regular tetrahedrons in the GaN lattice [24].

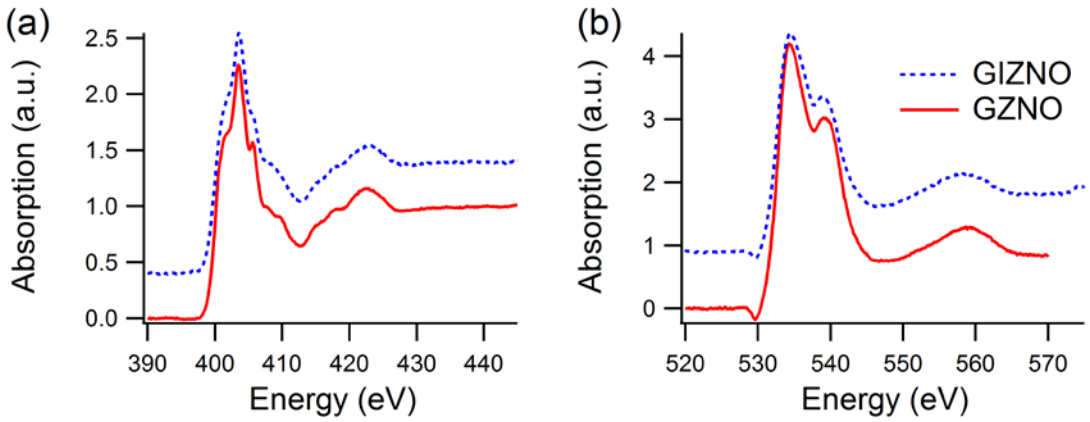

Figure 3-5 GZNO and GIZNO XANES at the (a) nitrogen and (b) oxygen *K*-edge.

We can explain what we observe in the XANES spectrum based on their analysis as follows: (1) The Ga and Zn $L_{3,2}$-edges involve dipole allowed electronic transitions from 2p→(4d,4s), and thus in a GaN rich environment we would expect both Zn and Ga cations to exhibit GaN like character in their absorption spectra; (2) the nitrogen *K*-edge involves transitions from N 1s→2p, since the sample is primarily GaN in composition we would expect that the nitrogen *K*-edge would be highly GaN like; (3) the oxygen *K*-edge probes the partial density of states of O 2p character via 1s→2p transitions, since there is

a much higher Ga concentration than Zn in the sample the local chemical environment of oxygen would be highly Ga-O like, which is significantly different from that of ZnO [22].

In the indium-doped GIZNO sample, we observed a small but noticeable broadening in all XANES features relative to the un-doped specimen, indicating that In doping increased chemical disorder within the lattice. This broadening is clearly observed in the nitrogen *K*-edge spectra of GIZNO in comparison to that of GZNO (Figure 3-5(a)). We further confirmed the presence of indium via the indium M_2-edge (Figure 3-6).

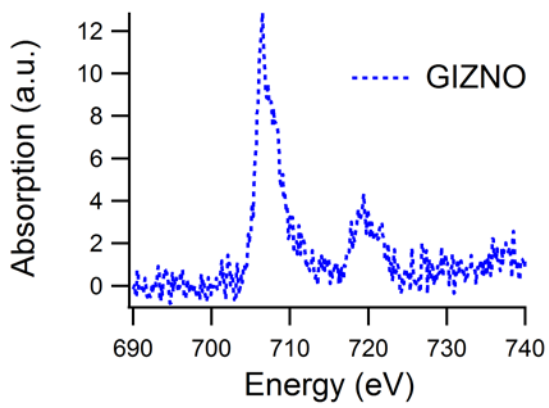

Figure 3-6 Indium M_2-edge XANES of GIZNO.

The oxygen *K*-edge for GIZNO also suggests an oxygen environment that is locally gallium oxide-like. Figure 3-7(a) and (b) show a comparison of the Zn and Ga $L_{3,2}$ edge XANES with (Figure 3-7(a)) and without (Figure 3-7(b)) In doping by aligning the threshold energy (E_0) of the Zn L_3-edge to that of the Ga L_3-edge. From the zinc $L_{3,2}$-edge it is clear that upon In doping there is an increase in ZnO character (Figure 3-7(a) vertical dashed line a”), this is clearly seen by comparing the Zn *L*-edge XANES in Figure 3-7(a) and (b); hence, zinc no longer appears to be solely occupying gallium sites (Figure 3-7(a) vertical dashed line a’), and some new ZnO-like features have emerged [25].Whereas for the un-doped sample, GZNO, we observe resonances in the near edge region (Figure 3-

7(b) vertical dashed lines a' and a") of the Zn $L_{3,2}$-edge that we can attribute to Zn occupying Ga sites in the GaN lattice.

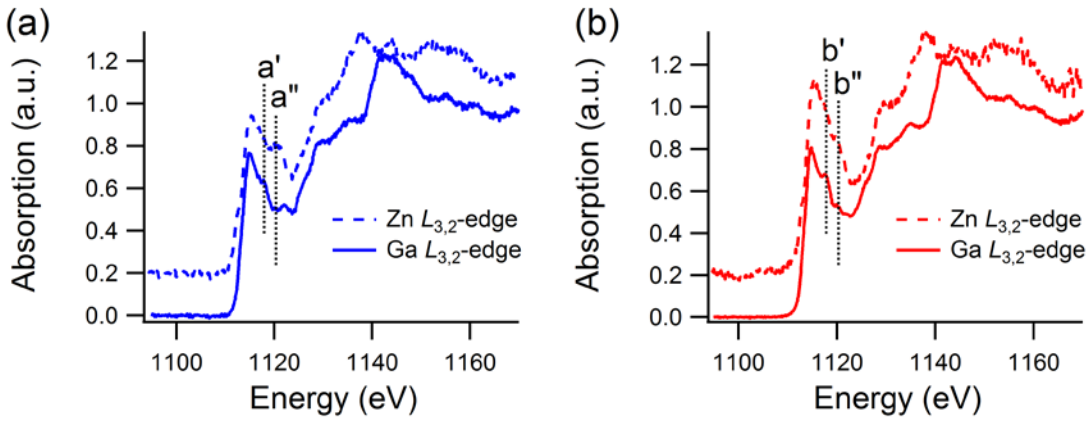

Figure 3-7 Zinc L_3-edge threshold energy (E_0) aligned to gallium L_3-edge (a) GIZNO; (b) GZNO.

3.3.3 XEOL

We measured the XEOL of the GZNO sample with excitation photon energy below and above the nitrogen and oxygen *K*-edges as well as the zinc and gallium $L_{3,2}$-edges (Figure 3-8(a) & (b)). The relative emission intensity rises with increasing excitation energy, with a λ_{max} at ~2.00 eV (~620 nm). The absence of near-band-gap emission is often associated with effective energy transfer to the defect optical channels. We observe equally spaced bumps in the XEOL of sample GZNO at ~60 meV (~484 cm^{-1}) which may correspond to phonon replicas (Figure 3-8(c)). There is no theoretical predication and/or experimental work on the phonon modes for this new class of oxy-nitride solid solutions, and thus further study is highly expected. It has previously been proposed that the Ga 4s and 4p orbitals dominate the composition of this material's conduction band, while the top of the valence band consists of N 2p, Zn 3d, and O 2p orbitals; furthermore, p–d repulsion seems to be responsible for narrowing of the band-gap compared with GaN [26]. Monemar et al. suggested that as zinc replaces gallium in GaN, acting as an acceptor impurity, four different acceptor levels are formed with binding energies of 0.4, 0.7, 1.0, and 1.4 eV [27,28]. Hirai et al. interpreted this as

resulting, respectively, in four distinct PL bands at ~430, 480, 560, and 690 nm , and that with the increase in *x* (where *x* is the ZnO concentration in the solid solution), the PL would be red-shifted [29].

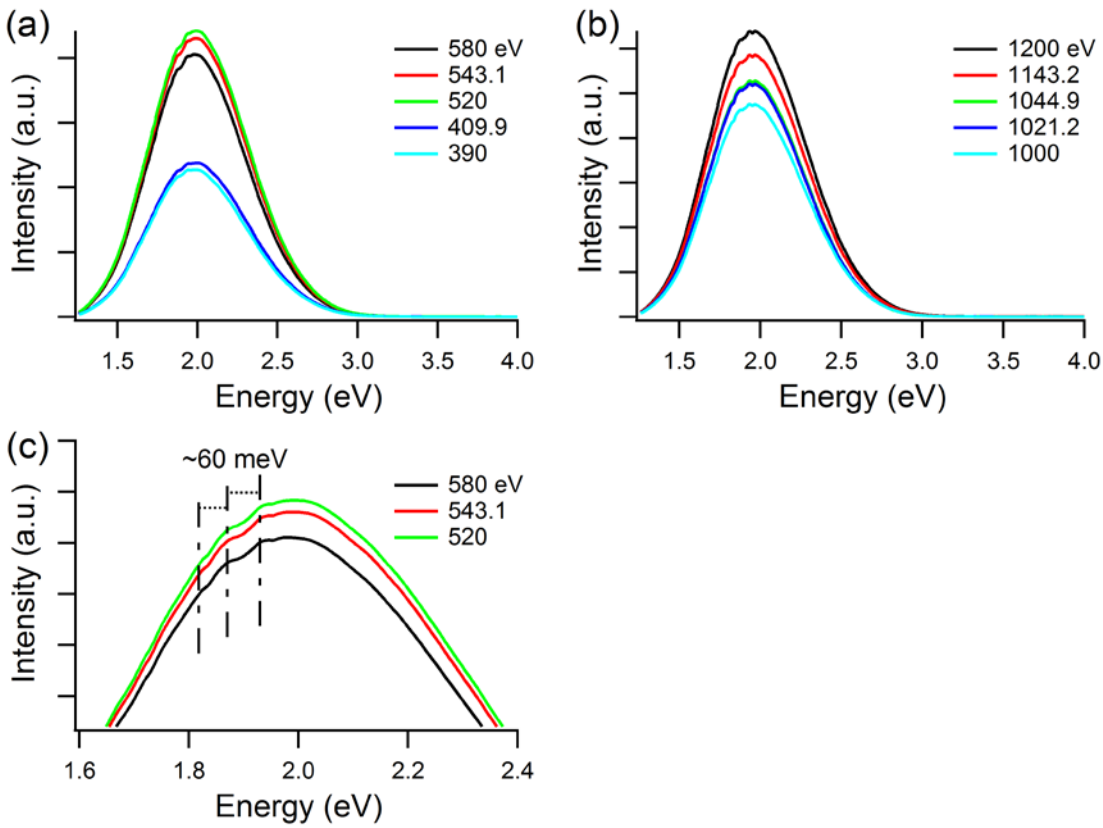

Figure 3-8 XEOL of GZNO: (a) across the nitrogen and oxygen *K*-edges; (b) across the zinc and gallium $L_{3,2}$-edges; (c) fine structure.

A broad (FWHM ~0.70 eV) XEOL emission band at ~2.00 eV (620 nm) was observed for GZNO, which is within the range of previous optically excited PL emission observed for these materials [24,29,30]. DFT studies of these solid solutions have suggested that the substitution of Zn for Ga causes the formation of acceptor levels above the valence band and the substitution of oxygen for nitrogen creates a donor level below the conduction band [30,31]. Recently Domen et. al. have thoroughly investigated the optically excited PL response of GaN rich $(Ga_{1-x}Zn_x)(N_{1-x}O_x)$ solid solutions and have made several important observations: (1) the luminescence of this material is likely to occur via the O donor level at the bottom of the conduction band; (2) two local maxima

were observed in the visible region and assigned to transitions from oxygen donors to a deep Ga vacancy band, the band at 480 nm is presumably related to the Zn acceptor levels and becomes slightly red-shifted with increasing Zn concentration; (3) the lower energy decay channel is favored at higher excitation energies; (4) and that the PL band at 480 nm was sensitive to, and increased with, an increase in excitation intensity [30].

Based on these observations we tentatively assign the broad XEOL band we observe for GZNO at ~2.00 eV to the transition of electrons bound to O donors recombining with holes bound to Zn acceptors in a donor-acceptor pair type recombination using the following argument: (1) at the energies of our XEOL measurements (390 – 1200 eV $>>E_{gap}$) we are exciting electrons from core levels to bound and quasi-bound states (and the continuum) of either some or all elements of the solid solution and therefore all de-excitation channels (fluorescence, photoluminescence, and Auger), including secondary processes are accessible; (2) the light generated by the third generation synchrotron source (CLS) in conjunction with the undulator insertion device of the SGM beam-line is both highly intense and highly collimated and thus levels with a low density of states (i.e. the Ga vacancy levels) will become saturated; (3) there is a very high density of Zn acceptor (and O donor) states in our sample thus our assignment of the XEOL emission band seems to be a plausible explanation. We aim to address the origin of the X-ray excited PL in a more quantitative fashion in future work.

We measured the XEOL of a sample of GIZNO below and above the nitrogen and oxygen *K*-edges, the indium $M_{3,2}$-edge, and the zinc and gallium $L_{3,2}$-edges (Figure 3-9(a), (b), and (c) respectively). The relative intensity of emission increases with increasing photon energy across the N and O *K*-edges. In contrast, across the Zn and Ga $L_{3,2}$-edges it decreases with increasing photon energy. This difference in intensity is associated with a change in quantum efficiency and sampling depth when the *core-hole* is turned on. Across the In $M_{3,2}$-edge emission intensity remained almost constant. However, emission increased with increasing photon energy in the un-doped sample across all absorption edges. Since these energies, the Zn and Ga $L_{3,2}$-edges, are above the In *M*-edges, our observation suggests that the energy absorbed by indium does not contribute significantly to the optical-decay channel; rather, its presence reduces the

penetration depth of the incident photons, thus lowering quantum efficiency compared to the un-doped sample.

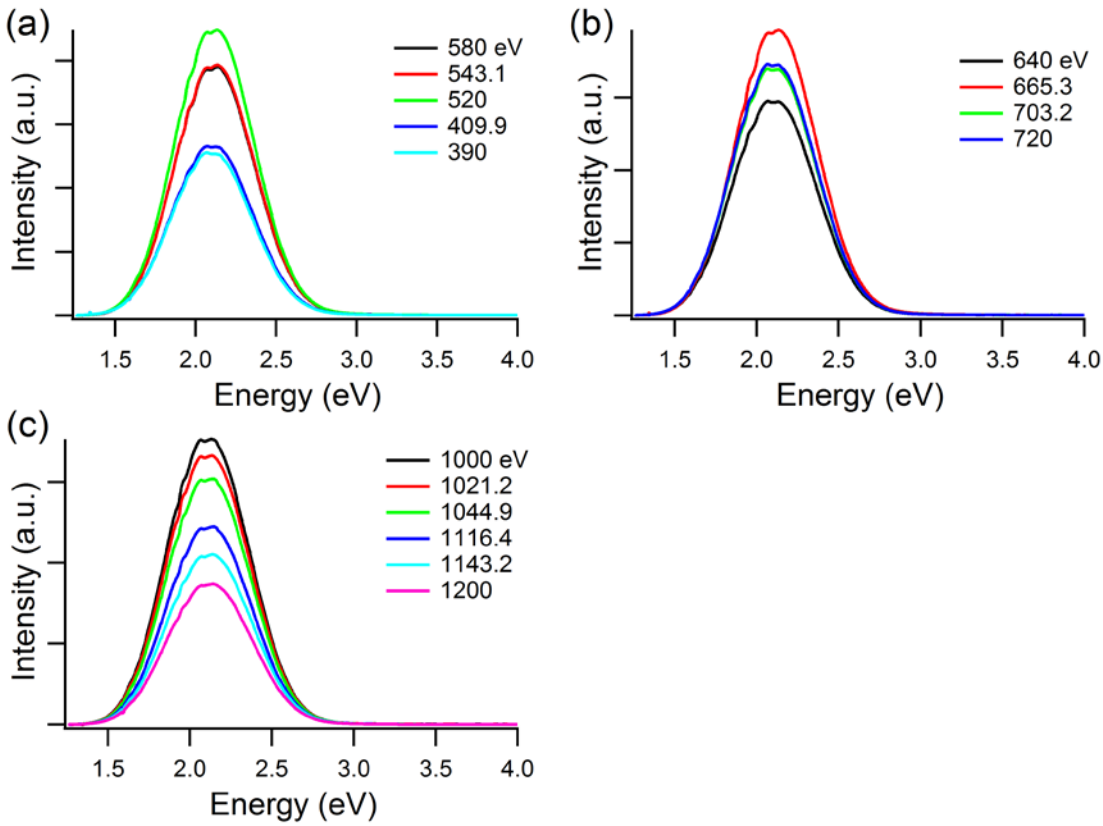

Figure 3-9 XEOL of GIZNO: (a) across the nitrogen and oxygen *K*-edges; (b) across the indium $M_{3,2}$-edges; (c) across the zinc and gallium $L_{3,2}$-edges.

Indium doping also entails a blue shift of the emission maximum to ~2.12 eV (584 nm) for the GIZNO sample, viz., an increase of ~0.12 eV over that of the GZNO material, and a narrowing of the emission band (FWHM ~0.57 eV). We might explain this as reflecting the In doping such that there is a narrower distribution of Zn acceptor levels above the conduction band and O donor levels below the valence band resulting in both a blue shift and narrowing of the emission band.

An alternative explanation for the differences observed in XEOL emission from GIZNO vs. GZNO may be the formation of an extremely thin (i.e. sub-nm) layer of indium oxide on the surface of the nanosheets. If this was the case then the XEOL

emission observed from GIZNO might be from energy transfer to defect decay channels in an InO_x surface sub-oxide layer, and not from the bulk region of the nanosheets. Additional evidence for this can be found by carefully examining the oxygen *K*-edge XANES, if we re-plot the spectra on the same vertical scale (Figure 3-10) we can see a decrease in intensity of the near-edge features in GIZNO vs. GZNO.

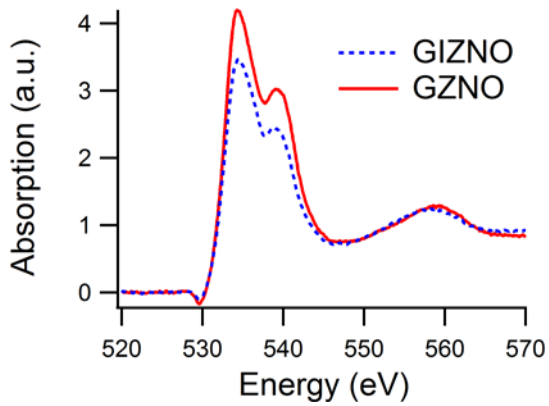

Figure 3-10 Oxygen *K*-edge XANES of GZNO and GIZNO.

If a small amount of oxygen was in an indium oxide absorber environment this might explain the decrease in the intensity of the near-edge absorption features of the oxygen *K*-edge XANES. Whereas the nitrogen *K*-edge has nearly identical intensity of all near-edge features in both GIZNO and GZNO (Figure 3-5(a)), the In doped and un-doped samples respectively, but GIZNO exhibits distortion of all near edge features. Since TEY is surface sensitive the distortion observed in the near-edge region of the nitrogen *K*-edge XANES of GIZNO is also consistent with the formation of a thin indium surface sub-oxide layer. This explanation is also consistent with our proposed growth model for the nanosheets where initially the reduced In evaporates forming an ultrathin In-layer which then acts as a growth catalyst for the nanosheet. This hypothesis will be addressed in more detail in chapter 4.

3.4 Conclusions

The band-gap energy of the indium doped nanosheets (GIZNO) was determined to be about 2.55 eV vs. 2.53 eV for the un-doped reference sample (GZNO). Although In plays a crucial role in the formation of the nanosheets it does not appear to have any

measureable effect on band-gap narrowing observed in this material. The slight increase observed in the band-gap of GIZNO vs. GZNO appears to be due to the reduction of the zinc content and not the introduction of In into the $Ga_{1-x}Zn_xN_{1-x}O_x$ alloy. XANES spectra measured at the zinc and gallium $L_{3,2}$-edges and the nitrogen and oxygen *K*-edges revealed that In-doping appears to increase chemical disorder in the system, broadening all absorption edges of the solid solution and potentially causes some phase separation in the solid-solution. The XEOL emission band observed from the indium doped nanosheets was found to be blue-shifted and narrowed vs. the un-doped sample. Although it is possible that the In doping causes a narrower distribution of Zn acceptor levels above the conduction band and O donor levels below the valence band explaining the resultant blue shift and narrowing of the XEOL emission band observed in GIZNO vs. GZNO, it is also possible that this is due to the formation of an extremely thin indium sub-oxide surface layer on the nanosheets. This will be addressed in a more quantitative fashion in future work.

3.5 References

[1] W. Q. Han, S. S. Fan, Q. Q. Li, and Y. D. Hu, *Science*, **277**, 1287 (1997)

[2] X. F. Duan, and C. M. Lieber, *J. Am. Chem. Soc.*, **122**, 188 (2000)

[3] S. Y. Bae, H. W. Seo, J. Park, H. Yang, J. C. Park, and S. Y. Lee, *Appl. Phys. Lett.*, **81**, 126 (2002)

[4] W. Q. Han, and A. Zettl, *Adv. Mater.*, 14, 1560 (2002)

[5] J. Goldberger, R. R. He, Y. F. Zhang, S. W. Lee, H. Q. Yan, H. J. Choi, and P. D. Yang, *Nature*, **422**, 599 (2003)

[6] Z. W. Pan, Z. R. Dai, and Z. L. Wang, *Science*, **291**, 1947 (2001)

[7] M. H. Huang, S. Mao, H. Feick, H. Q. Yan,; Y. Y. Wu, H. Kind, E. Weber, R. Russo, and P. D. Yang, *Science*, **292**, 1897 (2001)

[8] J. Wu, W. Walukiewicz, K. M. Yu, J. W. Ager, E. E. Haller, H. Lu, and W. J. Schaff, *Appl. Phys. Lett*., **80**, 4741 (2002)

[9] K. Maeda, K. Teramura, D. Lu, T. Takata, N. Saito, Y. Inoue, and K. Domen, *Nature*, **440**, 295 (2006)

[10] K. Maeda, and K. Domen, *J. Phys. Chem. C*, **111**, 7851 (2007)

[11] W. Han, Z. Liu, and H. Yu, *Appl. Phys. Lett.*, **96**, 183112 (2010)

[12] W.Q. Han, Y. Zhang, C.Y. Nam, C.T. Black, and E.E. Mendez, *Appl. Phys. Lett.*, **97**, 083108 (2010)

[13] K. S. Novoselov, A. K. Geim, S. V. Morozov,; D. Jiang, Y. Zhang,; V. Dubonos, I. V. Grigorieva, and A. A. Firsov, *Science*, **306**, 666 (2004)

[14] W. Q. Han, L. J. Wu, Y. M. Zhu, K. Watanabe, and T. Taniguchi, *Appl. Phys. Lett.*, **93**, 223103 (2008)

[15] K. S. Novoselov, D. Jiang, F. Schedin, T. J. Booth, V. V. Khotkevich, S. V. Morozov, and A. K. Geim, *Proc. Natl. Acad. Sci. U.S.A.*, **102**, 10451 (2005)

[16] L. Armelao, G. Bottaro, S. Quici, C. Scalera, M. Cavazzini, G. Accorsi, and M. Bolognesi, *ChemPhysChem*, **11**, 2499 (2010)

[17] W. Q. Han, D. Su, M. Murphy, M. Ward, T. K. Sham, L. J. Wu, Y. M. Zhu, Y. F. Hu, T. Aoki, *J. Mater. Res.*, **25**, 711 (2010)

[18] X. H. Sun, S. Lam, T. K. Sham, F. Heigl, A. Jurgensen, and N. B. Wong, *J. Phys. Chem.* B, **109**, 3120 (2005)

[19] S. H.Wei, and A. Zunger, *Phys. Rev. B*, **37**, 8958 (1988)

[20] Z. R. Dai, Z. W. Pan, and Z. L. Wang, *Adv. Funct. Mater.*, **13**, 9 (2003)

[21] W. Q. Han, *Appl. Phys. Lett.*, **88**, 133118 (2006)

[22] X. T. Zhou, F. Heigl, J. Y. P. Ko, M. W. Murphy, J. G. Zhou, T. Regier, R. I. R. Blyth, and T. K. Sham, *Phys. Rev. B*, **75**, 125303 (2007)

[23] T. Kuykendall, P. J. Pauzauskie, Y. F. Zhang, J. Goldberger, D. Sirbuly, J. Denlinger, and P. D. Yang, *Nature Mater.*, **3**, 524 (2004)

[24] M. Yashima, K. Maeda, K. Teramura, T. Takata, and K. Domen, *Chem. Phys. Lett.*, **416**, 225 (2005)

[25] M. W. Murphy, X. T. Zhou, J. Y. P. Ko, J. G. Zhou, F. Heigl, and T. K. Sham, *J. Chem. Phys.*, 130 (2009)

[26] K. Maeda, K. Teramura, T. Takata, M. Hara, N. Saito, K. Toda, Y. Inoue, H. Kobayashi, and K. Domen, *J. Phys. Chem.* B, **109**, 20504 (2005)

[27] B. Monemar, H. P. Gislason, and O. Lagerstedt, *J. Appl. Phys.*, **51**, 640 (1980)

[28] B. Monemar, O. Lagerstedt, and H. P. Gislason, *J. Appl. Phys.*, **51**, 625 (1980)

[29] T. Hirai, K. Maeda, M. Yoshida, J. Kubota, S. Ikeda, M. Matsumura, and K. Domen, *J. Phys. Chem.* C, **111**, 18853 (2007)

[30] M. Yoshida, T. Hirai, K. Maeda, N. Saito, J. Kubota, H. Kobayashi, Y. Inoue, and K. Domen, *J. Phys. Chem.* C, **114**, 15510 (2010)

[31] W. Wei, Y Dai, K Yang, M. Guo, B. Huang *J. Phys Chem. C*, **112**, 15915 (2008)

Chapter 4

4 2D XAFS–XEOL Mapping of $Ga_{1-x}Zn_xN_{1-x}O_x$ Nanostructured Solid Solutions*

4.1 Introduction

Since the first report by Maeda et al. of solid solutions of GaN and ZnO ($Ga_{1-x}Zn_xN_{1-x}O_x$) as potential photocatalysts for the overall splitting of water into hydrogen and oxygen, a highly coveted process for hydrogen production, there has been an intense research focus on these unique oxynitride materials [1-3]. Although both GaN and ZnO have band-gap energies greater than 3 eV, it has been found that GaN-ZnO solid solutions have band-gap energies less than 3eV and that the band-gap narrows with an increase in *x* (or ZnO concentration), falling in the range of ~2.4–2.8 eV (516–442 nm in optical emission) for $x = 0.05–0.42$ [4,5]. This band-gap narrowing has been attributed to p–d repulsion between N 2p and Zn 3d orbitals in the valence band resulting in an upward shift of the valence band maximum, and a corresponding narrowing of the band-gap [6]. Recent UV-vis diffuse reflectance and photoluminescence excitation (PLE) studies have suggested that the intrinsic band-gap of GaN-ZnO solid solutions can be attributed to the GaN component whereas visible light absorption can be assigned to Zn-related acceptor bands [7]. These materials also exhibit unique visible luminescence properties that give rise to broad photoluminescence peaks in the 500–700 nm range that exhibit a red-shift of the emission maximum corresponding to an increase in *x* and have been attributed to Zn acceptor levels, O donor levels, and Ga vacancies [4-7]. However the assignment of the origins of the visible luminescence is tentative, and more work in this area is necessary to complement the understanding of the electronic structure of these complex materials.

---

*Adapted with permission from *J. Phys. Chem. C* **115**, 20507 (2011). Copyright 2011 American Chemical Society

The recent synthesis of GaN-ZnO (GZNO) solid solution nanocrystals by Han et al., which are hypothesized to have better quantum-conversion efficiency than the bulk, has demonstrated that nanostructures of these materials follow the same trends in band-gap narrowing as the bulk [8,9]. The narrowest band-gap reaches 2.21 eV for the $(GaN)_{0.52}(ZnO)_{0.48}$ nanocrystals. These GZNO nanostructures exhibit a visible PL response consistent with bulk solid solutions of GaN-ZnO, and thus, it is hypothesized that the origin of the PL is the same as in the bulk. To extend light absorption of these photocatalysts farther into the visible part of the spectrum, solid solutions of GaN-ZnO-InN were synthesized, and the predicted extension of the absorption edge farther into the visible spectrum was indeed observed [10].

We have recently synthesized solid solution $Ga_{1-x}Zn_xN_{1-x}O_x$ nanoparticles (GZNO, Fig. 4-1(a)) and ultrathin $(Ga_{1-x-y}In_yZn_x)(N_{1-x}O_x)$ (In doping ratio is ≈ 1.5%) nanosheets (GIZNO, Fig. 4-1(b)) and studied their physical properties using a combination of conventional techniques and synchrotron-based spectroscopy including XANES (X-ray absorption near edge structures) and XEOL (X-ray excited optical luminescence) [11].

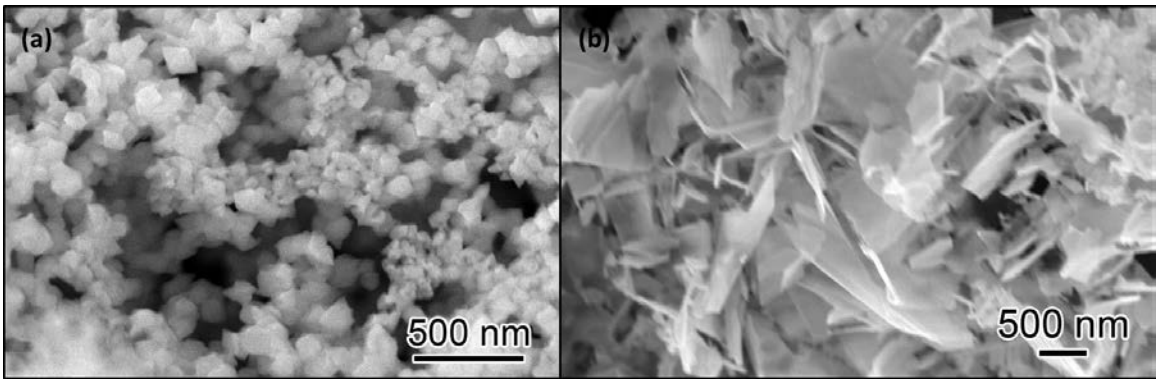

Figure 4-1 SEM of (a) GZNO nanoparticles and (b) GIZNO nanosheets.

The nanosheets were synthesized by the same method as the nanoparticles using a precursor doped with indium. Our preliminary findings indicated that although there was no significant effect on the band-gap (In doped $E_{gap} \approx 2.55$, un-doped $E_{gap} \approx 2.53$ eV) a broadening of all absorption edges, a blue-shift of the emission maximum from ca. 2.0

eV to 2.12 eV, and narrowing of the emission band were observed upon In doping [11]. To further our understanding of the nature of the observed X-ray excited optical luminescence (XEOL) and the effect of indium doping, which led to a dramatic change in the morphology from nanoparticles to nanosheets, we have applied a new synchrotron-based spectroscopy technique to this problem, namely, two-dimensional X-ray absorption fine structure–X-ray excited optical luminescence (2D XAFS–XEOL) spectroscopy in the soft X-ray region. We also studied these materials using X-ray absorption near edge structures (XANES) spectroscopy at the indium, gallium, and zinc *K*-edges in the hope of both resolving the local chemical environment of the indium dopant and determining the role of In in the growth and luminescence properties. The effects of solid solution formation on the local Ga and Zn chemical environments were also studied. Herein, we report the results of these experiments.

XANES refers to the modulation of the X-ray absorption coefficient in the near-edge region (from the edge up to ~50 eV above the threshold) of a particular core level of an atom in a material. XANES is often referred to as the near-edge region of the X-ray absorption fine structure (XAFS) which includes both the near-edge region and the extended region, the extended X-ray absorption fine structure (EXAFS). By exciting the core electrons of an element in a chemical environment to previously unoccupied electronic states with a tunable synchrotron light source, one can probe the local symmetry and occupation of these states, whose characteristics are governed by the local chemistry. Meanwhile, X-ray excited optical luminescence (XEOL), an X-ray photon-in / optical photon-out technique, is used to monitor the optical luminescence (UV–NIR) excited using a selected X-ray photon energy that can excite a particular core level of a given element of interest to bound, quasi-bound, and continuum states, providing elemental and, in some cases, site specificity. The energy absorbed is, in part, transferred to optical de-excitation channels, resulting in optical luminescence. Thus, XEOL is different from conventional UV-visible photoluminescence in that it can be site specific under favourable conditions if the excitation energy is scanned across an absorption edge, as the core level is specific to a given element, and it involves energy transfer through secondary processes to the optical channel (thermalization of electrons and holes, which, in turn, recombine radiatively) in condensed-matter studies. The extent of this X-ray

energy conversion to optical photons depends on the nature of excitation channel (*K* or *L* shell, etc.); the sample thickness; and the nature of the material, including crystallinity, morphology, size and proximity effects (surface and interface). XEOL can also be used to track the XANES using photoluminescence yield (PLY), which is done by monitoring the luminescence yield across an absorption edge. XANES recorded in PLY is equivalent to the excitation spectrum in the UV–visible region. XANES and XEOL can thus be used to reveal the element or the site that is responsible for the luminescence [12-14]. When these two techniques are combined into 2D XAFS–XEOL spectroscopy, one has the ability to extract the photoluminescence yield (PLY) at any optical wavelength as a function of incident X-ray energy, producing wavelength-selected optical-XAFS spectra. From the same experiment, one can extract excitation-energy-selected XEOL spectra, which enables the same elemental specificity gained from XAFS to be applied the optical luminescence response of a given material. XEOL is especially powerful when soft X-ray excitation is used. This is partly because of the high absorption cross-section, which can lead to total absorption of the incident light, yielding good contrast in the optical yield below and above an absorption edge, and partly because of the considerably shortened thermalization track of the secondary process (compared to hard X-ray techniques), which contributes significantly to the X-ray-to-visible light conversion [15].

4.2 Experimental

4.2.1 Synthesis

GZNO and GIZNO samples were synthesized as described previously [11]. Briefly a mixture of gallium nitrate hydrate, zinc acetate dihydrate (GZNO), and indium nitrate hydrate (GIZNO) was dissolved in monoethanolamine (MEA), stirred at 65 ℃ for 2 h, and aged for 1 week at 0 ℃. The resultant gel-like precursor was put in an alumina boat and inserted into the hot zone of a quartz tube furnace, where the precursor was nitridated with ammonia at 850 ℃ for 10 h. The product (GZNO nanoparticles or GIZNO nanosheets) was collected from the inner wall of the quartz tube close to the alumina boat.

4.2.2 2D XAFS–XEOL Spectroscopy

Two-dimensional XAFS–XEOL measurements were carried out at the undulator-based Spherical Grating Monochromator (SGM) beamline of the Canadian Light Source (CLS) at the University of Saskatchewan. CLS is a 2.9 GeV third-generation source operating at 250 mA at injection [16]. Powdered samples were applied in a thin uniform layer on carbon tape on a copper sample holder. The detection mode used for XANES measurements was total electron yield (TEY) recorded with the specimen's current. XEOL (UV–NIR, ~200–980 nm) spectra were collected using a dispersive optical spectrometer (Ocean Optics, QE65000) at every excitation photon energy of the TEY XANES scans across the N and O *K*-edges and Zn and Ga $L_{3,2}$-edges respectively for both samples (GZNO and GIZNO). A XEOL spectrum was also collected for every excitation photon energy of the TEY XANES scan across the In $M_{3,2}$-edges for sample GIZNO. Thus, a 2D XAFS–XEOL map can be created in which the *x* axis is the excitation energy and the *y* axis is the luminescence wavelength and the luminescence intensity as a function of excitation energy and emission wavelength is color-coded. More details of the technique will be discussed elsewhere. All spectra were normalized to the incident photon flux, measured with a refreshed Au mesh.

4.2.3 XANES and EXAFS Spectroscopy

Zinc, gallium, and indium *K*-edge XANES and indium *K*-edge EXAFS measurements were carried out at the bending magnet based PNC/XSD 20-BM beam-line of the Advanced Photon Source (APS) at Argonne National Laboratory, Argonne, IL. APS is a 7.0 GeV third-generation source operating in top-up mode at a ring current of 100 mA. Thin uniform samples were prepared on Kapton tape and the tape was folded to a thickness of ~1–2 absorption lengths ($1/\mu$, where μ is the absorption coefficient). The detection mode was fluorescence X-ray yield recorded using a 13-element Canberra detector. The sample was placed at 45^0 with respect to the incident photons, and the fluorescence detector was placed at 90^0 with respect to the incident photons, or normal detection geometry. The detector count rate was kept below 50000 counts to prevent detector saturation. All spectra were normalized to the dead-time-corrected I_0, measured

using an ion chamber filled with 100% N_2. Reference foil standards, used for energy calibration, were measured in transmission mode downstream of the sample between two ion chambers filled with an 85:20 sccm N_2/Ar mixture.

4.3 Results and Discussion

4.3.1 2D XAFS–XEOL of GZNO

Figure 4-2(a) and (c) display the 2D XAFS–XEOL map of GZNO in which, the color represents the intensity of the XEOL excited across the entire energy range, including the nitrogen and oxygen *K* and zinc and gallium $L_{3,2}$ absorption edges (see representative XEOL vertical cuts in Figure 4-3(a) and (b) below).

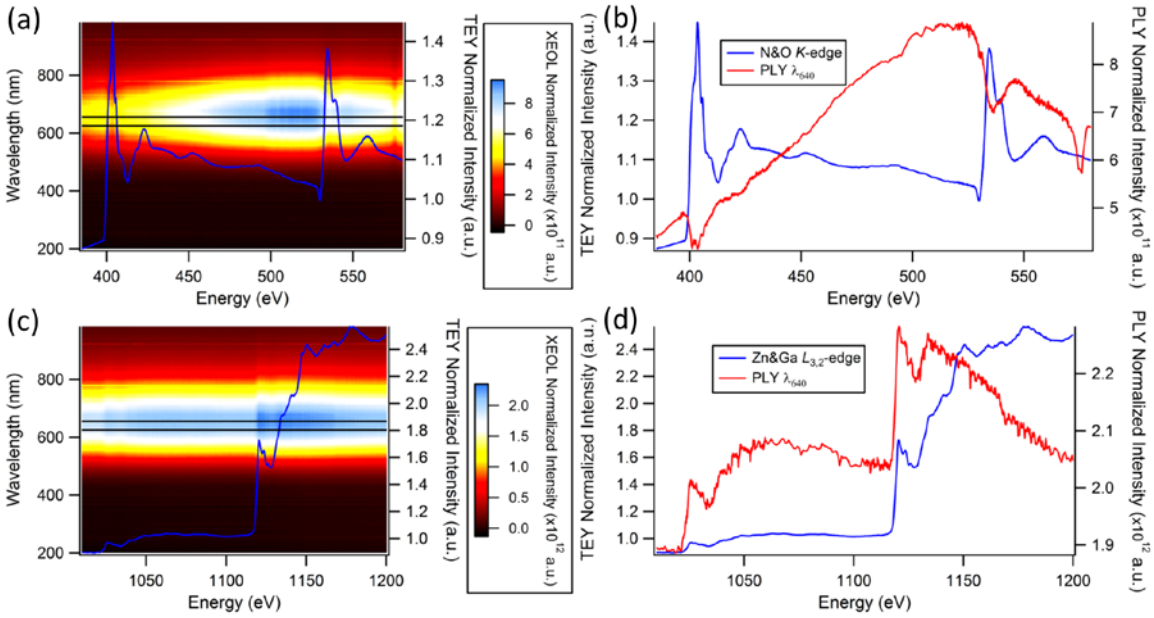

Figure 4-2 GZNO XAFS–XEOL: a) 2D XAFS-XEOL scan across N and O *K*-edges, TEY overlaid on scan (blue), black horizontal line denotes the window where optical-XAFS were collected. b) Wavelength window selected PLY (red) vs TEY across N and O *K*-edges. c) 2D XAFS-XEOL scan across Zn and Ga $L_{3,2}$-edge, TEY overlaid on scan (blue). d) Wavelength window selected PLY (red) vs TEY across Zn and Ga $L_{3,2}$-edges.

The XANES recorded in TEY are also shown, and they are representative of the GaN-ZnO alloy, as reported previously [11]. Figure 4-2(b) and (d) represent the photoluminescence yield (PLY) for a selected horizontal cut (wavelength window). According to the 2D XAFS–XEOL map of GZNO (Figure 4-1(a)) and the corresponding PLY $\lambda_{640\ \mathrm{nm}}$ trace (Figure 4-2(b)), the PLY starting from below the N *K*-edge (380 eV) decreases at the N *K*-edge but intensifies gradually until well above the nitrogen *K*-edge and just below the oxygen *K*-edge, and the PLY exhibits a negative response across the N and O *K*-edges. The 2D XAFS–XEOL map of the Zn and Ga $L_{3,2}$-edges (Figure 4-2(c)) and the corresponding PLY trace (Figure 4-2(d)) show a steady increase in the XEOL, with a corresponding positive increase across both Zn $L_{3,2}$-edges and Ga L_3-edges, and a decrease above the Ga L_2-edge.

These behaviours can be explained in terms of the penetration depth of the excitation photons and the origin of the luminescence when the penetration depth of the soft X-ray is less than the thickness of the sample. Below the nitrogen *K*-edge, there is insufficient energy to excite core electrons and produce fluorescent X-rays or Auger electrons, and thus, optical luminescence is only a function of electron-hole (e–h) pair production following the excitation of N, O, Zn, and Ga shallow levels (valence and inner-valence photoelectrons and their thermalization in the solid) and subsequent radiative recombination [17-19]. Across the nitrogen and oxygen *K*-edges, the X-ray penetration depth [~90–160 nm, the same order of magnitude as the size (diameter) of GZNO nanoparticles, 40–120 nm] decreases abruptly at the edge threshold, and the optical luminescence intensity is very sensitive to this rapid increase in absorption cross section compared to excitation below the edge, with a resultant decrease in e–h pair production, which is due to the competition for photons by the newly accessible levels (N and O 1s excitation) and the decay of the *core-hole*. Because Auger electrons created in the surface and near-surface regions can escape the surface without contributing to the thermalization (secondary) process, nanostructures with dimensions comparable to the attenuation length of electrons can truncate the thermalization path leading to a reduction in e–h pair production.

An intense region of the luminescence channel appears well above the N *K*-edge but just below the O *K*-edge, where the creation of an N *core-hole* (1s) and the subsequent de-excitation cascade in the absorbing atom leads to the creation of more holes at the top of the valence band and electrons at the bottom of the conduction band (photoexcited and thermalized electrons) because of the increasing penetration depths and increasing kinetic energy of the photoelectrons [18,19]. Thus, as is commonly the case at soft X-ray energies (i.e., low X-ray energies, where the X-ray absorption cross section is large and, thus, the penetration depth is low), an inversion of the PLY across the N and O *K*-edges occurs, and after the edge, the intensity increases again gradually until the next edge [15,20-23]. It should be noted that the XEOL spectra shown in Figure 4-3 exhibit a single peak with a maximum at ~640 nm (~ 1.94 eV). This energy is too small and the width is too broad for the near-band-gap emission.

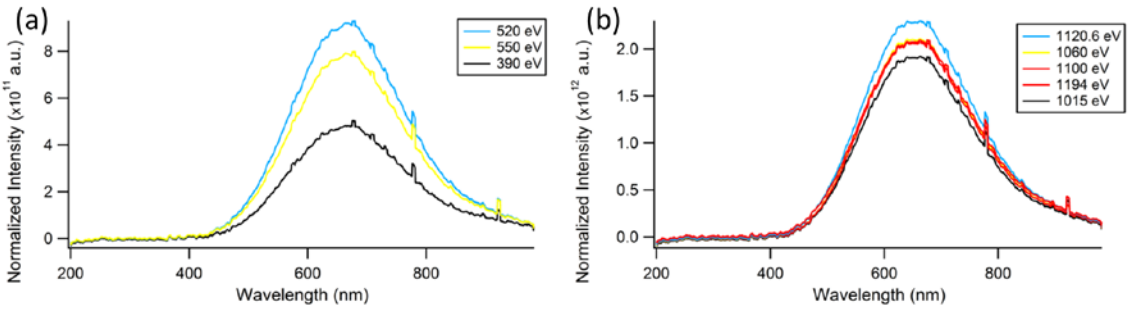

Figure 4-3 XEOL cuts taken across (a) N and O *K* and (b) Zn and Ga $L_{3,2}$ edges of GZNO.

This luminescence has been attributed to electrons bound to O donors at the bottom of the conduction band recombining with holes bound to Zn acceptors and was discussed in a recent report [11]. Across the Zn and Ga $L_{3,2}$-edges, inversion in the PLY does not occur. Here, the X-ray penetration depth (~160–600 nm) is greater than the size (diameter) of the GZNO nanoparticles, favouring a more complete thermalization process, and the luminescence intensity qualitatively tracks the change in X-ray cross section as one scans across the absorption edges (edge jump is less abrupt compared to the N and O *K*-edges). The creation of Zn and Ga *core-holes* ($2p_{3/2}$ and $2p_{1/2}$) results in electrons in the

conduction band and holes in the valence band, and subsequently, XEOL tracks the production of optical photons due to the recombination of these electron–hole pairs through charge transfer (traps) and energy transfer to defect states that decay optically.

4.3.2 2D XAFS-XEOL of GIZNO

2D XAFS–XEOL maps and corresponding PLY traces of the In doped sample, GIZNO, are shown in Figure 4-4.

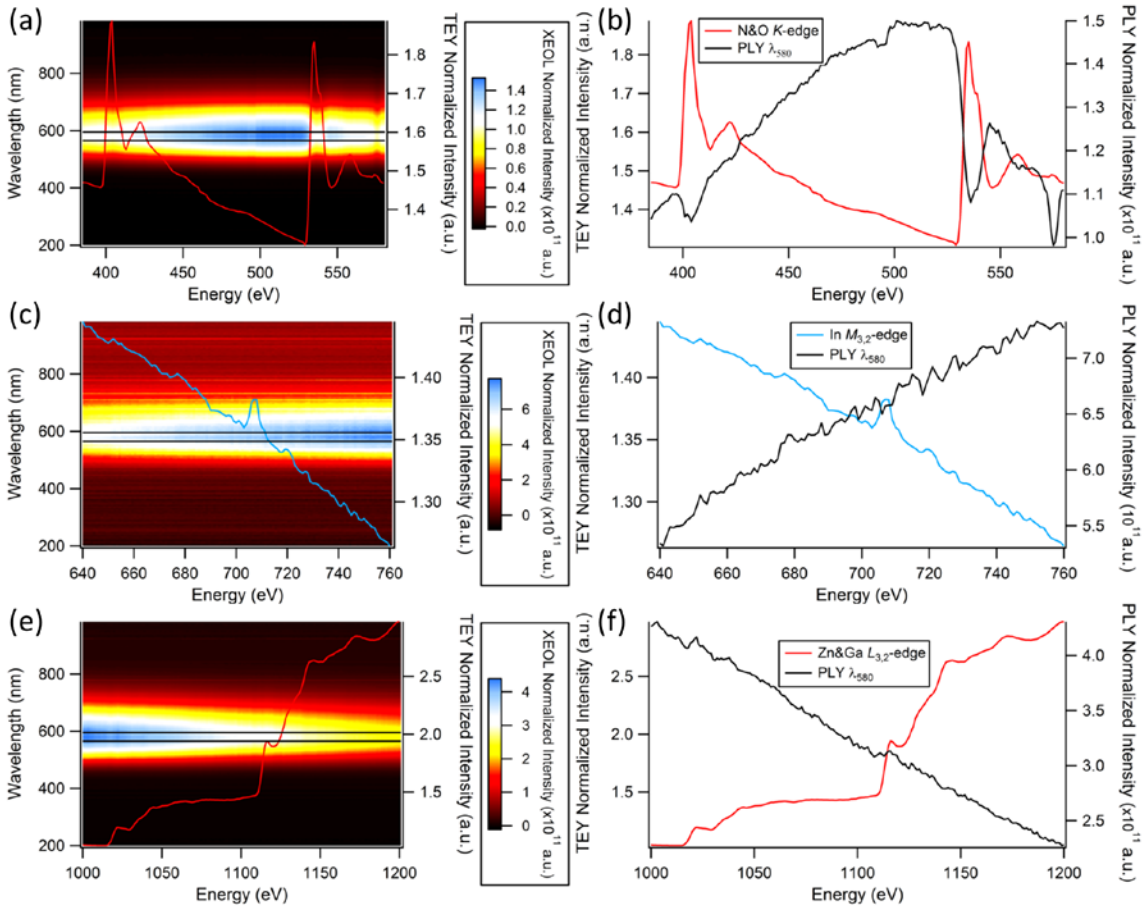

Figure 4-4 GIZNO XAFS–XEOL results: a) 2D XAFS–XEOL scan across N and O *K*-edges, TEY overlaid on scan (red), black horizontal line denotes the window where optical-XAFS were collected; b) PLY (black) vs TEY across N and O *K*-edges; c) 2D XAFS–XEOL scan across In $M_{3,2}$-edges, TEY overlaid on scan (light blue); d) PLY (black) vs TEY across In $M_{3,2}$-edges; e) 2D XAFS–XEOL scan across Zn and Ga $L_{3,2}$-edges, TEY overlaid on scan (red); f) PLY (black) vs TEY across Zn and Ga $L_{3,2}$-edges.

At first glance, the 2D XAFS–XEOL maps of the In doped sample, GIZNO (Figure 4-4), and the corresponding PLY $\lambda_{580\ nm}$ traces, appear very similar to those of GZNO, especially at the N and O *K*-edges. The XANES are also similar to those of GZNO, albeit with noticeable broadening, indicating some disorder. There are several clearly noticeable differences, however: (1) λ_{max} for the XEOL of GIZNO is blue shifted to ~580 nm from ~640 nm in GZNO; (2) the luminescence band is narrower than in GZNO; (3) the intense region of the luminescence channel, above the N *K*-edge and below the O *K*-edge, is spread out over a larger excitation energy range (Figure 4-4(a) and (b); see Figure 4-5(a) for representative XEOL cuts); and (4) the luminescence increases gradually across the In $M_{3,2}$-edges and reaches a maximum above the In *M*-edges and below the Zn *L*-edges (Figure 4-4(d) and (f))). The luminescence channel is insensitive across the Zn and Ga $L_{3,2}$-edges (Figure 4-4(e) and (f); see Figure 4-5(b) for representative XEOL cuts). This observation is in contrast to the behaviour of the GZNO sample, which shows positive edge jump in PLY at both edges.

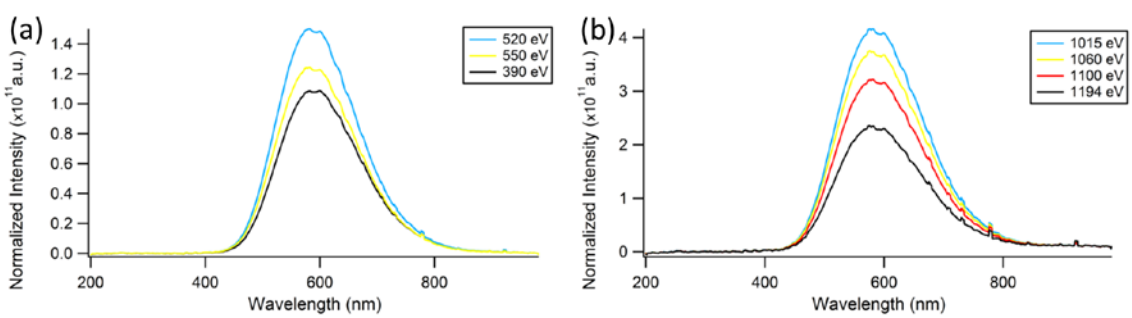

Figure 4-5 XEOL cuts taken across N and O *K* (a) and Zn and Ga $L_{3,2}$ (b) edges of GIZNO respectively.

4.3.3 Zn, Ga, and In *K*-edge XANES of GZNO and GIZNO

The above observations suggest that optical luminescence from GZNO, when In is absent, is either quenched or suppressed by the presence of In, which either gives rise to nonradiative channels or induces energy transfer to a different optical channel. We shall return to this point below. Qualitatively it appears as if indium doping has a strong effect

on the nature of the luminescence band (i.e., blue-shifted and narrower) and a strong effect on the emission intensity pattern above the O *K*-edge. Below the O *K*-edge, the emission intensity pattern does not appear as affected by the addition of an In dopant. These are the results of total absorption due to short penetration depths. Thus, the 2D XAFS–XEOL is a good illustration of the overall XEOL efficiency of the light-emitting materials in question.

To obtain a more quantitative explanation for the large differences observed in the XEOL between GZNO and GIZNO, hard X-ray spectroscopy was employed to study the local chemical environment of Ga and Zn in GZNO and GIZNO and of In in GIZNO. Because the penetration depth of hard X-rays is much greater than the sample thickness (nanoparticle diameter, nanosheet dimensions), the bulk properties of GZNO and GIZNO are being probed at these energies when collected in transmission and fluorescence detection modes and there is no saturation effect. The Ga, Zn, and In *K*-edges measure the 1s→ np transitions ($n \geq 4$ for Zn and Ga and $n \geq 5$ for In) and are highly sensitive to oxidation state and local chemical environment of the absorbing atom. Because Ga, Zn and In are in the vicinity of each other in the periodic table, their absorber atom phase shifts are very similar; also, O and N have a very similar back-scattering phases (nearly linear in k space) and monotonic back-scattering amplitudes. We would expect that, in an ideal solid solution, the absorption edges of Ga and Zn would be nearly identical, as the two absorbers would exist in the same chemical environment, in this case, a wurtzite structure containing an equal distribution of N and O nearest neighbours. In a non-ideal solid solution we would expect the minor component, which in the case of both GZNO and GIZNO is ZnO ($x \approx 0.25$), to show a greater amount of perturbation in the near-edge region. From Figure 4-6(a) and (b), as expected for GaN-ZnO solid solutions of similar stoichiometry, such as GZNO and GIZNO, the respective Zn and Ga absorption edges are essentially identical. Additionally, there is no apparent distortion of the local chemical environment of Zn and Ga atoms due to In doping in GIZNO.

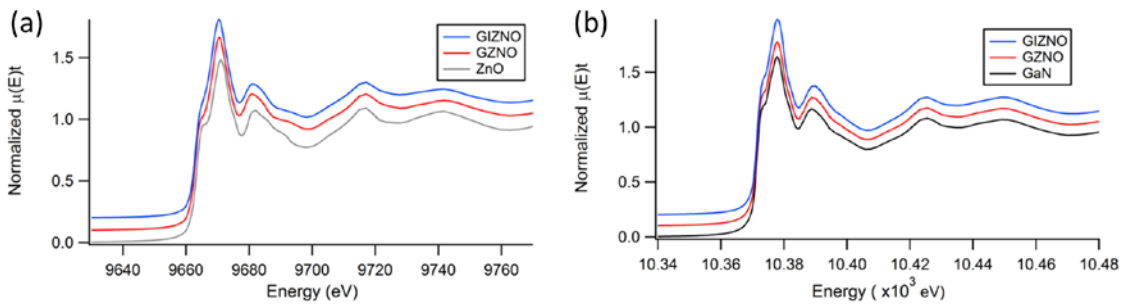

Figure 4-6 GZNO and GIZNO XANES at the Zn (a) and Ga (b) *K*-edge.

By setting the excitation threshold energy (E_0) for the Zn and Ga *K*-edge absorption spectra of GZNO and GIZNO, as well as that of the GaN and ZnO references, to 0 eV (Figure 4-7(a) and (b)), it is possible to identify whether Zn is in a GaN or ZnO local chemical environment (or, conversely, whether Ga is in a GaN or ZnO environment). The first feature in the Zn *K*-edge of both GZNO and GIZNO (Figure 4-7(a)), denoted by the vertically dashed line labelled a, shows a distortion of the Zn local environment by Ga (GaN).

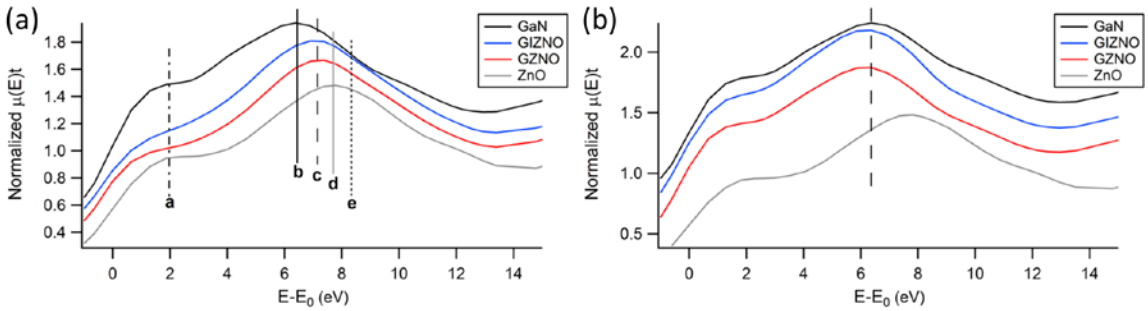

Figure 4-7 GZNO and GIZNO E_0 set to 0 eV: (a) Zn *K*-edge, near edge region;vertical line a and d marks the energy position of the first and second resonance of ZnO, respectively; vertical line b and c marks the second resonance of GaN, and GZNO and GIZNO respectively (b) Ga *K*-edge, near-edge region; vertical dashed line denotes the position of the multiple scattering resonance.

The intense peak at ~7.6 eV (denoted by vertical line d) is shifted to ~7 eV (vertical dashed line c) towards that of GaN at ~6.4 (vertical line b). The features of the Zn *K*-edge at e are more ZnO-like then GaN-like. Although GZNO and GIZNO are GaN-rich

solid solutions, there is still a large ZnO component (~25%), and thus the Zn *K*-edge spectra reflect this in a shift of all features towards GaN. The progressive shift of this peak can be qualitatively interpreted as a slightly expanded environment for Zn since the position of the multiple scattering peaks relative to the threshold is inversely proportional to the square of the interatomic distance, for example, Zn–O or Zn –N in the first shell.

At the Ga *K*-edge, one can clearly see that there is very little distortion of the near-edge region with respect to that of GaN. Thus, the local structure of Ga generally holds and exhibits more GaN than ZnO character, as expected. Finally, close inspection of the near-edge region of GZNO and GIZNO suggests that In doping does not induce distortion in the local chemical environment of Zn or Ga. This is contrary to what would be expected, as In(III) is larger than Zn(II) or Ga(III), unless the amount of In is insufficient to induce a distortion. Additionally, this poses questions about the large effect of the addition of indium on the optical and growth properties of GIZNO. Studying the In *K*-edge allows the local chemical environment of indium in GIZNO to be identified, and by a similar argument, it should enable the determination of whether In is exhibiting Zn, Ga, or some other absorber behaviour.

Indium *K*-edge XANES measures In 1s→5p transitions and is highly sensitive to the oxidation state and local chemical environment of indium. From the near-edge region (Figure 4-8(a)), it is apparent that In in GIZNO is predominately present as indium oxide.

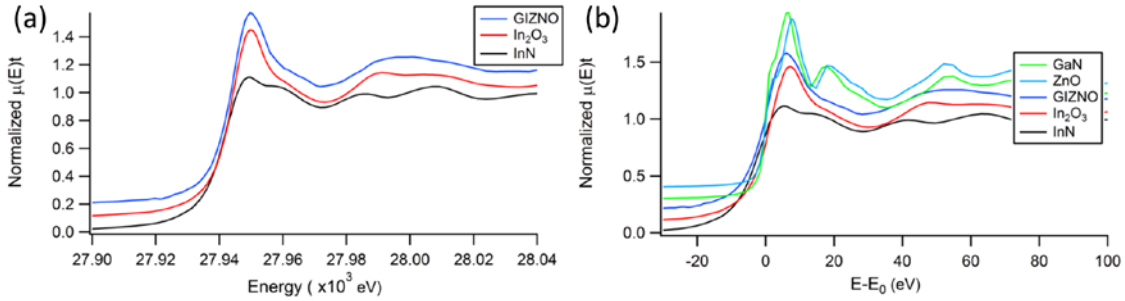

Figure 4-8 GIZNO In *K*-edge: (a) GIZNO, In_2O_3, and InN; (b) GIZNO and reference standards, E_0 set to 0 eV.

Some distortion is observed in the multiple-scattering peaks above the In absorption edge, which suggests that this may be a thin surface oxide with distortion due to the interface between the surface of the GaN-ZnO nanosheets and the thin surface oxide layer. To compare the local environment of indium to that of GaN and ZnO, the threshold energy (E_0) was set to 0 eV (Figure 4-8(b)) for the Zn, Ga, and In absorption edges of ZnO, GaN, GIZNO, and the In reference standards (InN and In_2O_3). It is clear that the local environment of indium in GIZNO is not ZnO-, GaN-, or InN-like. Further evidence for indium being present predominantly as a surface oxide can be found in our previous soft X-ray results for GIZNO, as well as the 2D XAFS–XEOL discussed above (Figure 4-4). A slight distortion was observed in the total electron yield (TEY) XANES spectra of all absorption edges (N and O *K*-edges and Zn and Ga $L_{3,2}$-edges) of GIZNO relative to GZNO, which we previously attributed to indium incorporation into the solid solution (In^{3+} larger than Ga^{3+} and Zn^{2+}) [11]. Because TEY is surface-sensitive, the slight distortion in these XANES spectra of GIZNO is also consistent with the formation of a thin surface oxide layer. The dissolution of In^{3+} into the lattice cannot be totally rejected at this time because of the more extended region of the XANES spectrum (~ 45 eV and ~ 70 eV above the threshold is distorted in GIZNO versus In_2O_3).

These results can be used to explain the differences in the XEOL of GIZNO vs. GZNO. The optical luminescence band observed at ~580 nm (2.12 eV) for GIZNO is likely produced predominately by the In_2O_3 surface oxide layer in GIZNO and not the bulk GaN-ZnO nanomaterial (see Figure 4-5). This band has been observed in PL studies of other In_2O_3 nanomaterials and has been attributed to oxygen-vacancy trap states [24-26]. The most common oxygen vacancies for semiconducting oxides are V_O, $V_O^{\cdot}$, and $V_O^{\cdot\cdot}$. It has been demonstrated by EPR spectroscopy that the paramagnetic singly ionized $V_O^{\cdot}$ state is common in oxygen-deficient In_2O_3 and that luminescence is likely due to radiative recombination of a photo-generated hole with an electron occupying the oxygen vacancy [27]. It is likely that this very thin surface oxide would be oxygen-deficient due to the high temperature (850 ℃) ammonia-rich growth environment, suggesting the formation of an In_2O_{3-x} suboxide surface layer. One then must ask the question of what happens to the luminescence from GZNO that presumably emits at ~640 nm. It can be argued that the presence of the In_2O_3 overlayer must have facilitated energy transfer from

GZNO to the optical channel of the surface In_2O_3 layer and quenched the GZNO luminescence, although we cannot rule out that a small amount of In^{3+} did dissolve into the lattice, shifting the energy of the defect state to the blue. It should be noted that, in nanocomposites, the effect of interface is much greater than that in bulk structures. It is likely that both effects contribute to the observation of the 580 nm emission in GIZNO as compared to the 640 nm emission in GZNO although In_2O_3 almost certainly makes the dominant contribution. This notion is also consistent with the observation that the PLY of GIZNO is insensitive to the edge jump at the Zn and Ga *L*-edges.

4.3.4 In *K*-edge EXAFS of GIZNO

Further evidence for a thin indium oxide surface layer can be found by studying the In *K*-edge EXAFS spectrum of GIZNO (Figure 4-9). From the extended region of the X-ray absorption spectrum, where single scattering dominates, there appears to be diminishing long-range order (Figure 4-9(a)).

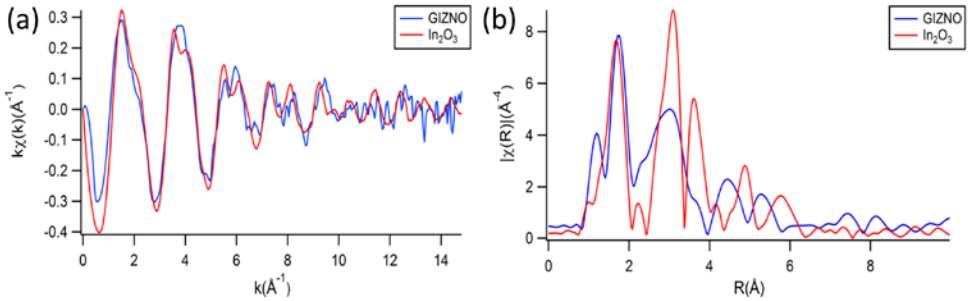

Figure 4-9 GIZNO In *K*-edge EXAFS: (a) in *k*-space, *k* weighted; (b) in *R* space, k^3 weighted.

Although the amplitudes of the EXAFS appear to be similar for both GIZNO and In_2O_3, the back transform to *R* space (Figure 4-9(b), k^3 weighted to emphasize outer coordination shells) indicates that the amplitude of the second coordination shell of GIZNO is diminished, and thus, In_2O_3 exists as a very thin surface layer. Although the first coordination shell for both GIZNO and indium oxide have similar amplitudes, the diminishing long-range order, subsequent decrease in the magnitude of the second

coordination shell, and previous EDS data (see ref 11) are consistent with a very thin (subnanometer) surface oxide layer, it is possible that surface hydroxides from water are responsible for the greater than expected amplitude of the first coordination shell in the EXAFS of GIZNO.

The above analysis strongly suggests that the introduction of indium into the precursor used to grow GaN-ZnO solid solution nanomaterials (GIZNO) does not appear to have resulted in a $Ga_{1-x-y}Zn_xIn_yN_{1-x}O_x$ solid solution with any significant amount of In, as the Zn and Ga *K*-edge XANES of GZNO and GIZNO are nearly identical, which implies similar composition of the solid solutions. Instead, indium appears to have formed a very thin (subnanometer) surface oxide, as evidenced from the XEOL band at ca. 580 nm, the In *K*-edge XANES spectrum, distortion of the N & O *K*-edge and Zn & Ga $L_{3,2}$-edge TEY XANES spectra, and the lack of long-range order in the In *K*-edge EXAFS spectrum.

In our proposed growth model of GIZNO nanosheets , we suggested that the 2D sheet growth is initiated by the formation of an ultrathin In layer and that the continuing dissolution of Ga, In, Zn, and O then generates a supersaturated solution wherein the growth of GIZNO nanosheets occurs through precipitation from the supersaturated liquid [11]. The observation of a surface In_2O_3 layer supports the initial stage of this mechanism and the formation of a nanosheet. Most likely, the outer layer is still In, which is easily oxidized. We thus can divide In into two parts: the first part is in the In_2O_3 surface layer, and the second part is incorporated into the GZNO solid solution. Since the total detected In ratio is only 1–2%, the effect of surface In_2O_3 layer is contributing more significantly to the XEOL.

XEOL observed for GIZNO appears to be the result of surface-layer absorption and energy transfer from the solid solution to the indium surface oxide. The intensity of the XEOL is inverted at the N *K*-edge, increases rapidly after the inversion above the N 1s threshold, and decreases again with the “turn on” of the O 1s *core-hole*. The inversion at the O *K*-edge is more significant in GIZNO than in GZNO, providing further evidence for the presence of a thin surface oxide from which Auger electrons can escape the

surface more readily without contributing to the thermalization, and, hence, luminescence. Energy transfer from the surface of the GaN-ZnO nanosheet to the indium surface oxide layer appears to be sensitive to the N and O 1s excitations, with a decrease in efficiency when the oxygen and nitrogen core levels compete for X-rays. It should also be noted that the In *M*-edge jump is quite small (a few percent), so most of the photons are still absorbed by O in the indium oxide surface and the GZNO substrate. The XEOL intensity reaches a maximum above the In M_2-edge and below the Zn L_3-edge, which suggests that e–h pair production is most efficient once the In core levels become accessible. Luminescence decreases monotonically as the X-ray photon energy is scanned across the Zn and Ga $L_{3,2}$-edges, and a positive edge jump is barely noticeable, which suggests that energy transfer from the de-excitation of these core levels to the GIZNO optical channel (largely In_2O_3 defect origin) is not as efficient in GIZNO at these edges compared with those from GZNO to optical channel of GZNO origin. Moreover, a larger fraction of the incident X-ray is now absorbed by the indium surface oxide layer, producing a high PLY background across the Zn and Ga $L_{3,2}$-edges.

4.4 Conclusions

We have reported a XANES and XEOL study of GZNO nanoparticles and GIZNO nanosheets. The XEOL observed at ~640 nm from GZNO is due to the recombination of e–h pairs through donor–acceptor states. We have introduced a 2D XAFS–XEOL technique, which clearly illustrates that well above the nitrogen *K*-edge, where photon penetration is the highest, there is a gradual increase in luminescence due to an efficient thermalization process. There is a sharp decrease in luminescence quantum yield as a result of increased competition for available X-ray photons by newly accessible shallow core levels such as the N and O *K*-edges. The excitation of electrons from the Zn and Ga $L_{3,2}$ core levels ($2p_{3/2}$ and $2p_{1/2}$) results in electrons in the conduction band and holes in the valence band, both directly (primary excitation) and indirectly (secondary process, often the dominant one), and subsequently, XEOL tracks the production of optical photons due to the recombination of these electron–hole pairs following charge/energy transfer to the most appropriate emitting state. The addition of indium to the starting material results in a change in morphology from nanoparticles (GZNO) to

nanosheets (GIZNO), and the presence of indium oxide on the surface of the nanosheet is clearly evident, whereas In dissolution into the lattice forming the solid solution is relatively small. Indium in GIZNO is mainly present as an extremely thin surface oxide layer, which is evident from the In *K*-edge XANES and EXAFS spectra. XEOL is observed at ~580 nm (2.12 eV) for GIZNO, which is consistent with luminescence observed from In_2O_3 nanostructures, and the presence of the indium oxide surface layer suppresses the GIZNO emission of a non-indium oxide origin (e.g. bulk GZNO emission). We have also shown that 2D XAFS–XEOL is a powerful method for studying the optical luminescence properties of semiconducting nanomaterials, and, in particular, for tracking the efficiency of the X-ray excited luminescence channel across absorption edges of nanostructures of different sizes and morphologies.

4.5 References

[1] K. Maeda, T. Takata, M. Hara, N. Saito, Y. Inoue, H. Kobayashi, and K. Domen, *J. Am. Chem. Soc.*, **127**, 8286 (2005)

[2] X. Chen, S. Shen, L. Guo, and S. S. Mao, *Chem. Rev.*, **110**, 6503 (2010)

[3] J. Wang, B. Huang, Z. Wang, P. Wang, H. Chen, Z. Zheng, X. Qin, X. Zhang, Y. Dai, and M. H. Whangbo, *J. Matter. Chem.*, **21**, 4562 (2011)

[4] K. Maeda, K. Teramura, T. Takata, M. Hara, N. Saito, K. Toda, Y. Inoue, H. Kobayashi, and K. Domen, *J. Phys. Chem.* B, **109**, 20504 (2005)

[5] K. Maeda, and K. Domen, *J. Phys. Chem.* C, **111**, 7851 (2007)

[6] W. Wei, Y. Dai, K. Yang, M. Guo, and B. Huang, *J. Phys. Chem.* C, **112**, 15915 (2008)

[7] M. Yoshida, T. Hirai, K. Maeda, N. Saito, J. Kubota, H. Kobayashi, Y. Inoue, and K. Domen, *J. Phys. Chem.* C, **114**, 15510 (2010)

[8] W. Han, Z. Liu, and H. Yu, *App. Phys. Lett.*, **96**, 183112 (2010)

[9] W. Q. Han, Y. Zhang, C. Y. Nam, C. T. Black, and E. E. Mendez, *App. Phys. Lett.*, **97**, 083108 (2010)

[10] K. Kamata, K. Maeda, D. Lu, Y. Kako, and K. Domen, *Chem. Phys. Lett.*, **470**, 90 (2009)

[11] W. Q. Han, M. J. Ward, and T. K. Sham, *J. Phys. Chem.* C, **115**, 3962 (2011)

[12] L. Armelao, F. Heigl, S. Brunet, R. Sammynaiken, T. Reiger, R.I. Blyth, L. Zuin, R. Sankari, J. Vogt, and T.K. Sham, *ChemPhysChem*, **11**, 3625 (2010)

[13] W. Q. Han, D. Su, M. Murphy, M. Ward, T. K. Sham, L. J. Wu, Y. M. Zhu, Y. F. Hu, T. Aoki, *Journal of Materials Research*, **25**, 711 (2010)

[14] X. H. Sun, S. Lam, T. K. Sham, F. Heigl, A. Jurgensen, and N. B. Wong, *J. Phys. Chem.* B, **109**, 3120 (2005)

[15] A. Rogalev, and J. Goulon, in *Chemical Applications of Synchrotron Radiation*, Part II: X-ray Applications; Sham, T.K., Ed.; World Scientific: River Edge, NJ, 2002; Vol 12B, pp 707-760.

[16] T. Reiger, J. Krochak, T. K. Sham, Y. F. Hu, J. Thompson, and R. I. R. Blyth, *Nucl. Instrum. Methods Phys. Res.*, Sect. A, **582**, 93 (2007)

[17] F. Heigl, S. Lam, T. Reiger, I. Coulthard, and T. K. Sham, *J. Am. Chem. Soc.*, **128**, 3906 (2006)

[18] T. K. Sham, D. T. Jiang, I. Coulthard, J. W. Lorimer, H. X. Feng, K. H. Tan, S. P. Frigo, R. A. Rosenberg, D. C. Houghton, and B. Bryskiewicz *Nature*, **363**, 331 (1993)

[19] L. Armelao, F. Heigl, A. Jürgensen, R. I. R. Blyth, T. Regier, X. T. Zhou, and T. K. Sham, *J. Phys. Chem.* C, **111**, 10194 (2007)

[20] R. A. Rosenberg, G. K. Shenoy, F. Heigl, S.-T. Lee, P.-S. G. Kim, X.-T. Zhou, and T. K. Sham, *Appl. Phys. Lett.*, **86**, 263115 (2005)

[21] P.-S. Kim, T. K. Sham, P. Zhang, M. K. Fung, S. T. Lee, Y.-F. Hu, and B. W. Yates, *J. Am. Chem. Soc.*, **123**, 8870 (2001)

[22] T. K. Sham, S. J. Naftel, and I. Coulthard, in *Chemical Applications of Synchrotron Radiation*, Part II: X-ray Applications; Sham, T.K., Ed.; World Scientific: River Edge, NJ, 2002; Vol 12B, pp 1154-1212.

[23] T. K. Sham, *International Journal of Nanotechnology*, **5**, 1194 (2008)

[24] S.-T. Jean, and Y.-C. Her, *Cryst. Growth Des.*, **10**, 2104 (2010)

[25] J. S. Jeong, J. Y. Lee, C. J. Lee, S. J. An, and G.-C. Yi, *Chem. Phys. Lett.*, **384**, 246 (2004)

[26] H. S. Kim, H. G. Na, J. C. Yang, C. Lee, and H. W. Kim, *Acta Phys. Pol.* A, **119**, 143 (2011)

[27] X. S. Peng, G. W. Meng, J. Zhang, Y. W. Wang, C. Z. Wang, and L. D. Zhang, *J. Mater. Chem.*, 12, 1602 (2002)

Chapter 5

5 Effects of Nitridation Temperature on $Ga_{1-x}Zn_xN_{1-x}O_x$ Solid Solution Nanocrystal Growth: An XAFS and XEOL Study

5.1 Introduction

Visible light driven photocatalytic overall water splitting into hydrogen and oxygen is a highly attractive process for the production of hydrogen gas for use as an efficient energy carrier. The first report of the synthesis of solid solutions of gallium nitride and zinc oxide, $(Ga_{1-x}Zn_x)(N_{1-x}O_x)$, by Maeda et al. identified these novel materials as potential photocatalysts for overall water splitting into H_2 and O_2 under visible irradiation [1]. Both GaN and ZnO are wide band-gap semiconductors with E_{gap} = 3.4 eV [2] and $E_{gap} \approx 3.3$ eV [3] respectively, but, when alloyed together to form a $(Ga_{1-x}Zn_x)(N_{1-x}O_x)$ solid solution the band-gap is narrowed into the visible region with $E_{gap} < 3$ eV [1]. Since their discovery an intense research effort has been directed at the synthesis and characterization of $(Ga_{1-x}Zn_x)(N_{1-x}O_x)$ solid solutions [4- 16], but, it is still unclear why the band-gap narrows over the parent materials and whether or not the material is best described as a homogeneous or heterogeneous solid solution. Band-gap (BG) narrowing in these $(Ga_{1-x}Zn_x)(N_{1-x}O_x)$ solid solution materials is known to vary as a function of x (or ZnO concentration), with an increase in x corresponding to a narrowing of the BG further into the visible region of the solar spectrum [4]. Thus it is important to develop synthesis methods for producing ZnO-rich $(Ga_{1-x}Zn_x)(N_{1-x}O_x)$ solid solutions. Recent synthetic efforts for the production of ZnO rich $(Ga_{1-x}Zn_x)(N_{1-x}O_x)$ solid solutions, including a solution combustion method [17], using layered double hydroxides as precursors [18], and using mixtures $ZnGa_2O_4$ and ZnO nanocrystals as synthetic precursors [19], have been successful at producing solid solutions with x tunable from ~0.3 to 0.9 and a corresponding decrease in band-gap energy from ~2.7 to 2.2 eV over this compositional range. Another synthetic route for controlling the ZnO concentration in $(Ga_{1-x}Zn_x)(N_{1-x}O_x)$ solid solutions is to vary the nitridation temperature. This has recently been demonstrated to be effective for the synthesis of $(Ga_{1-x}Zn_x)(N_{1-x}O_x)$

nanocrystals with atomic ratios of Zn/(Ga + Zn) ranging from ~0.09 to 0.48 with a corresponding reduction of band-gap energy from ~2.65 to 2.21 eV, using nitridation temperatures ranging from 850 to 650 ℃ [20]. It was determined, however, that using a nitridation temperature below 650 ℃ resulted in the presence of an additional spinel $ZnGa_2O_4$ phase, which was identified via X-ray diffraction [20]. In order to produce a highly active photocatalyst it is important to suppress the recombination of photogenerated electrons and holes to maximize the number of carriers that can participate in surface chemical reactions [21]. Using a low synthesis temperature can result in poor crystallinity of the resultant solid solution, and the subsequent formation of defects, which act as trapping and recombination centers between photogenerated electrons and holes resulting in a decrease in photocatalytic activity [22]. Thus it is important to produce a solid solution with a high degree of crystallinity and low defect concentration to maximize the number of photogenerated electrons and holes that can participate in water oxidation and reduction reactions at the surface of the photocatalyst. In order to study the effects of nitridation temperature on the synthesis of $(Ga_{1-x}Zn_x)(N_{1-x}O_x)$ solid solutions (GZNO) we have investigated a series of GZNO nanocrystals synthesized at different nitridation temperatures using a combination of X-ray absorption spectroscopy and X-ray excited optical luminescence.

X-ray absorption near edge structure (XANES) refers to the modulation of the X-ray absorption coefficient in the near-edge region (from the edge up to ~50 eV above the threshold) of a particular core-level electron of an atom in a material. XANES is often referred to as the near-edge region of the XAFS (X-ray absorption fine structure) which includes both the near-edge region and the extended region, the extended X-ray absorption fine structure (EXAFS). By exciting the core-level electrons of an element in a chemical environment to previously unoccupied electronic states with a tunable synchrotron light source, one can probe the local symmetry and occupation of these states of which the characteristics are governed by the local chemistry. Meanwhile, X-ray excited optical luminescence (XEOL), an X-ray photon- in optical photon- out technique, is used to monitor the optical luminescence (UV–Vis–NIR) excited using a selected X-ray photon energy, which can excite a particular core-level electron of a given element of interest to bound, quasi-bound, and continuum states, providing elemental, and in some

cases site specificity. The energy absorbed is in part transferred to optical de-excitation channels, resulting in optical luminescence. Thus XEOL is different from conventional UV-visible photoluminescence in that it can be site specific since the core level is specific to a given element and that it involves energy transfer via secondary processes to the optical channel (thermalization of electrons and holes) in condensed matter studies. The extent of this X-ray energy conversion to optical photons depends on the nature of excitation channel (*K* or *L* shell etc.), and the nature of the material, e.g. crystallinity, morphology, size and proximity effects (surface and interface). Herein, we present the results of an XAFS and XEOL study of the effects of nitridation temperature on the synthesis of these novel GZNO semiconducting nanomaterials.

5.2 Experimental

5.2.1 Synthesis

Solid solution nanocrystals of gallium nitride – zinc oxide (GZNO) were synthesized as reported previously [20]. Briefly, a Ga-Zn-O (GZO) precursor was prepared by mixing gallium nitrate hydrate and zinc acetate dihydrate in a solution of ethanolamine. After stirring at 65 °C for 2 h, the GZO solution was aged for 1 week at 0 °C. The resulting gel-like precursor was sintered in a 400 °C oven for 1 h in ambient air. Finally the dry GZO precursor was reacted with ammonia for 10 h at different nitridation temperatures. Samples GZNO-2, 3, and 4 were nitridated at 650, 750, and 850 °C, have average particle sizes of ~10, 17, and 27 nm, and have atomic Zn ratios [Zn/(Zn + Ga)] of 0.482, 0.379, and 0.088 respectively [20].

5.2.2 Synchrotron Radiation Spectroscopy

Gallium and zinc $L_{3,2}$-edge and oxygen and nitrogen *K*-edge XANES and XEOL measurements of samples GZNO-2, 3, and 4 were carried out at the undulator-based spherical grating monochromator (SGM) beam-line of the Canadian Light Source (CLS) at the University of Saskatchewan [23]. CLS is a 2.9 GeV third-generation light source operating in fill-up mode with a ring current of 250 mA at injection. Powdered samples were prepared on copper sample holders by applying a thin uniform layer of the powder to carbon tape. XANES was recorded in total electron yield (TEY) detection mode on the

SGM beam-line. XEOL spectra (200–900 nm) were collected using an Ocean Optics QE 65000 dispersive optical spectrophotometer at selected X-ray excitation energies across the Ga and Zn $L_{3,2}$ and O and N *K* edges.

Gallium and zinc *K*-edge XANES and EXAFS measurements of samples GZNO-2, 3, and 4 were carried out at the bending magnet-based PNC/XSD 20-BM beam-line of the Advanced Photon Source (APS) at Argonne National Laboratory, Argonne, IL [24]. APS is a 7.0 GeV third-generation light source operating in top-up mode at a ring current of 100 mA. Uniform powder samples were prepared on Kapton tape, and the tape was folded to a thickness of ~1–2 absorption lengths ($1/\mu$). The detection mode was fluorescent X-ray yield recorded using a 13-element Canberra detector (model # GL0110S). The detector count rate was kept below 50000 counts to prevent saturation. All spectra were normalized to dead-time corrected I_0, measured using an ion chamber filled with 100% N_2. Reference foil standards used for energy calibration were measured in transmission mode downstream of the sample between two ion chambers filled with an 85:20 sccm N_2/Ar mixture.

5.3 Results and Discussion

5.3.1 TEM, XRD, and UV-Vis diffuse reflectance of $Ga_{1-x}Zn_xN_{1-x}O_x$ Nanocrystals

Figures 5-1(a), (b), and (c) show TEM images of samples GZNO-2, 3, and 4 synthesized at nitridation temperatures of 650, 750, and 850 ℃ respectively. Particles are typically single crystal with a thin amorphous surface oxide layer. Figure 5-1(d) shows X-ray diffraction (XRD) patterns of samples GZNO-2, 3, and 4. From XRD the samples appear to be characterized by a single hexagonal wurtzite phase with a strong (101) peak. The (101) peak shifts towards a larger 2θ angle (see Figure 5-1(d)) with increasing nitridation temperature and the subsequent decrease in the Zn/(Zn + Ga) ratio. This shift has previously been attributed to a decrease in the length of the *a*-axis lattice constant in the solid solution as the ratio of Ga/Zn increases [4,20]. This is a plausible explanation for the observed shift in the (101) peak since the ionic radius of Zn^{2+} (0.74 Å) is larger than that of Ga^{3+} (0.61 Å) [25].

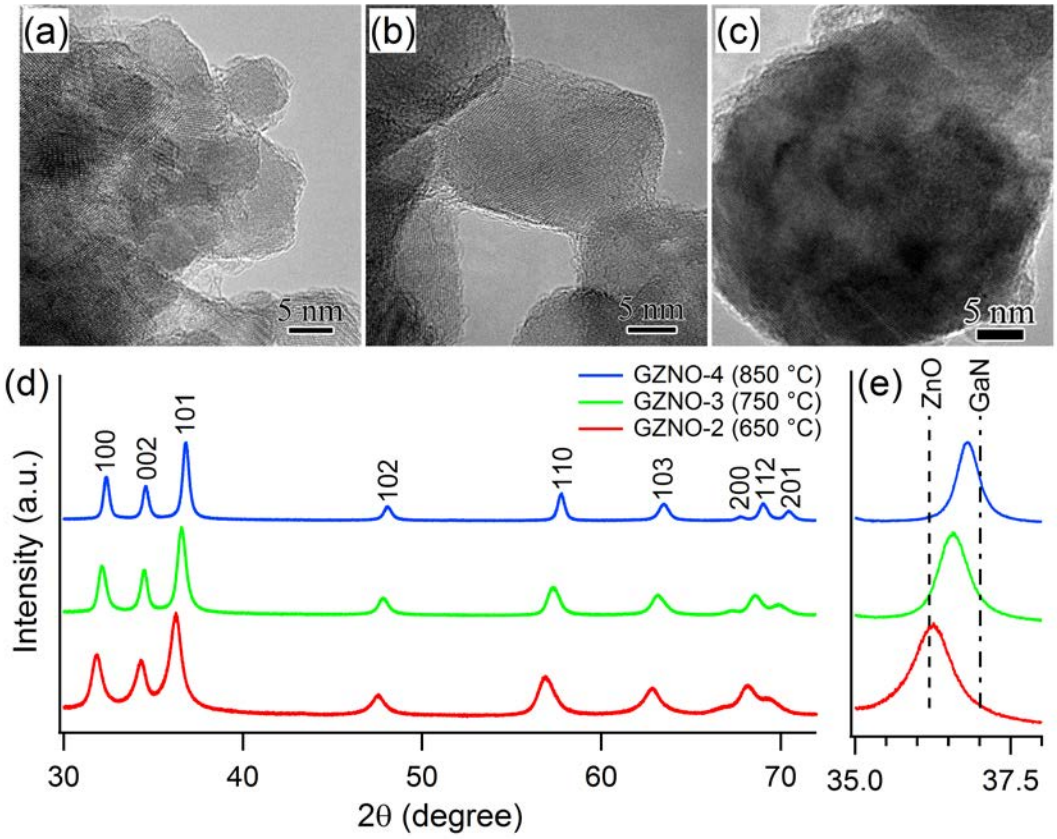

Figure 5-1 TEM images of nanocrystal samples GZNO-2, 3, and 4 synthesized at (a) 650 ℃ and (b) 750 ℃ and (c) 850 ℃ respectively. (d) XRD spectra of samples GZNO-2, 3, and 4. (e) Shift in the position of the (101) diffraction peak with respect to wurtzite ZnO and GaN.

Chen et al. studied the formation of GZNO solid solutions from the ammonolysis reaction of β-Ga_2O_3 and ZnO via in situ XRD and found that spinel $ZnGa_2O_4$ was a key growth intermediate [26]. Although, in our synthesis we use a Ga-Zn-O nanoparticulate precursor instead of β-Ga_2O_3 and ZnO, it appears that during nitridation the growth of GZNO solid solution nanocrystals goes through the same initial $ZnGa_2O_4$ phase formation as evidenced by the presence of an additional cubic spinel $ZnGa_2O_4$ phase in the XRD spectrum of GZNO nanocrystal samples synthesized using nitridation temperatures lower than 650 ℃ (not shown) [20]. In the spinel $ZnGa_2O_4$ lattice zinc atoms occupy tetrahedral sites and gallium atoms occupy octahedral sites, therefore in a spinel to wurtzite phase transformation the zinc atoms are not required to go through a big geometric rearrangement [26]. In the case of gallium, however, for a transformation

from a spinel $ZnGa_2O_4$ phase to a wurtzite GZNO phase at least two Ga-O bonds must be broken and some of the O atoms could then be replaced by N atoms to form the GZNO solution. Since the Ga-O bond (3.66 eV) is stronger than the Zn-O bond (1.65 eV) it is possible that Ga-O bond breaking could be the rate-limiting step in the phase transition from $ZnGa_2O_4$ to GZNO [26]. The progressive narrowing observed in XRD spectra of GZNO-2, 3, and 4 with increasing synthesis temperature is either due to an increase in nanocrystal size, an increase in crystallinity, or both.

Figure 5-2 shows the UV-Vis diffuse reflectance spectra of GZNO-2, 3, and 4 (*x* of ~ 0.482, 0.379, and 0.088 respectively) with band-gap energies of 2.21, 2.37, and 2.65 eV respectively estimated by extrapolating the linear region of the absorption on-set from each spectrum back to the *x* axis (Figure 5-2 dashed line).

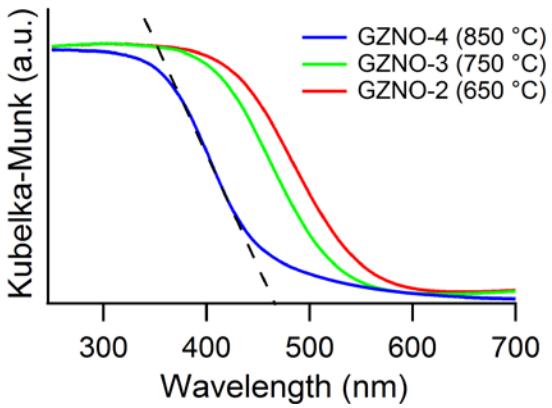

Figure 5-2 UV-Vis diffuse reflectance of GZNO-2, 3, and 4.

From the diffuse reflectance spectra of GZNO-2, 3, and 4 it is clear that regardless of the appropriate solid solution model (homogeneous or heterogeneous) the desired narrowing of the band-gap into the visible occurs as expected (BG narrows with increasing *x*). It is also apparent that the presence of a small amount of spinel phase $ZnGa_2O_4$ does not have a pronounced effect on band-gap narrowing. It has been suggested that the observed BG narrowing is due to p–d repulsion between N 2p and Zn 3d orbitals in the valence band

resulting in an upward shift of the valence band maximum, and a corresponding narrowing of the band-gap [1,4].

5.3.2 Zinc and Gallium *K*-edge XANES

The very high sensitivity and elemental specificity afforded by X-ray absorption spectroscopy makes it an excellent method for studying the composition and electronic structure of complex systems such as GZNO solid solutions. Hard X-ray spectroscopy was employed to study the local chemical environment of Ga and Zn in GZNO solid solution nanocrystals. At both zinc and gallium *K*-edges the X-ray cross section (σ) is small, hence the penetration depth of hard X-rays is much greater than the sample thickness (nanocrystal diameter) and the bulk properties of the GZNO samples are being probed at these energies when collected in transmission and fluorescence detection modes, and there is usually little saturation effect since the appropriate sample thickness can easily be prepared. The Ga and Zn *K*-edges measure the 1s→np transitions ($n \geq 4$ for Zn and Ga) and are highly sensitive to oxidation state and local chemical environment of the absorbing atom. Since Ga and Zn are neighbours in the 3rd row of the periodic table (Zn Group 12 and Ga Group 13), their absorber atom phase shift is very similar; also, O and N have a very similar back scattering phase (nearly linear in *k* space) and monotonic backscattering amplitude. We would expect that in an ideal solid solution the absorption edges of Ga and Zn would be nearly identical as both absorbers would exist in the same chemical environment, in this case a wurtzite structure containing a distribution of N and O nearest neighbours. In a non-ideal solid solution we would expect the minor component, which is the case for GZNO-2, 3, and 4 where ZnO ($x \approx 0.483$, 0.379, and 0.088 respectively) is the minor component, to show a greater amount of perturbation in the near-edge region. Figure 5-3(a) shows the zinc *K*-edge XANES of GZNO-2, 3, 4, and a ZnO standard for reference. All samples exhibit near edge features consistent with zinc oxide with a sharpening of all spectral features as nitridation temperature increases indicative of an increase in crystalinity.

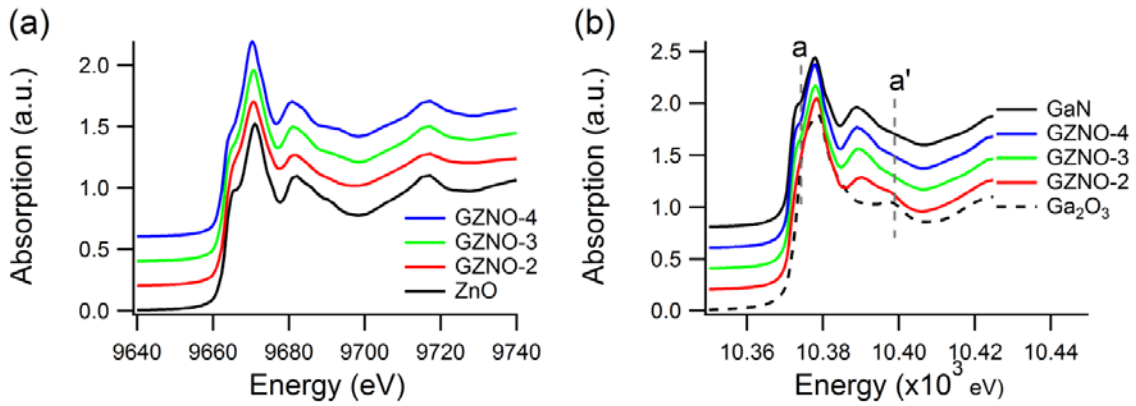

Figure 5-3 (a) Zinc *K*-edge XANES of GZNO-2, 3, and 4 and ZnO. (b) Gallium *K*-edge XANES of GZNO-2, 3, and 4, GaN and Ga_2O_3.

The gallium *K*-edge spectra for GZNO-2, 3, and 4 as well as those for GaN and β-Ga_2O_3 reference standards are displayed in Figure 5-3(b). Samples GZNO-3 and 4 exhibit near-edge features consistent with those of GaN. Sample GZNO-2 primarily exhibits a GaN near-edge structure, but, it is apparent that there is also an observable contribution from β-Ga_2O_3 (see Figure 5-3(b) vertical dashed lines a and a'). This suggests that while the bulk environment for zinc absorbers in GZNO-2 appears to be primarily wurtzite ZnO, there are at least two environments for gallium absorbers, α-GaN and β-Ga_2O_3. Thus it is likely that the synthesis temperature for GZNO-2, 650 ℃, is too low to achieve 100% conversion to wurtzite GaN. With synthesis temperatures ≥ 750 ℃, which is the case for samples GZNO-3 and 4, there appears to be only one bulk environment, ZnO or GaN, for zinc or gallium absorbers respectively. Since it is desirable to obtain GZNO solid solutions with a large value of *x*, or ZnO component, this is an important observation. If we want a highly crystalline single phase solid solution with a larger ZnO component we should use a synthesis temperature ≥ 750 ℃ which is high enough to ensure conversion to GaN occurs, but not high enough to allow for the volatilization of too much Zn(s) to occur. Using a synthesis temperature of ~750 ℃ still produces a crystalline GaN rich solid solution, but the ZnO component is large enough that the BG is extended well into the visible region (2.37 eV or ~ 520 nm) of the solar spectrum.

A closer examination of the near-edge region at the zinc *K*-edge (Figure 5-4(a)) shows an energy shift in the multiple-scattering (MS) peaks. The position of the intense MS feature at the Zn *K*-edge (see Figure 5-4(a) vertical dashed line **b**) is shifted to progressively lower energy with respect to ZnO as *x* (the ZnO component) decreases, and reaches a minimum for GZNO-4 (see Figure 5-4(a) vertical dashed line **a**).

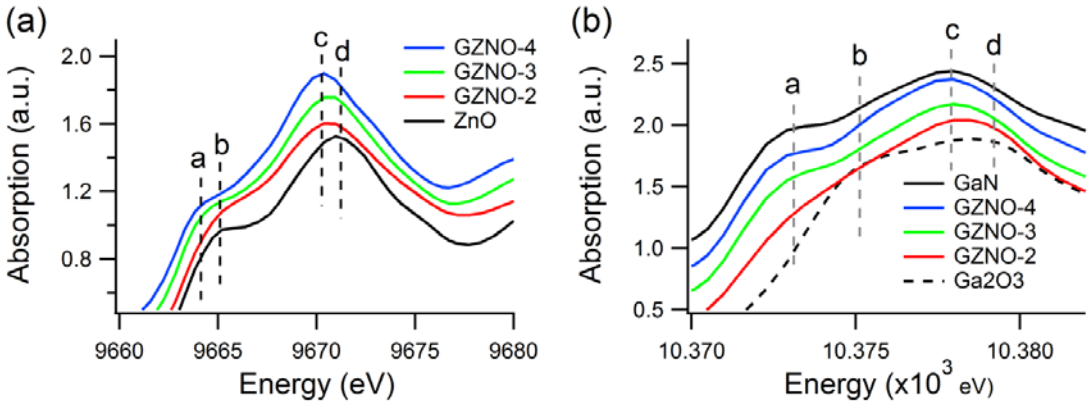

Figure 5-4 Near-edge region of: (a) zinc *K*-edge of GZNO-2, 3, 4 and ZnO; (b) gallium *K*-edge of GZNO-2, 3, 4, GaN, and Ga_2O_3.

The same effect is also observed in the second feature at the Zn *K*-edge (see Figure 5-3(a) vertical dashed lines **c** and **d**). Qualitatively this can be explained as a multiple-scattering (MS) effect since the position of multiple-scattering peaks relative to the excitation threshold has an inverse relationship with the square of the interatomic distance of the absorber, for example, Zn-O in the first coordination shell [27]. This suggests that the local environment around zinc is slightly expanded upon solid solution formation, and that this effect is intensified as the ratio of Zn/(Zn + Ga) decreases. If we take a closer look at the Ga *K*-edge (Figure 5-4(b) vertical dashed lines **a** and **c**) we can see that the first two features in the near edge region do not exhibit the same energy shift observed at the Zn *K*-edge. Since all of the solid solutions in our study are GaN rich, and the shift in energy of the ZnO near edge features becomes larger with an increase in the GaN component, it is plausible that this effect is related to an increase in strain on the ZnO phase of the solid-solution. We can, however, clearly see a distortion in the near edge

region of the Ga *K*-edge spectra of GZNO-2 which might be caused by the presence of an additional β-Ga_2O_3 phase (see Figure 5-4(b) vertical dashed lines **b** and **d**). We do not observe any evidence for a Ga_2O_3 phase in the XRD pattern of GZNO-2, but, this may be due to the detection limit of ~5 % for XRD. In order to measure the effect of GaN and β-Ga_2O_3 contributions to the Ga *K*-edge XANES spectrum of GZNO-2 we attempted to fit the absorption coefficient $\mu(E)$ with a linear combination of α-GaN and β-Ga_2O_3 reference spectra according to Equation 5-1.

$$\mu(E) = a_\mu \cdot \mu(E)_{Ga_2O_3} + b_\mu \cdot \mu(E)_{GaN} \qquad \text{Equation 5-1}$$

Where E is the X-ray excitation energy and a_μ and b_μ are the weighting factors of β-Ga_2O_3 and α-GaN respectively. Figure 5-5 shows the linear combination fit of GZNO-2, including the GaN- and Ga_2O_3-contributions of the reference spectra and the residual; it is clear that absorption coefficient $\mu(E)$ of GZNO-2 cannot be fit using only gallium nitride and gallium oxide as reference standards.

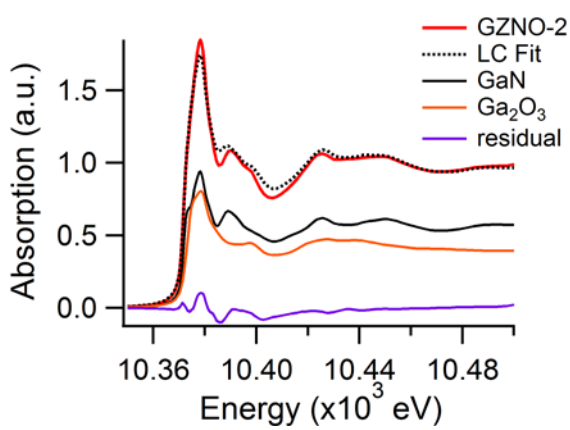

Figure 5-5 Linear combination fitting of GZNO-2 at the Ga *K*-edge using GaN and Ga_2O_3 as fitting standards.

Since we observe a Zn *K*-edge spectrum that is consistent with ZnO, and we cannot fit the Ga *K*-edge using only a combination of β-Ga_2O_3 and α-GaN it is clear that there is another absorber environment for gallium. It is thus likely that some of the gallium in GZNO-2 exists in the form of spinel $ZnGa_2O_4$ since the presence of this phase is observed

for GZNO nanocrystals synthesized at temperatures lower than 650 ℃ [20]. Although GZNO-2 appears to exhibit a single wurtzite phase from the XRD pattern (see Figure 5-1(d)) with no additional diffraction peaks from a cubic $ZnGa_2O_4$ phase, it is still possible that spinel $ZnGa_2O_4$ is present in reasonable amounts since, as previously mentioned, the lower detection limit for XRD is ~ 5%. Previous XANES studies of GZNO solid solutions synthesized at low nitridation temperature have demonstrated that these materials exhibit a spinel structure, and that the Ga *K*-edge XANES is consistent with that of spinel $ZnGa_2O_4$ [28]. Thus it is possible that our low temperature sample, GZNO-2, contains a small amount of spinel $ZnGa_2O_4$.

5.3.3 Zinc and Gallium *K*-edge EXAFS

The gallium *K*-edge EXAFS are displayed in Figure 5-6(a) and (b). In wurtzite GaN the first coordination shell (Ga-N) contains four nitrogen atoms and the second coordination shell (Ga-Ga) contains twelve gallium atoms. In the formation of a GZNO solid solution we would expect that the first coordination shell in would have N(O) nearest neighbours and the second coordination shell would have Ga(Zn) nearest neighbours in a wurtzite-type structure. Some direct experimental evidence for the substitution of O for N to form regular $(Ga,Zn)(N,O)_4$ tetrahedra in a wurtzite-type structure has been provided Yashima et al. using neutron diffraction [5]. If we look at the k^3-weighted Ga *K*-edge EXAFS (Figure 5-6(a)), which emphasizes the second (Ga-Ga(Zn)) coordination shell (see Chapter 2, Section 2.2.2 for an explanation of *k*-weighting), we can clearly see that for GZNO-4, synthesized at 850 ℃, gallium exists in a Ga-N coordination environment. For both GZNO-2 and GZNO-3 we observe a decrease in the FT amplitude of the EXAFS of the second shell at ~2.9 Å, and hence a decrease in Ga(Zn) coordination, which suggests that at lower nitridation temperatures there is a decrease in long-range order. The *k*-weighted Ga *K*-edge EXAFS, which emphasizes the first (Ga-N(O)) coordination shell at ~1.6 Å, is shown in Figure 5-6(b). The first coordination shell exhibits minimal decrease in amplitude compared with the second shell as a function of decreasing nitridation temperature. This suggests that the first coordination shell is less sensitive to the effects of nitridation temperature than the second coordination shell in the formation of the GaN phase of the solid-solution. This is consistent with theoretical work by Li et al. which

predicted a disordered phase with strong short-range order for GaN-ZnO solid solutions [29].

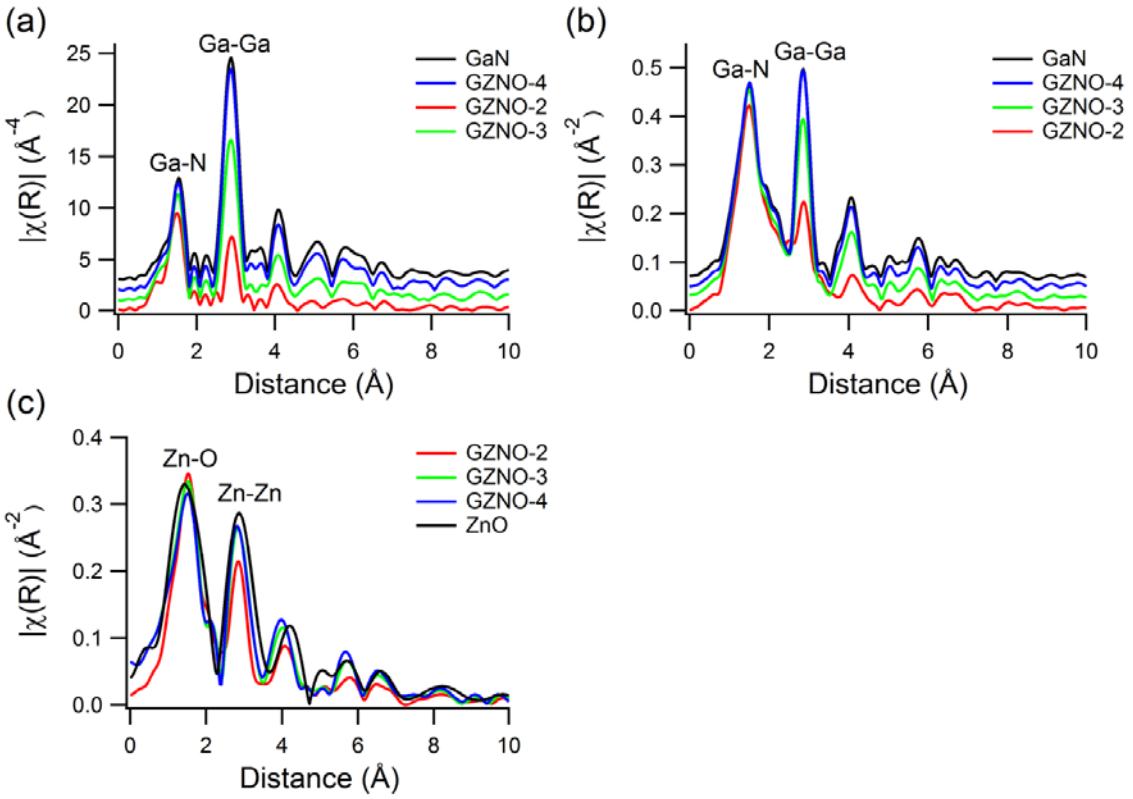

Figure 5-6 Gallium *K*-edge EXAFS of GZNO-2, 3, 4, and GaN (not phase-shift corrected): (a) k^3-weighted to emphasize second (Ga-Ga) coordination shell; (b) *k*-weighted to emphasize first (Ga-N) coordination shell; (c) Zinc *K*-edge EXAFS *k*-weighted to emphasize first (Zn-O) coordination shell (not phase-shift corrected).

Alternatively the reduction in amplitude of the second shell could be due to an increase in Zn content going from GZNO-4 to GZNO-2, causing more chemical disorder in the resultant solid solution. The *k*-weighted zinc *K*-edge EXAFS is displayed in Figure 5-6(c). In wurtzite ZnO the first coordination shell contains four oxygen atoms and the second coordination shell contains twelve zinc atoms. Thus in the formation of a GZNO solid solution we would expect that in the ZnO phase the first coordination shell would have O(N) nearest neighbours and the second coordination shell would have Zn(Ga)

nearest neighbours. Compared to Ga atoms, which only experience a strong distortion in the second coordination shell, Zn atoms see distortion in the first, second, and possibly third coordination shells. The amplitude of the first coordination shell (Zn-O(N)) is relatively insensitive to the change in nitridation temperature, with a slight decrease going from high to low Zn concentration (GZNO-2 to GZNO-4). The amplitude of the second coordination shell (Zn-Zn(Ga)) follows the same trend observed at the Ga *K*-edge with a decrease in intensity vs. the ZnO reference standard for all three samples. The biggest reduction in the amplitude of the second shell at the Zn *K*-edge was observed for GZNO-2, which was nitridated at a temperature of 650 ℃. The first shell interatomic distance increased slightly while the second shell interatomic distance decreased slightly for GZNO-2, 3, and 4. This is consistent with the observation of a red-shift in the MS peak at the Zn *K*-edge (see Figure 5-3(a)), which was attributed to a slightly expanded environment for zinc with a decrease in Zn content in the solid solution and has been previously observed in EXAFS of GZNO solid solutions [26].

5.3.4 Zinc and Gallium $L_{3,2}$-edge XANES

The total electron yield (TEY) Zn and Ga $L_{3,2}$-edge XANES of GZNO-2, 3, and 4 are shown in Figure 5-7(a) and (b) respectively. Since TEY is relatively surface sensitive (~10 nm) we are primarily probing surface and near surface absorber environments for Zn and Ga in the GZNO solid solutions. Since Ga^{3+} and Zn^{2+} are isoelectronic, they should exhibit very similar XANES if they are in the same chemical environment, e.g. Zn in a Ga site of GaN. When Ga^{3+} is replaced by Zn^{2+} charge neutrality must be preserved, this is affected by the substitution of O^{2-} for N^{3-} resulting in chemical disorder within the GaN lattice which is evident in the near-edge spectra at both the Zn and Ga L_3-edges (Figure 5-7(a) and(b)). The Ga and Zn L_3-edges involve dipole allowed electronic transitions from 2p→(4d,4s), and thus in a GZNO solid solution we would expect that as the ratio of Zn/Ga changes we would observe a change in the amount of distortion in the respective (Zn and Ga) absorption spectra. The distortion in the near-edge is a function disorder of the local chemical environment upon alloying despite identical crystal structure. The distortion arises from (i) static disorder resulting from substitution in the first and second shell of the absorbing atom; e.g. substitution of O by N will not only

change the inter-atomic distance between the absorbing atom and the backscatterer, but the back scattering amplitude as well, and (ii) dynamic disorder due to the Debye-Waller term (the root mean inter-atomic displacement), which will also vary. Thus for an isoelectronic absorber with a similar ligand and the same crystal structure, the effect on the XANES is a small shift and broadening of all the resonances.

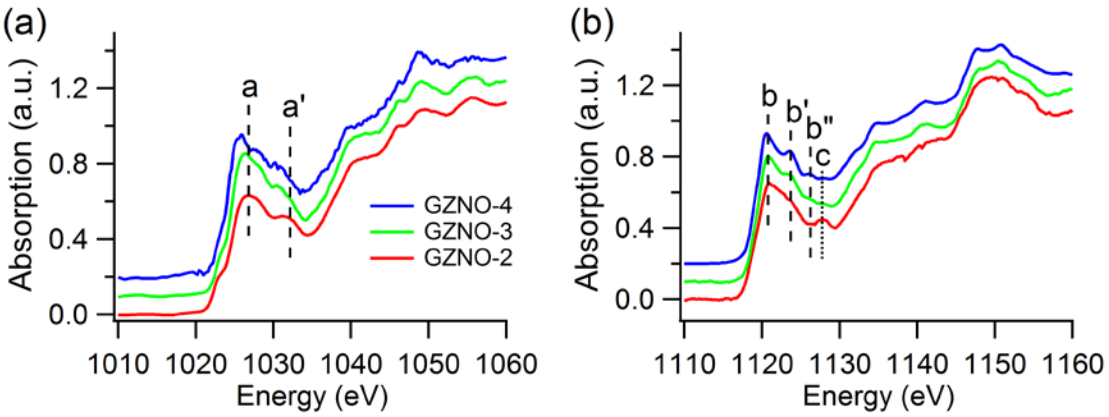

Figure 5-7 (a) Zn and (b) Ga $L_{3,2}$-edge XANES of GZNO-2, 3, and 4 (normalized to unit edge jump).

Initial inspection of the Zn L_3-edge (Figure 5-7(a)) shows an increase in distortion of ZnO multiple-scattering (MS) features (vertical dashed lines a and a') going from high to low Zn concentration, from GZNO-2 to GZNO-4, with the appearance of new MS features. Additionally, there appears to be a red-shift in the position of the MS peaks as the Zn content decreases, which is consistent with the red-shift in MS peaks observed at the Zn *K*-edge and the slight increase in Zn-O interatomic distance observed in the Zn *K*-edge EXAFS. At the Ga L_3-edge (Figure 5-7(b)) we observe an increase in distortion of the MS features (labeled b, b', and b") with a decrease in nitridation temperature and the resultant increase in Zn content. An additional MS feature was observed at the Ga L_3-edge for GZNO-2 (see Figure 5-7(b) vertical dotted line c). In order to study the effect of increasing the ZnO content (and thus the degree of Zn and O doping in the GaN lattice) the excitation threshold energy, E_0, of the Zn and Ga L_3-edge was calibrated to 0 eV for

GZNO-2, 3, and 4 (Figure 5-8(a), (b), and (c) respectively). By setting E_0 to zero for the respective zinc and gallium *L*-edges it is possible to see if the distortion in the MS peaks is due to the substitution of Zn for Ga (or Ga for Zn) in the wurtzite structure. Figure 5-8(a) shows the Zn and Ga L_3-edges of GZNO-2 with E_0 referenced to 0 eV. We observe what appears to be distortion of the MS peaks at both the Zn and Ga L_3-edges for GZNO-2: (1) at the Zn edge a weak shoulder contribution at ~2.7 eV (Figure 5-8(a) peak **I**) and a stronger MS contribution at ~5.9 eV (Figure 5-8(a) peak **II**) which we can tentatively attribute to Ga absorbers in a ZnO structure; (2) at the Ga L_3-edge a new MS feature appears at ~9.7 eV which can be attributed to Zn absorbers in the GaN structure.

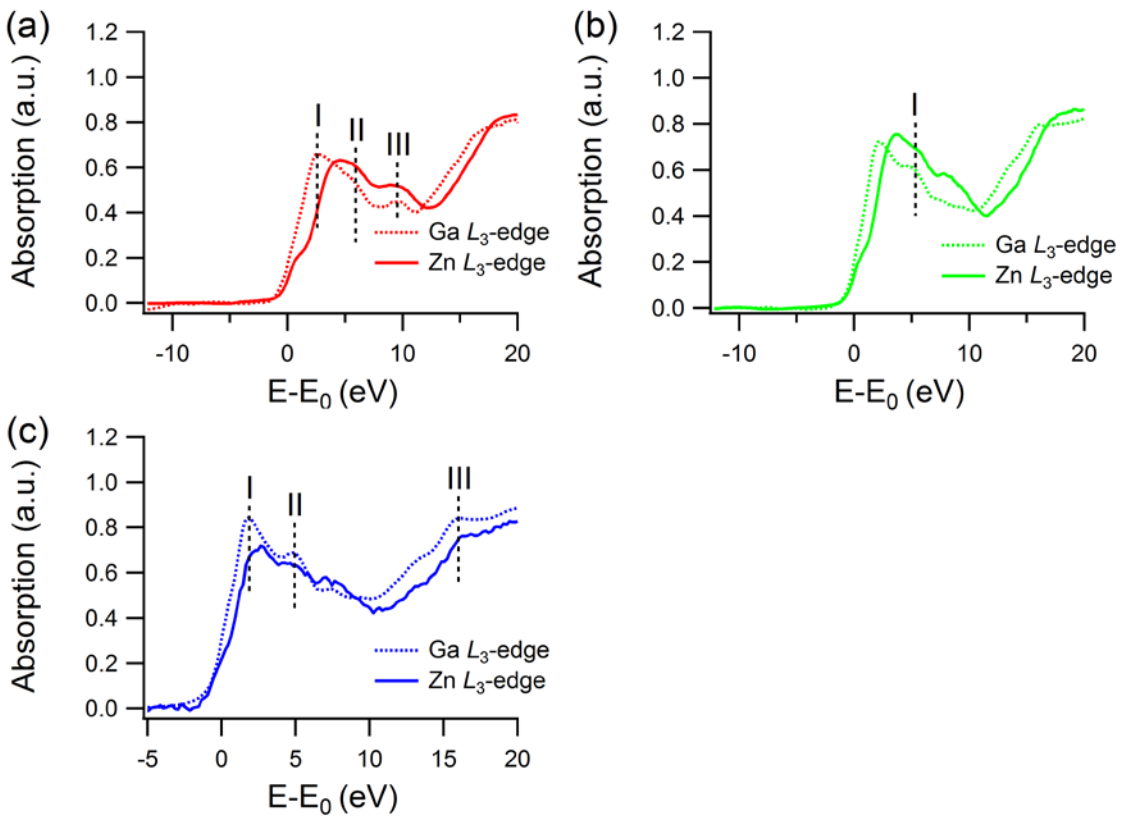

Figure 5-8 Zn and Ga L_3-edge XANES of (a) GZNO-2, (b) GZNO-3, and (c) GZNO-4 (E_0 set to 0 eV).

The Zn and Ga L_3-edges of GZNO-3 are displayed in Figure 5-8(b) with E_0 set to 0 eV. There appears to be only minor distortion in the MS peak of ZnO at ~5.3 eV (Figure 5-8(b) vertical dashed line **I**) which we assign to contributions from Ga absorbers in the ZnO lattice. Thus it appears that at intermediate GaN rich compositions of GZNO, i.e. GZNO-3 ($x \approx 0.379$), there is less distortion of the MS peaks at Zn and Ga L_3-edges. Figure 5-8(c) shows the Zn and Ga L_3-edges of GZNO-4 with E_0 referenced to 0 eV. The signal from the Zn L_3-edge is weak and noisy due to the very small ZnO component in the sample ($x \approx 0.088$); however, it is still clear that there is distortion in the MS region due to GZNO solid solution formation. We observe strong distortion of the MS peaks at the Zn L_3-edges for GZNO-4; a strong shoulder contribution in the first MS peak of ZnO at ~1.8 eV (Figure 5-8(c) peak I), a new MS peak at ~4.9 eV (Figure 5-8(c) peak II), and an alignment of the MS peak at ~16 eV (which differs from both GZNO-2 and 3) which we tentatively assign to Ga absorbers in a ZnO lattice. It is clear from our analysis that at both high and low Zn content, i.e. for GZNO-2 and 4 respectively, there is considerable distortion in the Zn and Ga L_3-edges of our GaN rich GZNO solid solutions. Why at intermediate Zn concentration (i.e. for GZNO-3) the GZNO solid solution does not exhibit as much distortion at the Zn and Ga L_3-edges is currently unclear.

5.3.5 Nitrogen and Oxygen *K*-edge XANES

The total electron yield (TEY) nitrogen and oxygen *K*-edge XANES of GZNO-2, 3, and 4 are shown in Figure 5-9(a) and (b) respectively. Since TEY is surface sensitive (~10 nm) we are probing near surface N and O absorber environments in the GZNO solid solutions. Nitrogen and oxygen *K*-edge XANES involves dipole allowed transitions from N and O 1s→2p, which probes partial unoccupied density of states of N and O 2p character respectively in the conduction band of GZNO solid solutions. It is clear that an increase in nitridation temperature causes a concomitant sharpening of all spectral features at the N *K*-edge (Figure 5-9(a)) indicating an increase in crystalinity going from GZNO-2 to GZNO-4. It is also possible that the distortion we observe in the MS peaks at the N *K*-edge is due to O doping into the GaN lattice as has been previously observed by Tran et al. [30], in oxygen-rich GaN thin films. We do not, however, observe any change in the position of MS peaks at the N *K*-edge across the synthesis temperature range (650

– 850 °C). Closer examination of the near-edge region shows N *K*-edge absorption features consistent with those of GaN [31,32], with peaks at ~401 and 405.8 eV (see Figure 5-9(c) a and a") corresponding to N 1s→s+p_z transitions and peak at ~403.6 eV (see Figure 5-9(c) a') corresponding to N 1s→p_x+p_y transitions [33].

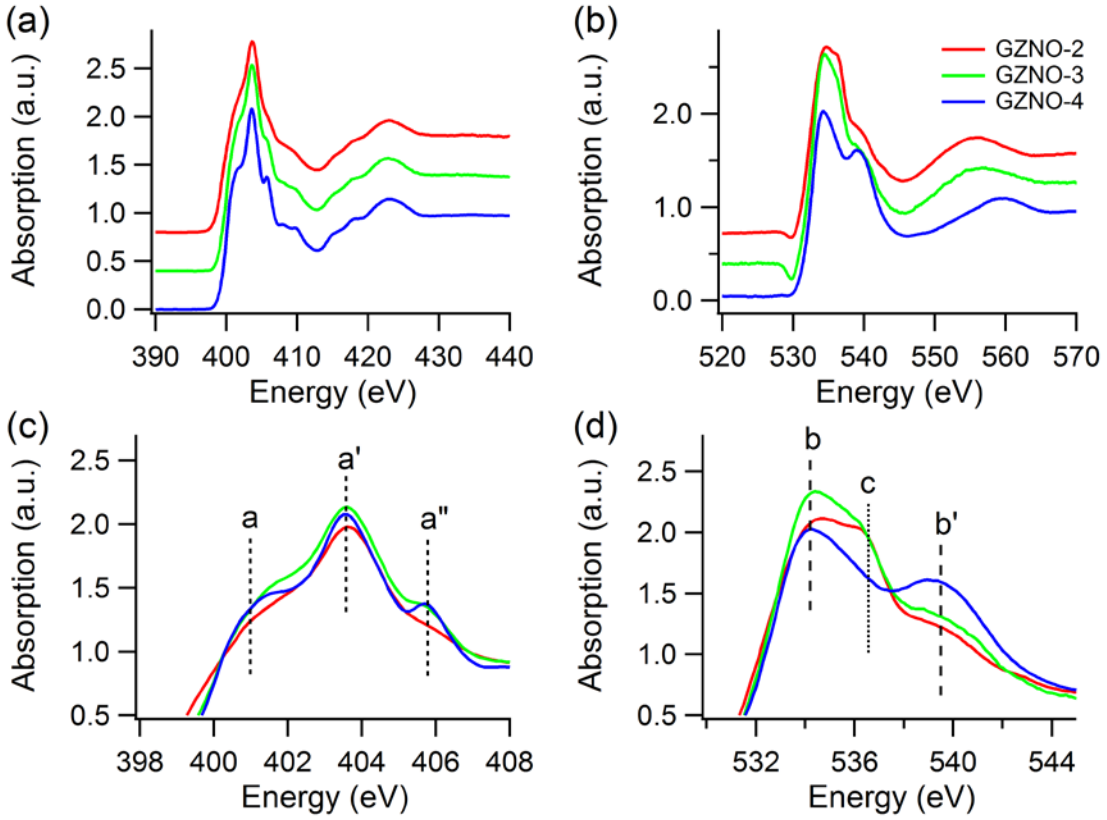

Figure 5-9 (a) Nitrogen and (b) oxygen *K*-edge XANES of GZNO-2, 3, and 4. Near-edge region of (a) nitrogen and (d) oxygen *K*-edge of GZNO-2, 3, and 4. All spectra are normalized to unit edge jump.

At the oxygen *K*-edge we observe a strong dependence on synthesis temperature in the MS features observed (Figure 5-9(b)). Figure 5-9(d) shows the near-edge region of the O *K*-edge with peaks at ~534.2 eV and ~539.5 eV (Figure 5-9(d) b and b") which are present in all three GZNO samples and can be assigned to oxygen atoms in a β-Ga_2O_3 phase [34]. In comparison the peak at ~536.6 eV (Figure 5-9(d) c) is only observed in samples GZNO-2 and 3, and can be attributed to O atoms in a ZnO phase [35]. At the O

K-edge as the nitridation temperature is decreased going from GZNO-4 to GZNO-2: (1) there is a decrease in the intensity of the b and b" peaks assigned to β-Ga_2O_3; (2) a new peak c, assigned to ZnO, is observed for GZNO-2 and 3; (3) and there is an increase in the intensity of the c peak. It appears that at high nitridation synthesis temperatures, e.g. GZNO-4, the surface / near surface environment for oxygen is β-Ga_2O_3. As nitridation temperature decreases oxygen exists in both β-Ga_2O_3 and ZnO absorber environments. Previous XPS studies of GZNO solid solutions have suggested that surface oxygen species exist around both Zn and Ga atoms and that the surface O/Ga ratio increases with increased nitridation time, whereas the bulk O concentration (estimated by EDX) decreases with a decrease in nitridation time associated with the decrease in both surface and bulk zinc concentration due to Zn(s) volatilization [4]. From our N and O *K*-edge XANES analysis it appears that these effects hold for changes in the nitridation temperature; as nitridation temperature increases we observe an increase in near surface O/Ga and a decrease in near surface Zn which results in the formation of a β-Ga_2O_3 surface oxide at high temperature and a loss of surface ZnO phase.

5.3.6 XEOL

X-ray excited optical luminescence (XEOL) of GZNO-2, 3, and 4 was measured using excitation energies below, at resonance, and above the N and O *K*-edges and the Zn and Ga $L_{3,2}$-edges (not shown). Since there was no observable energy dependence on the position of the wavelength of maximum emission (λ_{max}) or the appearance of new emission bands at different excitation energies the XEOL of GZNO-2, 3, and 4 is shown in Figure 5-10(a), collected using an X-ray excitation energy of 580 eV (above the O *K*-edge). GZNO-2 exhibits a broad emission band with a λ_{max} at ~1.90 eV (fit with a single Gaussian) with a FWHM of 0.57 eV and GZNO-3 exhibits a broad emission band at ~1.95 eV (fit with a single Gaussian) with a FWHM of 0.62 eV. GZNO-4 exhibits a broad emission band at λ_{max} ~1.77 eV with a FWHM of 0.50 eV, and a broad shoulder on the high energy side at λ_{max} ~2.12 eV with FWHM of 0.74 eV (fit with two Gaussians).

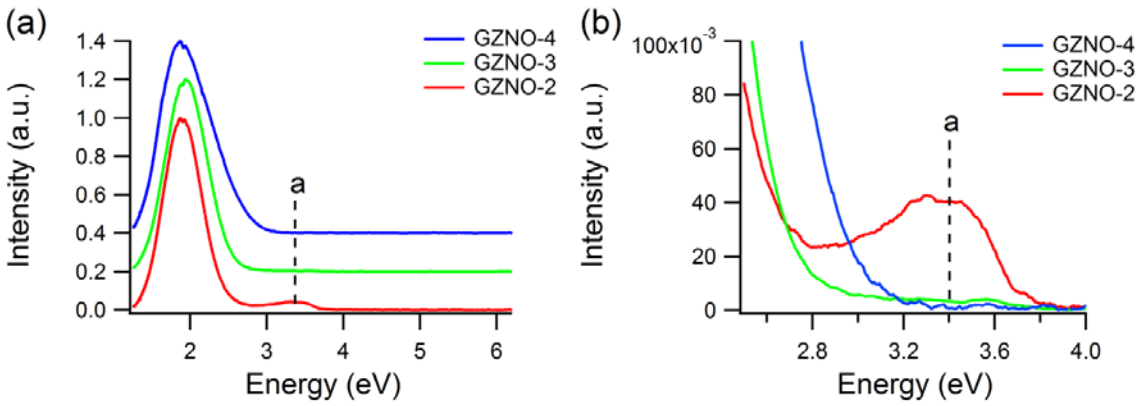

Figure 5-10 (a) XEOL of GZNO-2, 3, and 4 excited with 580 eV X-rays (above O *K*-edge). (b) Expanded view of NBG emission from ZnO phase in GZNO-2. All spectra are normalized to unit intensity.

The XEOL emission bands observed for GZNO-2, 3, and 4 appear at energies too low to be from the optical band-gap (BG) in the materials (the BG was estimated by UV-Vis diffuse reflectance to be 2.21, 2.37, and 2.65 eV for GZNO-2, 3, and 4 respectively, see Figure 5-2). Broad photoluminescence (PL) emission bands have previously been observed for GaN-rich GZNO solid solutions in the range of ~500 – 650 nm (~2.5 – 1.9 eV) with the value of *x* (or ZnO concentration) ranging from ~0.05 – 0.20, with a red-shift in the emission band associated with an increase in *x* [5,36,37]. It has been suggested that these bands are due to the recombination of electrons on O donor levels below the conduction band minimum with holes bound to Zn-related acceptor level sub-bands located above the valence band maximum of the GZNO solid solution, and that with an increase in ZnO concentration (or *x*) an increase in the concentration of lower energy Zn-acceptor levels give a dominant contribution to PL band explaining the observation of a red-shift in the PL [36]. Yoshida et al. suggest that PL emission observed from GZNO solid solutions could be assigned to two overlapping broad emission bands at ca. 650 and 480 nm due to radiative recombination of electron-hole pairs with electrons on O donors below the conduction band and holes on native Ga vacancies for the 650 nm band and holes on Zn acceptor levels for the 480 nm band respectively [38]. Thus the red-shift observed in the PL band with an increase in *x* can be explained as reflecting an increase in the energy distribution of the Zn acceptor levels

which widens with increasing Zn concentration. A broad XEOL emission band at ~2.0 eV (620 nm) was observed by Han et al. from GZNO nanocrystals with $x \approx 0.25$ [39]. Qualitatively, our XEOL results are consistent with these findings as we observe emission bands at 1.90 eV (650 nm), 1.95 eV (636 nm), and 2.12 eV (580 nm) for GZNO-2, 3, and 4 respectively.

The XEOL emission band at ~1.77 eV (700 nm) observed from GZNO-4 has not, however, been observed in previous PL studies of GZNO solid solutions. Broad red XEOL emission bands at ~1.78 eV have been reported for β-Ga_2O_3 nanostructures [40], and have been assigned to the electron-hole pair recombination of a deeply trapped electron on an oxygen vacancy donor state with a deeply trapped hole on a gallium vacancy acceptor state. It is thus likely that the red emission band we observe at ~1.77 eV originates from the β-Ga_2O_3 surface oxide layer on GZNO-4, which would be consistent with the strong TEY O *K*-edge XANES signal that was attributed to β-Ga_2O_3 (see Figure 5-9(c) and discussion that follows). An expanded view (from 2.65 – 4 eV) of the XEOL emission spectrum for GZNO-2, 3, and 4 is shown in Figure 5-10(b). We observe a weak emission band centered at ~3.5 eV for GZNO-2 (Figure 5-10(b) vertical dashed line a) which is too high in energy to be from the optical band-gap of the GZNO solid solution (BG energy ~2.21 eV). We tentatively attribute this peak to the formation of either a pure ZnO or GaN phase in GZNO-2 that does not belong to the bulk GZNO chemical environment. It is likely that at low nitridation temperature there is incomplete conversion to the wurtzite GZNO solid solution phase. Future work is needed to identify whether it is a GaN or ZnO phase (or both) that is responsible for this emission band.

5.4 Conclusion

The effect of nitridation temperature on the synthesis of GZNO solid solution nanocrystals was studied using XAFS and XEOL. From zinc and gallium *K*-edge XANES it was determined that a decrease in nitridation temperature causes a decrease in crystallinity of the resultant GZNO solid solution. A progressive red-shift was observed in the position of the multiple-scattering (MS) peaks at the Zn *K*-edge for GZNO-2, 3, and 4, which was tentatively attributed to a slightly expanded local environment around

zinc upon formation of the GZNO solid solution. The same MS effect was not observed at the Ga *K*-edge suggesting that the ZnO phase exists in a GaN host which is plausible since GZNO-2, 3, and 4 are all GaN rich GZNO solid solutions. A strong decrease in amplitude was observed in the EXAFS of the second coordination shell (Zn-Zn(Ga) and Ga-Ga(Zn)) but not the first coordination shell (Zn-O(N) and Ga-N(O)) at the zinc and gallium *K*-edges suggesting a disordered solid solution with strong short range order. Strong distortions in the zinc and gallium $L_{3,2}$-edge XANES were observed and which was tentatively attributed to Ga absorbers in the ZnO lattice and Zn absorbers in the Ga lattice respectively. This strong distortion in the near-edge region of the Zn and Ga $L_{3,2}$-edges was interpreted as indicative of solid solution formation.

The local environment of nitrogen and oxygen in the surface and near-surface region of the GZNO nanocrystals was examined using total electron yield (TEY) N and O *K*-edge XANES. Features consistent with β-Ga_2O_3 were observed in the near-edge region of the oxygen *K*-edge for all three samples. A new feature was observed in the near-edge region of GZNO-2 and GZNO-3, which increased in intensity with decreasing nitridation temperature, and was assigned to O atoms in a ZnO phase. These findings suggest that as nitridation temperature is increased there is an increase in the concentration of near surface O/Ga atoms and a decrease in near surface Zn atoms which results in the formation of β-Ga_2O_3 surface oxide and the loss of ZnO surface oxide at high synthesis temperature.

XEOL emission bands were observed at ~1.90 eV, 1.95 eV, and 2.12 eV from GZNO-2, 3, and 4 respectively, with an additional emission band at 1.77 eV from GZNO-4. These XEOL emission bands were tentatively assigned to the radiative recombination of electron–hole pairs with electrons on O donors and holes on Zn acceptors in the GZNO solid solution. We observed a red-shift in the XEOL emission with an increase ZnO concentration, and thus an increase in Zn concentration, in the GZNO solid solution. The red-shift can be explained as reflecting a greater energy distribution of Zn acceptor bands with an increase in Zn concentration in the solid solution.

From our study it is clear that using nitridation temperature to control the ZnO content in GZNO solid solutions is not a very tenable process. When the nitridation temperature is reduced there is phase separation resulting in the possibility of additional phase interfaces and boundaries which may result in the formation of electron–hole recombination centers, and thus, a subsequent reduction in the migration of photogenerated carriers for use in surface chemical reactions. Thus it is highly likely that ZnO rich GZNO solid solutions synthesized using nitridation temperature control would exhibit poor photocatalytic activity.

5.5 References

[1] K. Maeda, T. Takata, M. Hara, N. Saito, Y. Inoue, H. Kobayashi, and K. Domen, *J. Am. Chem. Soc.*, **127**, 8286 (2005)

[2] E. Ejder, *Phys. Status Solidi* , **6**, 445 (1971)

[3] V. Srikant, and D. R. Clarke, *J. Appl. Phys.*, **83**, 5447 (1998)

[4] K. Maeda, K. Teramura, T. Takata, M. Hara, N. Saito, K. Toda, Y. Inoue, H. Kobayashi, and K. Domen, *J. Phys. Chem.* B, **109**, 20504 (2005)

[5] M. Yashima, K. Maeda, K. Teramura, T. Takata, and K. Domen, *Chem. Phys. Lett.*, **416**, 225 (2005)

[6] M. Yashima, K. Maeda, K. Teramura, T. Takata, and K. Domen, *Mater. Trans.*, **47**, 295 (2006)

[7] K. Teramura, K. Maeda, T. Saito, T. Takata, N. Saito, Y. Inoue, and K. Domen, *J. Phys. Chem. B*, **109**, 21915 (2005)

[8] K. Maeda, K. Teramura, D. Lu, T. Takata, N. Saito, Y. Inoue, and K. Domen, *Nature*, **440**, 295 (2006)

[9] K. Maeda, K. Teramura, N. Saito, Y. Inoue, and K. Domen, *J. Catal.*, **243**, 303 (2006)

[10] K. Maeda, K. Teramura, D. Lu, T. Takata, N. Saito, Y. Inoue, and K. Domen, *J. Phys. Chem. B*, **110**, 13753 (2006)

[11] K. Maeda, K. Teramura, D. Lu, T. Takata, N. Saito, Y. Inoue, and K. Domen, *J. Phys. Chem. B*, **110**, 13107 (2006)

[12] K. Maeda, K. Teramura, D. Lu, T. Takata, N. Saito, Y. Inoue, and K. Domen, *Angew. Chem. Int. Ed.*, **45**, 7806 (2006)

[13] K. Maeda, K. Teramura, D. Lu, T. Takata, N. Saito, Y. Inoue, and K. Domen, *J. Phys. Chem. C*, **111**, 7554 (2007)

[14] K. Maeda, K. Teramura, D. Lu, and K. Domen, *J. Mater. Chem.*, **18**, 3539 (2008)

[15] K. Maeda, K. Teramura, and K. Domen, *J. Catal.*, **254**, 198 (2008)

[16] K. Maeda, H. Hashiguchi, H. Masuda, R. Abe, and K. Domen, *J. Phys. Chem. C*, **112**, 3447 (2008)

[17] M. Mapa, K. S. Thushara, B. Saha, P. Chakraborty, C. M. Janet, R. P. Viswanath, C. M. Nair, K. V. G. K. Murty, and C. S. Gopinath, *Chem. Mater.*, **21**, 2973 (2009)

[18] J. Wang, B. Huang, Z. Wang, P. Wang, H. Cheng, Z. Zheng, X. Qin, X. Zhang, Y. Dai, and M. H. Whangbo, *J. Mater. Chem.*, **21**, 4562 (2011)

[19] K. Lee, B. M. Tienes, M. B. Wilker, K. J. Schnitzenbaumer, and G. Dukovic, *Nano Lett.*, **12**, 3268 (2012)

[20] W. Han, Z. Liu, and H. Yu, *App. Phys. Lett.*, **96**, 183112 (2010)

[21] X. Chen, S. Shen, L. Guo, and S. S. Mao, *Chem. Rev.*, **110**, 6503 (2010)

[22] A. Kudo, H. Kato, and I. Tsuji, *Chem. Lett.*, **33**, 1534 (2004)

[23] T. Reiger, J. Krochak, T. K. Sham, Y. F. Hu, J. Thompson, and R. I. R. Blyth, Nucl. Instrum. Methods Phys. Res., Sect. A, 582, 93 (2007)

[24] S. M. Heald, D. L. Brewe, E. A. Stern, K. H. Kim, F. C. Brown,; D. T. Jiang, E. D. Crozier, and R. A. Gordon, J. Synchrotron Rad., 6, 347 (1999)

[25] R. D. Shannon, *Acta Crystallogr., Sect. A*, **32**, 751 (1976)

[26] H. Chen, W. Wen, Q. Wang, J. C. Hanson, J. T. Muckerman, E. Fujita, A. I. Frenkel, and J. A. Rodriguez, *J. Phys. Chem. C*, **113**, 3650 (2009)

[27] M. J. Ward, W. Q. Han, and T. K. Sham, *J. Phys. Chem.* C, **115**, 20507 (2011)

[28] V. B. R. Boppana, D. J. Doren, and R. F. Lobo, *J. Mater. Chem.*, **20**, 9787 (2010)

[29] L. Li, J. T. Muckerman, M. S. Hybertsen, and P. B. Allen *Phys. Rev. B*, **83**, 134202 (2011)

[30] N. H. Tran, R. N. Lamb, L. J. Lai, and Y. W. Yang, *J. Phys. Chem. B*, **109**, 18348 (2005)

[31] M. Petravic, P. N. K. Deepnapanray, V. A. Coleman, K. J. Kim, B. Kim, and G. Li, *J. Appl. Phys.*, **95**, 5487 (2004)

[32] T. Kuykendall, P. J. Pauzauskie, Y. F. Zhang, J. Goldberger, D. Sirbuly, J. Denlinger, and P. D. Yang, *Nature Materials*, **3**, 524 (2004)

[33] K. Lawniczak-Jablonska, T. Suski, I. Gorczyca, N. E. Christensen, K. E. Attenkofer, R. C. C. Perera, E. M. Gullikson, J. H. Underwood, D. L. Ederer, and Z. L. Weber, *Phys. Rev. B*, **61**, 16623 (2000)

[34] F. Tourtin, P. Armand, A. Ibanez, G. Tourillon, and E. Philippot, *Thin Solid Films*, **332**, 85 (1998)

[35] V. Vaithianathan, B. T. Lee, C. H. Chang, K. Asokan, and S. S. Kim, *Appl. Phys. Lett.*, **88**, 112103 (2006)

[36] T. Hirai, K. Maeda, M. Yoshida, J. Kubota, S. Ikeda, M. Matsumura, and K. Domen, *J. Phys. Chem.* C, **111**, 18853 (2007)

[37] Y. C. Lee, T. Y. Lin, C. W. Wu, H. Teng, C. C. Hu, S. Y. Hu, and M. D. Yang, *J. Appl. Phys.*, **109**, 073506 (2011)

[38] M. Yoshida, T. Hirai, K. Maeda, N. Saito, J. Kubota, H. Kobayashi, Y. Inoue, and K. Domen, *J. Phys. Chem.* C, **114**, 15510 (2010)

[39] W. Q. Han, M. J. Ward, and T. K. Sham, *J. Phys. Chem.* C, **115**, 3962 (2011)

[40] X. T. Zhou, F. Heigl, J. Y. P. Ko, M. W. Murphy, J. G. Zhou, T. Regier, R. I. R. Blyth, and T. K. Sham, *Phys. Rev. B*, **75**, 125303 (2007)

Chapter 6

6 Time Resolved X-ray Excited Optical Luminescence (TR-XEOL) of $Ga_{1-x}Zn_xN_{1-x}O_x$ Nanoparticles Using an Optical Streak Camera*

6.1 Introduction

The phenomenon of X-ray excited optical luminescence (XEOL) has been around since the discovery of X-rays by Röntgen in 1895, and has commonly been used to "see" X-rays [1]. Despite the increasing popularity of X-ray excited optical luminescence (XEOL) for the study of nano materials, the process has not been fully understood because of both the complexity of the energy transfer process involving the decay of a *core-hole* and subsequent decay cascade dynamics, and its strong dependence on the composition, structure, morphology, size, crystallinity and defects of the scintillation material [2,3]. The advent of third generation light sources has changed this and XEOL is now routinely employed in the study of nano materials [4-7], and is particularly useful for understanding energy transfer in semiconducting nanostructures where the dynamics of band-gap and defect luminescence processes are of great importance [8,9].

In order to further the applications of XEOL we have developed a time-resolved (TR-XEOL) system using an optical streak camera which makes use of the inherent time structure of synchrotron radiation. TR-XEOL is a powerful technique that monitors the temporal behaviour of the emission intensity (decay curve) following absorption of a synchrotron X-ray pulse [8]. TR-XEOL experiments were conducted on the Spherical Grating Monochromator (SGM) beam-line at the Canadian Light Source (CLS) operating in single bunch mode with a 570 ns dark gap, a 35 ps root-mean-square (RMS) electron bunch pulse, and a bunch purity of 10^5 and on the PNC-XSD 20-BM beam-line at the

---

*A portion of this chapter has been accepted for publication: *Journal of Physics: Conference Series*, JPCS113R1 (2012). Published under licence in *Journal of Physics: Conference Series* by IOP Publishing Ltd.

Advanced Photon Source (APS) operating in regular top-up fill mode with a 153 ns dark gap and 33.5 ps RMS electron bunch pulse.

To illustrate the power of this technique we have measured the TR-XEOL of solid-solution nanopowders of gallium nitride – zinc oxide ($Ga_{1-x}Zn_xN_{1-x}O_x$). GaN (E_{gap} = 3.4 eV) and ZnO ($E_{gap} \approx 3.3$ eV) are both wide band-gap semiconductors with wurtzite structures and similar lattice parameters, but, when alloyed together to form a solid solution the resultant material has a band-gap energy less than 3 eV [10,11], and the band-gap narrows with an increase in *x* (or ZnO concentration), falling in the range of ~2.21-2.8 eV (516-442 nm) for *x* = 0.05-0.42 [12-14]. When these solid solutions are investigated with conventional photoluminescence (PL) or XEOL techniques no near-band-gap (NBG) related emission is observable and we only see a broad defect luminescence peak [15-17], which has been previously attributed to oxygen-zinc / donor-acceptor pair (DAP) recombination [18], surface vacancies and defects [19], and a combination of oxygen-gallium and oxygen-zinc DAP recombination [20]. For the first time, however, we have been able to use the temporal resolution of a streak camera, combined with the intense, tunable, and pulsing light from a synchrotron, to directly resolve fast NBG luminescence components in this material. Herein we will discuss the development of our steak camera TR-XEOL technique and its application to the study of these novel materials.

6.2 Part I: Development of Optical Streak Camera TR-XEOL Technique

The TR-XEOL apparatus employs a Hamamatsu C5680 streak camera with a M5677 slow single sweep unit, a Bruker IS200 spectrograph, and a 30 mm WD lens system composed of 1 inch lenses and a sapphire UHV window (Figure 6-1). The streak tube is operated in single sweep mode and is triggered at CLS by a highly stable pulse generated by resynchronization of the orbit clock to the 500 MHz storage ring RF signal. At APS the streak tube is triggered by a bunch clock signal from the APS Ring RF system.

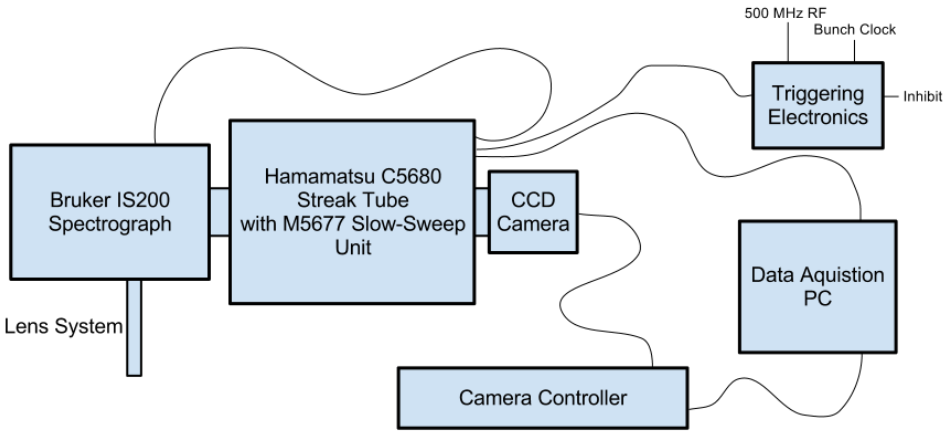

Figure 6-1 Schematic of streak camera TR-XEOL apparatus.

Streak cameras operate by converting a temporal event into a spatial profile, and thus are able to achieve sub-picosecond time resolution. The primary benefit of streak camera based TR-XEOL over other time resolved methods is the ability to simultaneously collect both lifetime decay and emission wavelength data, thus producing a temporally resolved 2D map of the XEOL emission pattern. This 2D temporal mapping capability is achieved by first passing XEOL collected from the sample through a spectrograph to disperse the light across the photocathode of the streak camera. Photoelectrons are subsequently generated at the front of the streak tube with a horizontal profile that is determined by the XEOL spectrum. The streak tube then applies a vertical deflection to the transiting photoelectrons, and thus, the original horizontal XEOL emission pattern is retained at the detector. The resulting 2D map contains XEOL spectral information on the horizontal axis and temporal information on the vertical axis. The ability to differentiate between multiple luminescence decay processes that are occurring with different lifetimes by applying appropriate integration windows (both temporal and spectral) to the resultant streak image is the greatest advantage that this technique provides over other TR-XEOL methods [21].

The M5677 slow sweep unit was chosen for the TR-XEOL apparatus due to the specified resolution of 50 ps, which makes it an ideal match for the pulse duration of 35

ps at CLS. Due to the large reduction in ring current at CLS while operating in single bunch mode vs. regular fill-up mode (16 mA vs. 250 mA at injection) the XEOL collected from a single excitation pulse is very weak. In order to overcome the weak XEOL signal data is usually collected in photon counting mode, which produces a final streak image that is a composite of single photon events captured over many (thousands to tens of thousands) individually triggered streak processes. Thus minimizing trigger jitter, which produces a blurring of the streak image in time, is of great importance to achieve a high level of temporal resolution. In order to minimize trigger jitter effects custom in-house triggering electronics were developed with the following features: 1) The streak camera is triggered by resynchronizing the orbit clock to the 500 MHz master oscillator, which produces a highly stable pulse with the same period as a single electron bunch orbiting the storage ring [22]; 2) The streak camera is inhibited during the periodic bunch cleaning; 3) The trigger pulse can be delayed in 2 ns steps to synchronize the timing of the camera with the single bunch in the storage ring.

High bunch purity, the ratio of the amount of charge in the excitation pulse vs. the amount of charge in the dark gap before and after the excitation pulse, is very important for TR-XEOL experiments due to the necessity of having a well-defined excitation pulse. In order to improve bunch purity in the CLS storage ring a transverse feedback (TFB) kicker system was installed, the implementation and testing of which is described elsewhere: An improvement in the bunch purity from 10 to 10^5 was observed resulting in stable excitation pulses with the time structure of a true single bunch [23].

Extensive testing of this system was carried out at CLS and APS [24]. Although the streak camera TR-XEOL apparatus was designed to be fully implemented for routine use on the spherical grating monochromator (SGM) beam-line at CLS during single bunch operation, the ability to run TR experiments during regular top-up mode operations at APS provided highly necessary testing and commissioning time due to the limited number of single bunch shifts available at CLS.

The SGM beam-line at the CLS is a high resolution - high flux undulator based beam-line with an energy range of 250-2000 eV and a resolving power greater than 10^4

below 800 eV [25]. Beam-lines that operate in the soft X-ray regime (~200 – 2000 eV) are particularly suited to this type of experiment for the following reasons: (1) at low excitation energy the quantum efficiency of XEOL is much higher than at high X-ray energy where X-ray fluorescence processes dominate (X-ray can escape the solid without contributing to the secondary process which in turn leads to energy transfer to the luminescence channel); (2) at these energies the X-ray attenuation length (1/*e*) is sufficiently short to allow for probing of surface, interfacial, and bulk regions of the sample; (3) the mean free path for electrons in condensed matter excited using soft X-rays is relatively short, and thus their energy is more readily transferred through inelastic scattering creating shallow holes and low kinetic energy (secondary) electrons; (4) electrons in the K and L shells of many important light emitting semiconducting nanomaterials (ZnO, GaN, Si, etc.) are accessible at these energies.

6.3 Part II: TR-XEOL Study of $Ga_{1-x}Zn_xN_{1-x}O_x$ Nanoparticles

6.3.1 Experimental

A solid solution of gallium nitride – zinc oxide (GZNO) was synthesized as reported previously [16]. Briefly a mixture of gallium nitrate hydrate and zinc acetate dihydrate was dissolved in MEA, stirred at 65 ℃ for 2 h, and aged for 1 week at 0 ℃. The resultant gel-like precursor was put in an alumina boat and inserted into the hot zone of a quartz tube furnace; the precursor was then nitridated with ammonia at 850 ℃ for 10 h. The product was collected from the inner wall of the quartz tube close to the alumina boat.

Preliminary TR-XEOL measurements were carried out at bending magnet based PNC/XSD 20-BM beam-line of the Advanced Photon Source (APS) at Argonne National Laboratory, Argonne IL [26]. APS is a 7.0 GeV third-generation source operating in top-up mode at a ring current of 100 mA. Streak images were recorded on a Hamamatsu C5680 streak camera with a M5677 slow single sweep unit and a Bruker IS200 spectrograph. The streak slits were set at 100 μm and the spectrometer slits were set fully open. The streak camera was triggered using the bunch clock signal from the APS Ring RF system. A sweep time of 20 ns was chosen (determined experimentally) and streak

images were collected using excitation energies below and above the Zn and Ga *K*-edges. Streak images were collected in photon counting mode with an exposure time of 138 ms; each image is a composite of 30000 exposures. Due to the limitations of the experimental set-up at the 20-BM beam-line no instrument response function (IRF) data was recorded.

TR-XEOL measurements were carried out at the undulator based Spherical Grating Monochromator (SGM) beamline of the Canadian Light Source (CLS) at the University of Saskatchewan [25]. CLS is a 2.9 GeV third-generation source operating at 250 mA at injection in regular fill mode and ~16 mA at injection in single-bunch fill mode. A powdered sample of GZNO was applied in a thin uniform layer on carbon tape on a copper sample holder. Streak images were collected using a Hamamatsu C5680 streak camera with a M5677 slow single sweep unit and a Bruker IS200 spectrograph. The streak slits were set at 20 μm and the spectrometer slits were set fully open. The streak tube was triggered at CLS using a highly stable pulse generated by resynchronization of the orbit clock to the 500 MHz storage ring RF signal. TR-XEOL streak images were recorded with a sweep time of 5 ns (determined experimentally) using excitation energies below, at resonance, and above the N and O *K*-edges and Zn and Ga L_3-edges respectively. Streak images were collected in photon counting mode with an exposure time of 34 ms; each image is a composite of 10000 exposures. An IRF streak image was recorded using zero-order light from the SGM beam-line and an Au coated piece of silicon wafer as a mirror.

6.3.2 Results and Discussion

Applying our streak camera based TR-XEOL technique to study the electronic structure of GaN-ZnO solid solutions we have been able to observe several distinct components in the optical emission spectrum by choosing appropriate time windows and slices. For our study we used a well characterized sample of GaN-ZnO solid solution nanoparticles (GZNO) with an approximate composition of $(GaN)_{0.75}(ZnO)_{0.25}$, a particle size of ~40-120 nm, and uniform bulk composition measured with EDS, SEM and total electron yield (TEY) and total fluorescence yield (TFY) X-ray absorption spectroscopy respectively [16]. Initial streak camera measurements of GZNO (not shown) collected at the 20 BM beam-line (APS), taken below and above the Zn and Ga *K*-edges using a 20 ns

sweep time, indicated that there was a fast luminescence emission component at ca. 480 nm, which was not observed previously via conventional un-gated XEOL [16,17].

A XEOL streak image of GZNO collected on the SGM beam-line (CLS) using a 5 ns sweep time with excitation energy of 550 eV is shown in Figure 6-2(a).

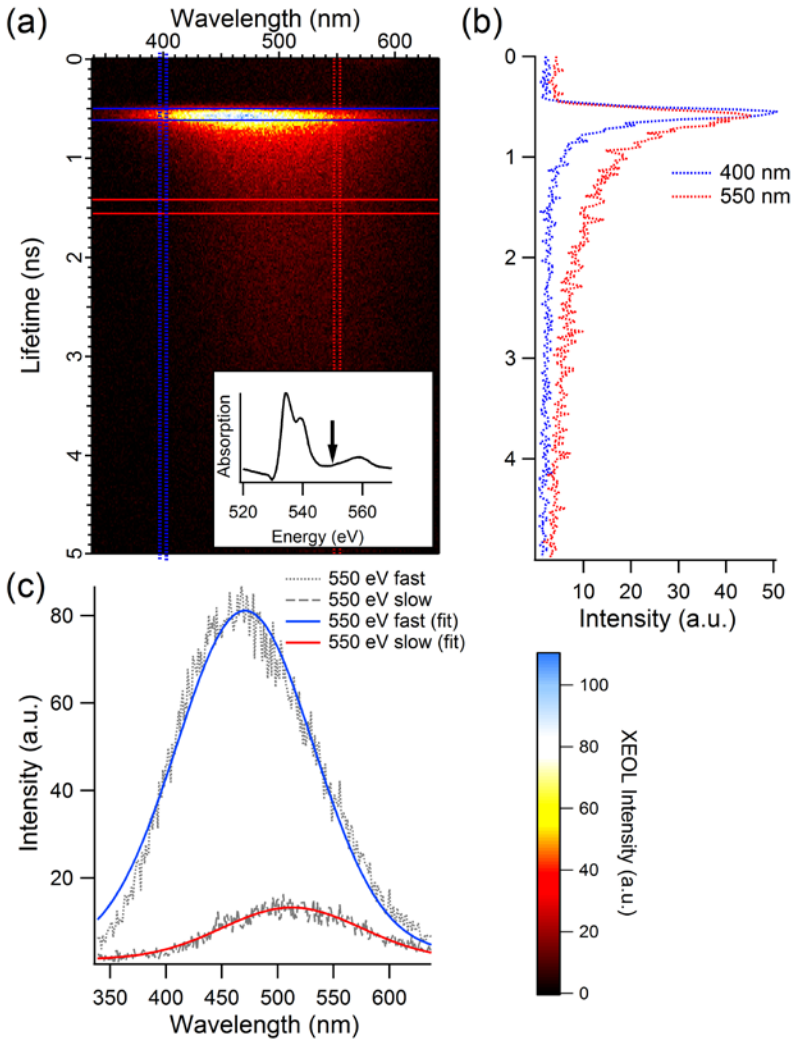

Figure 6-2 (a) 5 ns streak image of XEOL emission (340-640 nm) from GZNO excited at 550 eV (see O *K*-edge XANES inset). (b) XEOL decay lifetime windows taken from blue (400 nm) and red (550 nm) regions of the streak image respectively. (c) Fast and slow XEOL spectral windows taken from 0.5-0.6 ns and 1.45-1.55 ns (both raw data and Gaussian fits are displayed).

By taking a 0.1 ns horizontal slice (Figure 6-2(c), 550 eV fast) of this image from immediately after excitation with a 550 eV X-ray pulse (0.5-0.6 ns) we observe a broad, asymmetric emission band centered at ~471 nm (2.63 eV), with a shoulder on the low energy side. When we take a 0.1 ns slice (Figure 6-2(c), 550 eV slow) ~1 ns after excitation (1.45-1.55 ns) we observe another broad band centered at ~512 nm (2.42 eV). Lifetime decay spectra shown in Figure 6-2(b), taken from the high energy (blue curve) and low energy (red curve) side of the XEOL map respectively, exhibit a shorter luminescence lifetime from the high energy side of the XEOL emission spectrum. Using a phenomenological argument we can interpret this as a shorter lifetime for the 471 nm band vs. the 512 nm band, however, further work must be done to provide quantitative lifetime information. XEOL spectra collected from GZNO using a conventional un-gated apparatus (CLS, SGM beam-line, Ocean Optics QE65000 spectrometer) exhibit a broad, long lifetime, emission band at ca. 620 nm (Figure 6-3) [16].

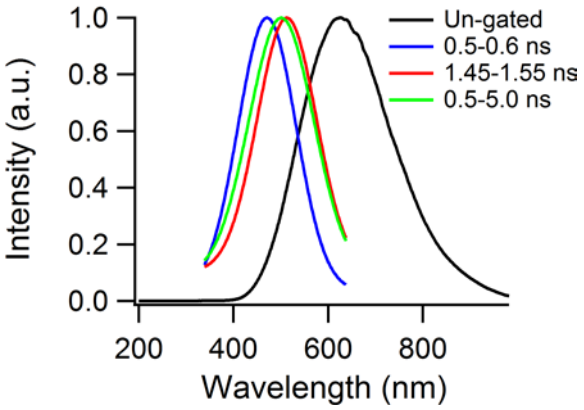

Figure 6-3 XEOL spectra of GZNO, normalized to unity, recorded un-gated and using 0.5-0.6, 1.45-1.55, and 0.5-5.0 ns time windows respectively (Gaussian fit of raw TR data displayed).

In contrast, by employing our streak camera TR-XEOL apparatus with CLS operating in single-bunch mode and applying appropriate time windows, the long lifetime emission band is completely suppressed and we can resolve two bands, one centered at ~471 nm (0.5-0.6 ns slice, Figure 6-3: blue spectra) and one centered at ~512 nm (1.45-

1.55 ns slice, Figure 6-3: red spectra) when the sample is excited with 550 eV X-rays (above O *K*-edge). Integrating over the entire 5 ns window immediately after excitation (0.5-5 ns, Figure 6-3: green spectra), we observe one broad band composed of the 471 nm and 512 nm components, centered at ca. 500 nm (~2.48 eV). The appearance of short wavelength emission in TR-XEOL that is not observed in un-gated XEOL has been previously reported for systems where a significant portion of the photon energy absorbed was transferred to the defect emission channel, which is a relatively slow process [27]. The band-gap for GZNO has been estimated to be ~2.53 eV from UV-vis diffuse reflectance measurements [16], which is in reasonable agreement with the wavelength of maximum emission of ~2.48 eV observed using the 5 ns time window (integrated over the entire window, 0.5-5 ns) to record the TR-XEOL spectra, hence the possibility of two separate NBG emission bands with different decay lifetimes.

Previously the band-gap narrowing observed in these materials has been attributed to p–d repulsion between N 2p and Zn 3d states in the valence-band, which would result in an upward shift of the valence band maximum and a corresponding narrowing of the band-gap [28], and is consistent with the formation a stoichiometric oxy-nitride super lattice. It has also been suggested that this band-gap narrowing is due to strong mixing of 4s and 4p states of Zn and Ga near the conduction band and O and N 2p states in the valence band [29]. Recent theoretical studies have suggested a disordered random-alloy system of ZnO(GaN) in a GaN(ZnO) host containing phase boundaries is a better model for these solid solution oxynitrides, and that the resultant band-gap narrowing within the GaN-ZnO system arises from a decrease in conduction band onset energy (as opposed to an increase in valence band maximum energy) [30,31].

A recent experimental X-ray emission (XES) and absorption (XAS) study by McDermott et al. has suggested that GaN-ZnO solid solutions are best described as an inverted gap heterostructure of GaN and ZnO with two separate optical gaps characteristic of each phase (GaN and ZnO respectively), and that the band-gap narrowing can be attributed to repulsion between empty conduction-band states associated with the distinct phases of the material due to the proximity of these states at the phase interface [32]. Our TR-XEOL results are consistent with these findings lending

further support to a disordered random-alloy as the correct model for GaN-ZnO solid solutions. If the observed low and high energy emission bands are really NBG components of the solid solution then it would be expected that they would be very narrow. One possible explanation for the broadness of these peaks is that the local atomic composition of each nanoparticle is likely not homogeneous as has been previously observed by Maeda and Domen for GaN-ZnO particles [33].

Figure 6-4(a) shows the XEOL collected above the N and O *K*-edges and Zn and Ga L_3-edges using a 0.5–0.6 ns time window.

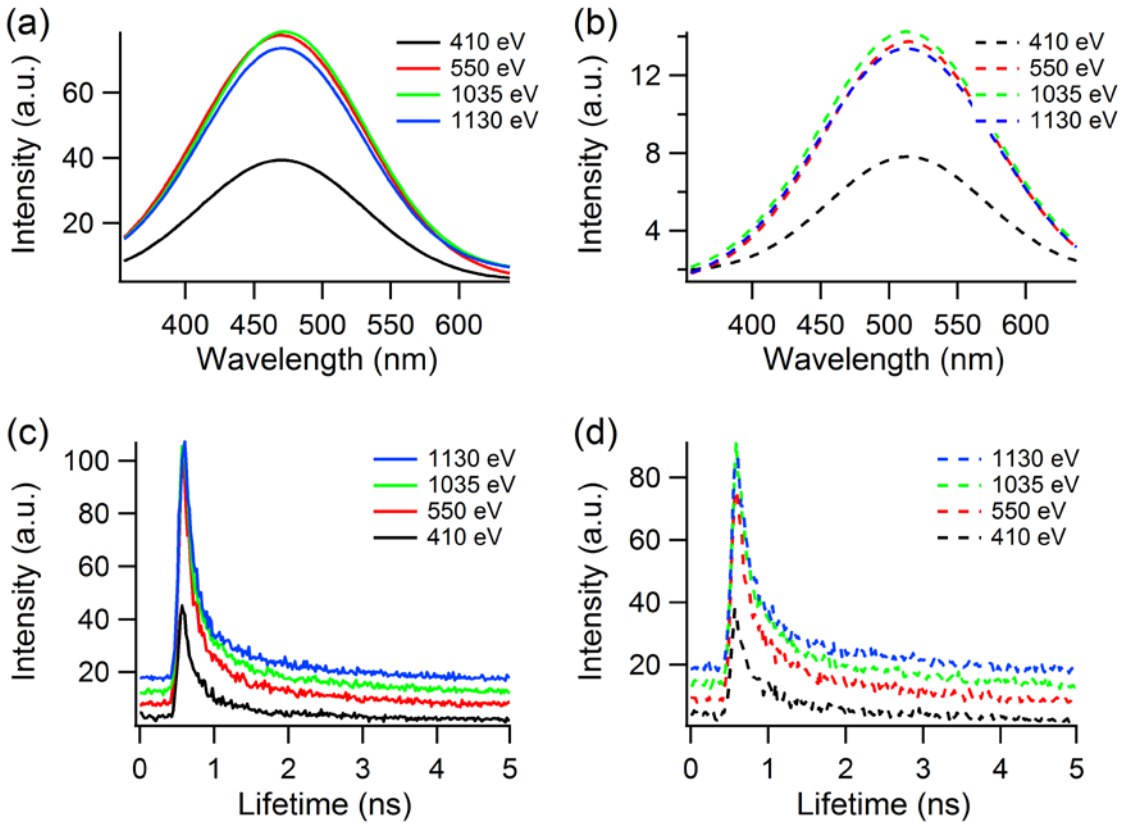

Figure 6-4 TR-XEOL spectra of GZNO collected with excitation energies above the N and O *K*-edges and Zn and Ga L_3-edges using (a) 0.5-0.6 ns and (b) 1.45-1.55 ns time windows respectively (Gaussian fit of raw data displayed). XEOL lifetime decay spectra of GZNO collected with excitation energies above the N and O *K*-edges and Zn and Ga L_3-edges using (c) 466-475 nm and (d) 507-517 nm wavelength windows respectively.

In an attempt to assign the observed NBG components to their respective phases (GaN and ZnO) in the solid solution TR-XEOL measurements were taken below, at resonance, and above the N and O *K*-edges and Zn and Ga L_3-edges. The emission maximum remains constant for all excitation energies at ~471 nm (2.63 eV). The emission intensity of this band increases with the turn-on of the O 1s *core-hole* (550 eV excitation energy) and then remains relatively constant. Figure 6-4(b) shows XEOL collected above the N and O *K*-edges and Zn and Ga L_3-edges using a 1.45–1.55 ns time window. Again the emission maximum remains constant for all excitation energies at ~512 nm (2.42 eV), the emission intensity of this band also increases with the turn-on of the O 1s *core-hole* (550 eV excitation energy) and then remains relatively constant.

Since the two NBG bands appear to be insensitive to the excitation of the different core levels of the chemical species present in the solid solution it is not possible to attribute either emission band to a particular phase of the material based on the XEOL spectra alone. It does appear that both NBG emission bands are sensitive to the turn-on of the O 1s *core-hole*, however, suggesting that the ZnO phase may be responsible for energy absorption in this material. If we turn to the XEOL decay spectra collected using 466–475 nm wavelength window (Figure 6-4(c)) we can see the same effect on the emission intensity. From initial inspection of the spectra there does not appear to be a difference in the decay lifetime as we excite the different core levels within the material. The XEOL decay spectra collected using the 507–517 nm wavelength window (Figure 6-4(d)) show the same trend.

Figure 6-5(a) and (b) show XEOL decay curves collected using integration windows centered at 471 and 512 nm above the O *K*-edge and Ga L_3-edge respectively. In both cases it appears that the luminescence band at ~512 nm (2.42 eV) has a slightly longer decay lifetime then the band centered at ~471 nm (2.63 eV).

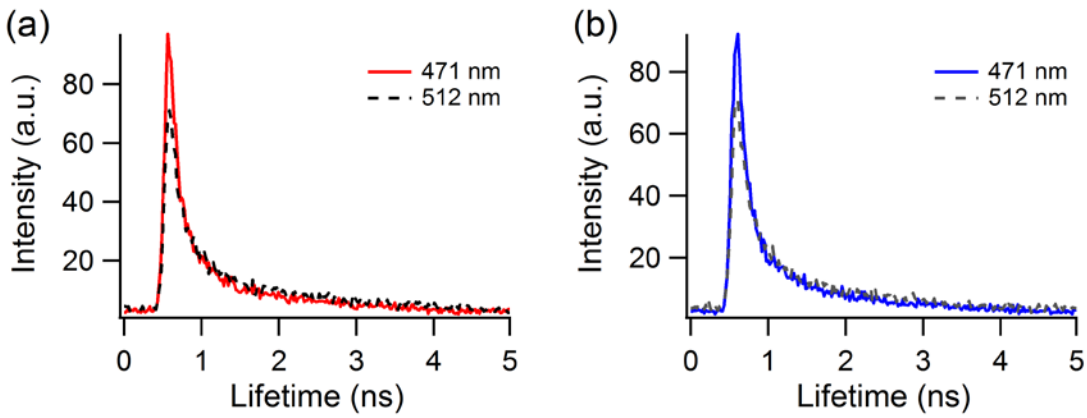

Figure 6-5 XEOL lifetime decay of GZNO collected using an excitation energy of (a) 550 eV (above the O *K*-edge) and (b) 1130 eV (above the Ga L_3-edge) with integration windows centered on the 471 nm (fast) and 512 nm (slow) emission bands.

In order to obtain quantitative lifetime data from the XEOL decay spectra a detailed fitting analysis of the lifetime decay curves collected using 465-475 nm and 505-515 nm wavelength windows was conducted using excitation energies below, at resonance, and above the N and O *K*-edges and Zn and Ga L_3-edges. TR-XEOL decay curves were fit using a double exponential function which was experimentally determined to provide the best fit:

$$I(t) = a_1 \cdot exp\left({}^{-t}/_{\tau_1}\right) + a_2 \cdot exp\left({}^{-t}/_{\tau_2}\right) \tag{6-1}$$

Where a_i represents the amplitudes of the components, t represents time, and τ_i represents the decay lifetime (both components are excited at time $t = t_0$). Equation 6-1 can be generalized as:

$$I(t) = F(t - t_0) = \begin{cases} \sum_{i=1}^{K} a_i \cdot exp[-(t - t_0)/\tau_i] \,; t > t_0 \\ 0 \qquad\qquad\qquad\qquad\qquad\qquad ; t \leq t_0 \end{cases} \tag{6-2}$$

Where $F(t - t_0)$ is the sample's XEOL decay curve. Fitting of TR-XEOL data collected using our optical streak camera must take into account the lifetime of the excitation pulse if accurate decay values are to be obtained. In order to factor in the lifetime of the single-

bunch X-ray pulse generated by the synchrotron an instrument response function (IRF) was collected using zero-order light from the SGM beam-line. The XEOL lifetime decay curve is then convoluted with the IRF according to the following convolution integral:

$$I(t) = L(t) \otimes F(t) \tag{6-3}$$

Where $L(t)$ is the curve of the total IRF (including the synchrotron pulse and all temporal broadening effects of the detection system), $F(t)$ is the sample's decay curve (Equation 6-2), and $I(t)$ is the curve of measured intensity. Thus given the measured intensity curve $I(t)$ and the IRF curve $L(t)$, the sample's decay curve $F(t)$ is recalculated and then fit with the double exponential function (see Equation 6-1). In this way we are able to extract quantitative XEOL decay lifetimes taking into account the width of the synchrotron excitation pulse and any additional broadening contributions from the beam-line, the spectrograph, and the streak camera.

Representative XEOL decay lifetime fitting results collected using excitation energies above the N and O *K*-edges and Zn and Ga L_3-edges are shown in Table 6-1. It is clear from our fitting results that the emission band centered at 471 nm has a shorter lifetime than the emission band centered at 512 nm at all X-ray excitation energies.

Table 6-1 Representative XEOL decay lifetime fitting results for GZNO collected using an excitation energy above the N and O *K*-edges and the Zn and Ga L_3-edges with integration windows centered on the 471 nm (fast) and 512 nm (slow) emission bands.

Excitation Energy (eV)	410		550		1035		1130	
Integration Window (nm)	465 – 475	505 – 515	465 – 475	505 – 515	465 – 475	505 – 515	465 – 475	505 – 515
τ_1 (ns)	0.126	0.162	0.139	0.156	0.121	0.158	0.123	0.160
τ_2 (ns)	1.05	1.20	0.982	1.25	0.850	1.09	0.901	1.13
χ^2	1.13	1.20	1.15	1.16	1.21	1.32	1.24	1.20

The XEOL decay lifetime as a function of excitation energy is shown in Figure 6-6(a) for τ_1 and (b) for τ_2 using integration windows ~centered on the 471 and 512 nm emission bands. From the plot of τ_1 vs. excitation energy it appears that the first decay lifetime component of the 512 nm band is sensitive to N and O 1s→2p (*K*-edge) and Ga $2p_{3/2}$→4s,4d (L_3-edge) *core-hole* creation. Whereas the first decay lifetime component of the 471 nm band appears to be sensitive to O 1s→2p (*K*-edge) and Zn $2p_{3/2}$→4s,4d (L_3-edge) *core-hole* creation. At first this does not seem consistent with the idea that these two bands are NBG components corresponding to GaN and ZnO phases of the material respectively, however, if we consider other XEOL decay processes occurring within the material these observations are not inconsistent with our proposed model for the electronic structure of GZNO. We must recall that in the un-gated XEOL of GZNO there is a broad emission band centered at ~620 nm and although the bulk environment for Ga is GaN, the surface appears to be primarily β-Ga_2O_3 [16,17].

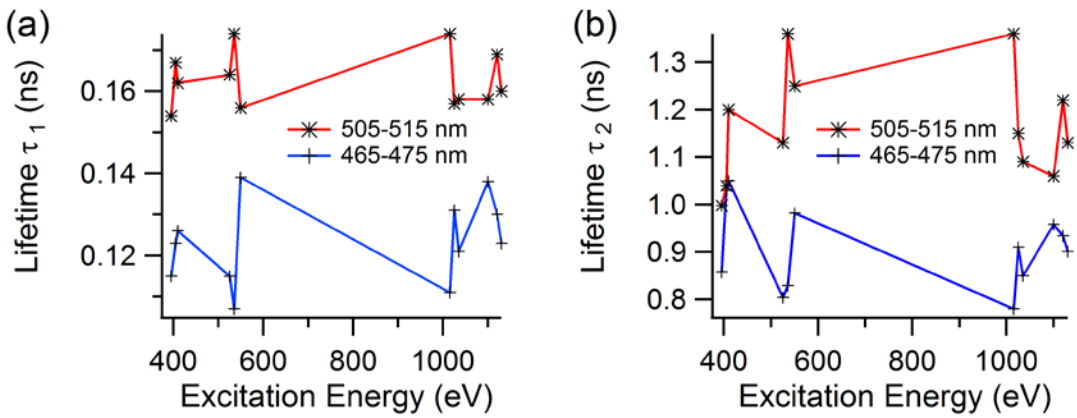

Figure 6-6 XEOL decay lifetimes (a) τ_1 and (b) τ_2 as a function of excitation energy taken below, at resonance, and above the N and O *K*-edges and Zn and Ga L_3-edges using integration windows of 505-515 nm and 465-475 nm.

We can thus use this information to tentatively assign the XEOL emission band at 512 nm to the GaN phase in the solid solution. We justify this assignment because the decay lifetime of this emission band is perturbed by the creation of N and Ga *core-holes*. The sensitivity to the oxygen *K*-edge at first appears inconsistent with our assignment of this emission band; however, we can imagine the possibility of energy transfer from de-excitation of the β-Ga_2O_3 surface oxide into the GaN phase in an intersystem crossing.

If we focus on the 471 nm emission band we observe a decrease in decay lifetime at resonance at the O *K*-edge and an increase in decay lifetime at resonance at the Zn L_3-edge. We tentatively attribute the band at 471 nm to the ZnO phase within the GZNO solid solution. Examination of the second decay lifetime, τ_2, of the 512 nm emission band (Figure 6-6(b)) lends further support to our initial assignment of this band to the GaN component of the GZNO solid solution. Here we can see that the second decay lifetime of the lower energy emission band is sensitive to O 1s→2p (*K*-edge) and Ga $2p_{3/2}$→4s,4d (L_3-edge) *core-hole* creation suggesting that this decay lifetime is related to the defect emission band from the β-Ga_2O_3 surface oxide. Whereas the second decay lifetime, τ_2, of the 471 nm emission band (Figure 6-6(b)) exhibits the same general trend as the first decay lifetime, τ_1. Previous time-resolved photoluminescence (TR-PL)

measurements by Lee et al. of a GaN-ZnO solid solution with x = 0.22, which is close to the x value of our GZNO sample (x = 0.25) have been taken at the wavelength of maximum emission of the defect luminescence band at 663 nm (1.87 eV) [34]. The TR-PL measurements gave a decay lifetime of τ =1.24 ns fit using a stretched exponential function. This value is in good general agreement with the values we observe for τ_2 around the O K and Ga L_3 edges which range from ~1.1–1.4 ns. Since Lee and co-workers only studied the TR-PL at one emission wavelength it is not possible to know if the TR-PL profile would have resembled ours with a suppression of the defect emission band and resolution of the NBG luminescence components. Our results do, however, suggest that the second decay lifetime of the 512 nm emission band likely originates from the β-Ga_2O_3 defect emission decay channel.

6.4 Conclusions

A time-resolved X-ray excited optical luminescence apparatus employing an optical streak camera has been developed and tested at CLS and APS, and successfully integrated into the SGM beam-line (CLS) for regular operation during single-bunch fill operation mode. Applying this new TR-XEOL technique to study the electronic structure of GaN-ZnO solid solution nanoparticles we have been able to temporally resolve several components in the X-ray excited optical emission spectrum. These emission bands at ~ 471 nm (2.63 eV) and ~512 nm (2.48 eV) have been tentatively attributed to ZnO and GaN phases within the GZNO solid solution. Our preliminary assignment of these bands was based on their temporal behavior as a function of excitation energy which was studied below, at resonance, and above the N and O K-edges and Zn and Ga L_3-edges. Our results are consistent with the findings of McDermott et al. [32], who suggest that this system is best described as a solid solution heterostructure of GaN and ZnO phases, and that the band-gap narrowing observed in these materials is a result of repulsion between each phase's conduction band onset due to the proximity of states at the phase interface and not, as has previously been suggested, due to p–d repulsion of N 2p and Zn 3d states in the valence band resulting in an upward shift of the VBM. The second decay lifetime for the 512 nm emission was found to be sensitive to O K and Ga L_3 edge core-hole creation and had decay time of τ ~ 1.1–1.4 ns which is in reasonable agreement with

TR-PL measurements by Lee an co-workers that give a decay lifetime of τ =1.24 ns for the defect emission channel of a GaN-ZnO solid solution with a similar composition to the GZNO sample used in our study [34]. Further TR-XEOL work must be done on this material collecting streak images at many excitation energies across each absorption edge in order to provide a more quantitative assignment for the observed emission bands.

6.5 References

[1] A. Rogalev, and J. Goulon, in *Chemical Applications of Synchrotron Radiation*, Part II: X-ray Applications; Sham, T.K., Ed.; World Scientific: River Edge, NJ, 2002; Vol 12B, pp 707-760.

[2] T.K. Sham, D.T. Jiang, I. Coulthard, J.W. Lorimer, H.X. Feng, K.H. Tan, S.P. Frigo, R.A. Rosenberg, D.C. Houghton, and B. Bryskiewicz *Nature*, **363**, 331 (1993)

[3] R.A. Rosenberg, G.K. Shenoy, M.H. Chisholm, L.C. Tien, D. Norton, and S. Perton, *Nano. Lett.*, **7**, 1521 (2007)

[4] M.W. Murphy, X.T. Zhou, J.Y.P. Ko, F. Heigl, and T.K. Sham, *J. Chem. Phys.*, **130**, (2009)

[5] L. Liu, Y.M. Yiu, T.K. Sham, L. Zhang, and Y. Zhang, *J. Phys. Chem.* C, **114**, 6966 (2010)

[6] L. Liu, and T.K. Sham, *Small*, **8**, 2371 (2012)

[7] L. Armelao, F. Heigl, P.S.G. Kim, R.A. Rosenberg, T.Z. Reiger, and T.K. Sham, *J. Phys. Chem.* C, **116**, 14163 (2012)

[8]T.K. Sham, and R.A. Rosenberg, *ChemPhysChem*, **8**, 2557 (2007)

[9] L. Armelao, F. Heigl, S. Brunet, R. Sammynaiken, T. Reiger, R.I. Blyth, L. Zuin, R. Sankari, J. Vogt, and T.K. Sham, *ChemPhysChem*, **11**, 3625 (2010)

[10] K. Maeda, T. Takata, M. Hara, N. Saito, Y. Inoue, H. Kobayashi, and K. Domen, *J. Am. Chem. Soc.*, **127**, 8286 (2005)

[11] K. Maeda, K. Teramura, D. Lu, T. Takata, N. Saito, Y. Inoue, and K. Domen, *Nature*, **440**, 295 (2006)

[12] K. Maeda, and K. Domen, *J. Phys. Chem.* C, **111**, 7851 (2007)

[13] H.Y. Chen, L.P. Wang, J.M. Bai, J.C. Hanson, J.B. Waren, J.T. Muckerman, E. Fujita, and J.A. Rodriguez, *J. Phys. Chem.* C, **114** 1809 (2010)

[14] W.Q. Han, Z.X. Liu, and H.G. Yu, *Appl. Phys. Lett.*, **96**, 183112 (2010)

[15] M. Yashima, K. Maeda, K. Teramura, T. Takata, and K. Domen, *Chem. Phys. Lett.*, **416**, 225 (2005)

[16] W.Q. Han, M.J. Ward, and T.K. Sham, *J. Phys. Chem.* C, **115**, 3962 (2011)

[17] M.J. Ward, W.Q. Han, and T.K. Sham, *J. Phys. Chem.* C, **115**, 20507 (2011)

[18] T. Hirai, K. Maeda, M. Yoshida, J. Kubota, S. Ikeda, M. Matsumura, and K. Domen, *J. Phys. Chem.* C, **111**, 18853 (2007)

[19] K. Maeda, K. Teramura, and K. Domen, *J. Catal.*, **254**, 198 (2008)

[20] M. Yoshida, T. Hirai, K. Maeda, N. Saito, J. Kubota, H. Kobayashi, Y. Inoue, and K. Domen, *J. Phys. Chem.* C, **114**, 15510 (2010)

[21] F. Heigl *et al AIP Proceedings*, **CP879**, 1202, (2007)

[22] Y. Tanaka, T. Hara, H. Kitamura, and T. Ishikawa, *Nucl. Inst. Meth. A*, **467**, 1451 (2001)

[23] J.M. Vogt, J.C. Bergstrom, S. Hu,V. Poucki, and P. Lemut, *Proceedings of PAC09*, **TH6REP068**, 4111 (2009)

[24] T.Z. Regier, J.M. Vogt, R. Sammynaiken, and T.K. Sham, AIP Conf. Proc. 1234, 838 (2010)

[25] T. Reiger, J. Krochak, T.K. Sham, Y.F. Hu, J. Thompson, and R.I.R. Blyth, Nucl. Instrum. Methods Phys. Res., Sect. A, 582, 93 (2007)

[26] S.M. Heald, D.L. Brewe, E.A. Stern, K.H. Kim, F.C. Brown,; D.T. Jiang, E.D. Crozier, and R.A. Gordon, J. Synchrotron Rad., 6, 347 (1999)

[27] X.T. Zhou, F. Heigl, M.W. Murphy, T.K. Sham, T. Regier, I. Coulthard, and R.I.R Blyth, *App. Phys. Lett.*, **89**, 213109 (2006)

[28] W. Wei, Y. Dai, K. Yang, M. Guo, and B. Huang, *J. Phys. Chem.* C, **112**, 15915 (2008)

[29] M. Mapa, K.S. Thushara, B. Saha, P. Chakraborty, C.M. Janet, R.P. Viswanath, C.M. Nair, K.V.G.K. Murty, and C.S. Gopinath, *Chem. Mater.*, **21**, 2973 (2009)

[30] M. Hida, Y. Yan, S.H. Wei, and M. Al-Jassim, *Phys. Rev.* B, **78**, 195204 (2008)

[31] L. Li, J. Muckerman, M. Hybertsen, and P. Allen, *Phys. Rev.* B, **83**, 134202 (2011)

[32] E.J. McDermott, E.Z. Kurmaev, T.D. Boyko, L.D. Finkelstein, R.J. Green, K. Maeda, K. Domen, and A. Moewes, *J. Phys. Chem.* C, **116**, 7694 (2012)

[33] K. Maeda, and K. Domen, *Chem. Mater.*, **22**, 612 (2010)

[34] Y.C. Lee, T.Y. Lin, C.W. Wu, H. Teng, C.C. Hu, S.Y. Hu, and M.D. Yang, *J. Appl. Phys.*, **109**, 073506 (2011)

Chapter 7

7 Summary, Conclusions, and Future Directions

7.1 Summary

The aim of this research was the investigation of chemical (both bulk and surface), electronic, and optical properties of gallium nitride – zinc oxide (GaN-ZnO) solid solution nanostructures using X-ray absorption fine structure (XAFS), including both X-ray absorption near edge structure (XANES) and extended X-ray absorption fine structure (EXAFS), and X-ray excited optical luminescence (XEOL). In chapter 3 the effects of indium doping on the synthesis of GaN-ZnO nanostructures were studied using conventional methodologies (e.g., XRD, SEM, TEM, and EDX), XANES, and XEOL. To further the understanding of the optical luminescence properties and electronic structure of these complex materials a new two-dimensional (2D) XAFS–XEOL mapping technique, which is described in chapter 4, was developed and applied to the study of GaN-ZnO nanostructures. The effects of nitridation temperature on the chemical, electronic, and optical properties of GaN-ZnO nanocrystals were studied in chapter 5 using XANES, EXAFS, and XEOL. Chapter 6 describes the development of a new time-resolved (TR) XEOL technique using an optical streak camera, and the subsequent application of this technique to study near-band-gap emission from GaN-ZnO solid solution nanostructures.

7.2 Conclusions

Although GaN-ZnO solid solution systems have already been extensively studied, both experimentally and theoretically, the nature of local chemical environment, electronic structure, surface composition, and band-gap properties of these materials still remains unclear. The primary aim of this research was to address some of the questions about the nature of GaN-ZnO solid solutions, and in particular GaN-ZnO solid solution nanostructures. The most important findings of this study are presented in the following discussion which is organized such that it addresses each of the preceding questions about the nature of these materials individually.

7.2.1 Local Chemical Environment

The local chemical environment of GaN-ZnO solid solution nanostructures was investigated using XANES and EXAFS. It was determined that chemical disorder is caused by the formation of a solid solution of GaN and ZnO, which was evident from distortions observed in the near-edge region at the zinc and gallium $L_{3,2}$-edges in chapters 3 and 5. The local chemical environment of zinc and gallium, however, was consistent with that of GaN and ZnO respectively, which was observed from zinc and gallium *K*-edge XANES and EXAFS. The effects of doping the starting precursor with indium in an attempt to produce a GaInN-ZnO solid solution were studied using XANES and EXAFS in chapters 3 and 4. It was observed that indium doping not resultant in the formation of a GaInN-ZnO solid solution, instead, an extremely thin (i.e., subnanometer) indium oxide surface layer was formed. The incorporation of indium into the staring precursor did, however, result in an increase in chemical disorder of the resultant GaN-ZnO solid solution which was observed as a broadening of all near-edge features in the zinc and gallium $L_{3,2}$-edge XANES. It was determined that GaN-ZnO solid solutions exhibit strong short range chemical order around zinc and gallium centers, but, have diminished long range order which is particularly sensitive to nitridation temperature as observed in EXAFS studies of these materials in chapter 5. These observations suggest that the local chemical environment of these materials is such that there is a heterogeneous mixture of pure GaN and ZnO phases with very strong short range ordering and that a solid solution of GaN-ZnO forms at the phase interfaces of these local GaN and ZnO regions.

It appears that although the formation of a single phase GaN-ZnO solid solution has started in these materials, it has not gone fully to completion, which is possibly a function of the relatively short synthesis times. If synthesis times were lengthened to a period of days / weeks it is possible that the growth of single phase GaN-ZnO solid solutions would go to completion, however, this would result in a final product with a very low zinc content due to the volatilization of Zn (s) under the current synthesis conditions.

7.2.2 Electronic Structure

The band-gap energies of the GaN-ZnO solid solution nanostructures synthesized for this study were found to be in the visible region (i.e., less than 3 eV), but, optical emission from these materials was observed at lower energies (longer wavelengths) then their respective band-gaps. The electronic and optical properties of these materials were studied using XEOL. Broad XEOL emission bands were observed from these materials and tentatively assigned to the radiative recombination of electron–hole pairs with electrons on O donors and holes on Zn acceptors in the GaN-ZnO solid solution. The effect of indium doping on band-gap narrowing in GaN-ZnO solid solution nanostructures was studied in chapters 3 and 4. It was determined that the addition of indium to the synthesis precursor had no noticeable effect on the band-gap energy of the resultant solid solution, but, resulted in a blue-shift of the XEOL emission band. This blue-shift was determined to be the result of defect formation in the extremely thin (subnanometer) indium surface oxide which was identified using indium *K*-edge EXAFS. The efficiency of the optical decay channel in these materials was studied using a new 2D XAFS–XEOL mapping technique in chapter 4, which confirmed that the emission band observed from the GaN-ZnO sample grown using an indium doped precursor originated from the extremely thin indium surface oxide layer. The indium surface oxide was also observed to completely suppress optical emission from the bulk GaN-ZnO solid solution.

A red-shift with an increase in ZnO concentration, and thus, an increase in zinc concentration, was observed in XEOL emission bands from GaN-ZnO solid solution nanocrystals in chapter 5. This red-shift was explained as reflecting a greater energy distribution of Zn acceptor bands with an increase in Zn concentration in the solid solution, and thus, the formation of lower energy optical decay channels. An additional low energy (red) XEOL emission band was observed from GaN-ZnO nanocrystals synthesized at high nitridation temperature and was assigned electron–hole pair recombination from deeply trapped electrons and holes in the β-Ga_2O_3 surface oxide. It is possible that this emission band is suppressed at lower nitridation temperatures with the formation of a mixed Zn and Ga surface oxide.

The development of a new TR-XEOL apparatus employing an optical streak camera was described in chapter 6. This new TR-XEOL method was then applied to study the electronic structure of GaN-ZnO solid solution nanoparticles, and several new emission bands in the XEOL spectrum were temporally resolved. These emission bands were tentatively attributed to near-band-gap (NBG) emission from ZnO and GaN phases within the GaN-ZnO solid solution. Our preliminary assignment of these bands was based on their temporal response as a function of X-ray excitation energy, which was studied below, at resonance, and above the N and O *K*-edges and Zn and Ga L_3-edges. The use of a short decay lifetime window completely suppressed the broad low energy XEOL emission band observed from these materials using conventional un-gated XEOL spectroscopy.

The broad XEOL emission bands that are observed from GaN-ZnO nanostructures suggest that these materials are defect rich providing radiative recombination centers for photogenerated electrons and holes. Thus, these materials may have lower than desirable photocatalytic activity for overall water splitting. It may be possible to reduce the number of defects in these materials through the use of post-synthesis annealing or longer synthesis times. The observation of two NBG emission bands, attributed to ZnO and GaN phases respectively, suggest that these materials are better described as solid solution heterostructures, where GaN-ZnO solid solution formation at phase interfaces is responsible for controlling the energy of these bands. Thus, it may be better to think of these materials as heterogeneous mixtures of GaN and ZnO containing phase interface regions of GaN-ZnO solid solution.

7.2.3 Surface Composition

The local environment of nitrogen and oxygen in the surface and near-surface region of the GaN-ZnO nanostructures was examined using total electron yield (TEY) N and O *K*-edge XANES in chapters 3 and 5. We observed a GaN absorber environment for nitrogen in the near-surface region of all GaN-ZnO nanostructures with a broadening of all spectral features in the nitrogen *K*-edge, indicative of a decrease in crystallinity of the resultant solid solution, as the synthesis nitridation temperature was reduced. Features consistent with β-Ga_2O_3 were observed in the near-edge region of the oxygen *K*-edge for

all GaN-ZnO nanostructures. At lower nitridation temperatures a new feature was observed and assigned to O atoms in a surface ZnO phase. These findings suggest that as nitridation temperature is increased there is an increase in the concentration of near surface O/Ga atoms and a decrease in near surface Zn atoms which results in the formation of β-Ga_2O_3 surface oxide and the loss of ZnO surface oxide at higher synthesis temperatures. Additionally, nitrogen does not appear to participate in the local surface chemistry of the resultant GaN-ZnO nanostructures; instead it exists in the bulk of the solid solution retaining local GaN short range chemical order.

In order to produce a suitable photocatalyst for overall water splitting it is important to suppress surface recombination of photogenerated electrons and holes. From our observations GaN-ZnO solid solution nanostructures have a rich surface chemistry and preferentially form a gallium surface oxide layer at high synthesis temperature. It may be possible to further control the surface chemistry by increasing synthesis times which may allow single phase GaN-ZnO growth to proceed towards completion.

7.2.4 Origin of Band-Gap Narrowing

It has previously been suggested that band-gap narrowing observed in GaN-ZnO solid solutions is due to p–d repulsion between N 2p and Zn 3d states in the valence band which results in a shift of N 2p states to higher potential energy, and subsequently, an upward shift of the valence band maximum and a narrowing of the band-gap. Using a new TR-XEOL technique, which is described in chapter 6, we were able to temporally resolve two near-band-gap (NBG) emission bands from GaN-ZnO solid solution nanostructures. We tentatively assigned these two NBG components to ZnO and GaN phases within the GaN-ZnO solid solution. Our results are consistent with previous experimental and theoretical findings and suggest that band-gap narrowing observed in these materials is a result of repulsion between each phase's (GaN and ZnO) conduction band onset due to the proximity of unoccupied states at the phase interfaces, and not due to p–d repulsion between N 2p and Zn 3d states in the valence band. The possibility of a dual band-gap GaN-ZnO solid solution heterostructure would allow for further optimization of the band-gap and band-edge potentials, and thus, may lead to the

production of visible light driven photocatalysts for overall water splitting with both higher quantum efficiencies and photocatalytic activities.

7.2.5 General Conclusions

The motivation for this research was to increase our understanding of gallium nitride –zinc oxide solid solutions, which have been identified as potential materials for converting solar energy into chemical energy through the photocatalytic splitting of pure water into hydrogen and oxygen. If the level of control over the synthesis of these materials could be improved then it may be possible to produce highly active GaN-ZnO photocatalysts which could help solve the global energy crisis by producing hydrogen gas using water and sunlight. This research has answered some of the important questions about nature of this novel class of materials including their chemical, electronic, and optical properties. The information gained from our X-ray absorption studies of GaN-ZnO solid solutions has identified many areas in which these materials can be improved, and some of the challenges that they will present for future researchers. The development of several new synchrotron based X-ray excited optical luminescence (XEOL) techniques, including two-dimensional XAFS–XEOL mapping and time-resolved XEOL using an optical streak camera, have much broader applications in future studies of luminescent materials, and in particular luminescent semiconductors.

7.3 Future Directions

Although this XAFS and XEOL study has broadened the understanding of the electronic and chemical properties of GaN-ZnO solid solution nanostructures there are still many unanswered questions. Future work will include a scanning transmission X-ray microscopy (STXM) study of GaN-ZnO solid solution nanowires, a more detailed TR-XEOL analysis of the energy dependence of the luminescence decay lifetime, and a STXM investigation of GaN-ZnO thin films grown by pulsed laser deposition.

Since GaN-ZnO nanowires are thought to be single crystal structures a detailed study of the chemical environment and electronic structure at the nanoscale could provide new experimental insights into the formation of these materials [1]. STXM is capable of chemical imaging with a spatial resolution of ~30 nm [2]. Additionally nano-XANES

measurements can be performed at both surface and bulk regions of the GaN-ZnO nanowires allowing for the investigation of the local chemical and electronic environment of the surface and bulk [3]. Since the optical luminescence properties of these nanostructures appear to be of complex origin local chemical mapping and nano-XANES of the surface region would be beneficial to further understanding of the electronic structure and surface chemistry of these complex materials.

The existence of graphitic GaN-ZnO has been predicted theoretically and it has been suggested that the resultant material would be much softer and easier to wrap up into a nanotube than graphene [4]. The theoretical electronic and magnetic properties of graphitic GaN-ZnO nanoribbons have also been investigated and it was suggested that armchair nanoribbons would be nonmagnetic semiconductors and zigzag nanoribbons would be magnetic metals [5]. Future work will include the synthesis of thin films of GaN-ZnO grown via pulsed laser deposition and subsequent study of the resultant material by both conventional techniques (SEM, TEM, etc.) and STXM microscopy.

7.4 References

[1] W. Q. Han, Y. Zhang, C. Y. Nam, C. T. Black, and E. E. Mendez, *App. Phys. Lett.*, **97**, 083108 (2010)

[2] J. Zhou, J. Wang, H. Fang, C. Wu, J. N. Cutler, and T.K. Sham *Chem. Commun.*, **46**, 2778 (2010)

[3] Z. Q. Wang, J. Wang, T. K. Sham, and S. Yang, *J. Phys. Chem. C*, **116**, 10375 (2012)

[4] G. L. Chai, C. S. Lin, and W. D. Cheng, *J. Mater. Chem.*, **21**, 17071 (2011)

[5] G. L. Chai, C. S. Lin, and W. D. Cheng, *J. Mater. Chem.*, **22**, 7708 (2012)

Appendices

Appendix A: Copyright Release for Chapter 3 from the American Chemical Society

Copyright Clearance Center RightsLink®

Home | Account Info | Help

ACS Publications High quality. High impact.

Logged in as: Matthew Ward

LOGOUT

Title: Effect of Indium Doping on the Growth and Physical Properties of Ultrathin Nanosheets of GaInN/ZnO Solid Solution

Author: Wei-Qiang Han, Matthew James Ward, and TsunKong Sham

Publication: The Journal of Physical Chemistry C

Publisher: American Chemical Society

Date: Mar 1, 2011

Copyright © 2011, American Chemical Society

PERMISSION/LICENSE IS GRANTED FOR YOUR ORDER AT NO CHARGE

This type of permission/license, instead of the standard Terms & Conditions, is sent to you because no fee is being charged for your order. Please note the following:

- Permission is granted for your request in both print and electronic formats, and translations.
- If figures and/or tables were requested, they may be adapted or used in part.
- Please print this page for your records and send a copy of it to your publisher/graduate school.
- Appropriate credit for the requested material should be given as follows: "Reprinted (adapted) with permission from (COMPLETE REFERENCE CITATION). Copyright (YEAR) American Chemical Society." Insert appropriate information in place of the capitalized words.
- One-time permission is granted only for the use specified in your request. No additional uses are granted (such as derivative works or other editions). For any other uses, please submit a new request.

BACK | CLOSE WINDOW

Copyright © 2012 Copyright Clearance Center, Inc. All Rights Reserved. Privacy statement.
Comments? We would like to hear from you. E-mail us at customercare@copyright.com

Appendix B: Copyright Release for Chapter 4 from the American Chemical Society

Copyright Clearance Center RightsLink®

Home | Account Info | Help

ACS Publications High quality.high impact.

Logged in as:
Matthew Ward
LOGOUT

Title: 2D XAFS–XEOL Mapping of Ga1–xZnxN1–xOx Nanostructured Solid Solutions

Author: Matthew James Ward, Wei-Qiang Han, and Tsun-Kong Sham

Publication: The Journal of Physical Chemistry C

Publisher: American Chemical Society

Date: Oct 1, 2011

Copyright © 2011, American Chemical Society

PERMISSION/LICENSE IS GRANTED FOR YOUR ORDER AT NO CHARGE

This type of permission/license, instead of the standard Terms & Conditions, is sent to you because no fee is being charged for your order. Please note the following:

- Permission is granted for your request in both print and electronic formats, and translations.
- If figures and/or tables were requested, they may be adapted or used in part.
- Please print this page for your records and send a copy of it to your publisher/graduate school.
- Appropriate credit for the requested material should be given as follows: "Reprinted (adapted) with permission from (COMPLETE REFERENCE CITATION). Copyright (YEAR) American Chemical Society." Insert appropriate information in place of the capitalized words.
- One-time permission is granted only for the use specified in your request. No additional uses are granted (such as derivative works or other editions). For any other uses, please submit a new request.

BACK | CLOSE WINDOW

Copyright © 2012 Copyright Clearance Center, Inc. All Rights Reserved. Privacy statement.
Comments? We would like to hear from you. E-mail us at customercare@copyright.com

Appendix C: Copyright Release for Chapter 6 from the Institute of Physics

IOP Proceedings Licence

For papers published in our open access proceedings titles IOP Publishing no longer requires authors to sign and submit copyright forms. Our regular journals are unaffected by this change. Authors who wish to publish a paper in the following titles:

- *Journal of Physics: Conference Series* (JPCS)
- *IOP Conference Series: Materials Science and Engineering* (MSE)
- *IOP Conference Series: Earth and Environmental Science* (EES)

are asked to submit a paper only if all authors of the paper can agree in full to the terms of the licence. All papers submitted to us for publication in the above titles will be published according to the following terms and conditions.

Licence terms and conditions

By submitting your paper to the conference organizer, you, as author/representative of all the authors, grant a royalty free licence to IOP Publishing Limited (IOP) to use the copyright in the paper for the full term of copyright in all ways otherwise restricted by copyright, including the right to reproduce, distribute and communicate the article to the public and to make any other use which IOP may choose world-wide, by all means, media and formats, whether known or unknown at the date of submission, to the conference organizer.

This licence does not transfer the copyright in the paper as submitted which therefore remains with the authors or their employer, as appropriate. IOP encourages authors to use the paper in any way provided that, where possible, he/she displays citation information and the IOP Proceedings Licence Notice, for electronic use, best efforts are made to include a link to the online abstract in the journal and no author offers the paper to another publisher (prior to withdrawal or rejection) or includes it in another publisher's website.

However, a re-written and extended version of the paper may be published in another journal provided such re-use is within generally accepted ethical scientific limits and provided further citation information and the IOP Proceedings Licence Notice is displayed if possible, and for electronic use best efforts are made to include a link to the online abstract in the journal.

By granting this licence, the author warrants that the paper he/she is submitting is his/her original work, has not been published previously (other than in a research thesis or dissertation which fact has been notified to the conference organizer in writing), all named authors participated sufficiently in the conception and writing of the paper, have received a final version of the paper, agree to its submission and take responsibility for it,

and the submission has been approved as necessary by the authorities at the establishment where the research was carried out.

By granting this licence, the author also warrants that he/she acts on behalf of, and with the knowledge of, all authors of the paper, that the paper does not infringe any third party rights, it contains nothing libellous, all factual statements are, to the best of the authors' knowledge, true or based on valid research conducted according to accepted norms, and all required permissions have been obtained.

The IOP Proceedings Licence Notice

The IOP Proceedings Licence Notice should be displayed as:

“Published under licence in *Journal Title* by IOP Publishing Ltd.”

where *Journal Title* is one of:
Journal of Physics: Conference Series
IOP Conference Series: Materials Science and Engineering
IOP Conference Series: Earth and Environmental Science

Curriculum Vitae

Matthew James Ward

Department of Chemistry
University of Western Ontario
London, ON.
N6A 5B7

Education

2008 – Present* University of Western Ontario London, ON
Direct Entry PhD Physical Chemistry
*Expected Completion Date: December 2012

2004 – 2008 Carleton University Ottawa, ON
Honors BSc Chemistry

1995 – 1998* Queen's University Kingston, ON
BEng Electrical Engineering
*Not Conferred

Research Experience

The University of Western Ontario (2008 – Present)

- X-ray absorption fine structures (XAFS), X-ray excited optical luminescence (XEOL), and scanning transmission X-ray microscopy (STXM) of nanomaterials using facilities at both the Canadian Light Source (Saskatoon, SK) and the Advanced Photon Source (Argonne, IL)
- Development of time resolved X-ray excited optical luminescence (TR-XEOL) spectroscopy using an optical streak camera
- Development of two dimensional (2D) XAFS-XEOL mapping technique
- Synthesis, characterization, and spectroscopy of gallium nitride – zinc oxide solid solution semiconductors (bulk and nano), core-shell germanium – germanium oxide nanowires, and gallium nitride, zinc oxide, and germanium oxide nanomaterials
- Development of a multi-gas chemical vapor deposition (CVD) apparatus
- XAFS and XEOL of novel molecular germanium compounds
- Nanomaterial characterization using scanning electron microscopy (SEM), energy dispersive spectroscopy (EDS), X-ray diffraction (XRD), and transmission electron microscopy (TEM)
- Nanofabrication facility experience including clean room, microscopy, HF etching, and DC sputtering

Carleton University (2007-2008)

- Synthesis and characterization of new indium amidinate and guanidinate precursors for chemical vapor deposition (CVD) and atomic layer deposition (ALD) of indium tin oxide (ITO), indium oxide, and indium metal
- Air-free synthetic work using inert atmosphere glove boxes and Schlenk line techniques
- Precursor characterization using NMR, mass spectrometry, and crystallography
- Analysis of precursor suitability using TGA, DSC, sublimation, NMR thermolysis, and residual gas analysis (RGA)
- Deposition of aluminum oxide thin films using atomic layer deposition (ALD)
- Deposition of indium oxide and indium metal thin films using CVD
- Thin film characterization via elipsometry, X-ray diffraction, and scanning electron microscopy (SEM)

Publications

M.J. Ward, T.Z. Regier, J.M. Vogt, R.A. Gordon, W.Q. Han, and T.K. Sham "Time-Resolved X-ray Excited Optical Luminescence (TR-XEOL) using an Optical Streak Camera" *Journal of Physics: Conference Series* **2012**, Accepted.

M.J. Ward, J.G. Smith, T.Z. Regier, W.Q. Han, and T.K. Sham "2D XAFS-XEOL Spectroscopy – Some Recent Developments" *Journal of Physics: Conference Series* **2012**, Accepted.

M.J. Ward, P.A. Rupar, M.W. Murphy, Y.M. Yiu, K.M. Baines, and T.K. Sham "XAFS and XEOL of tetramesityldigermene – An electronic structure study of a heavy group 14 ethylene analogue" *Journal of Physics: Conference Series* **2012**, Accepted.

J. Smith, A. Akbari-Sharbaf, **M.J. Ward**, M.W. Murphy, G. Fanchini, and T.K. Sham "Luminescence Properties of Defects in Nanocrystalline ZnO" *J. Appl. Phys.* **2012**, JR12-10436, Submitted.

M.J. Ward, W.Q. Han, and T.K. Sham "2D XAFS-XEOL Mapping of $Ga_{1-x}Zn_xN_{1-x}O_x$ Nanostructured Solid Solutions" *J. Phys. Chem. C* **2011**, *115*, 20507.

S.T. Barry, P.G. Gordon, **M.J. Ward**, M.J. Heikkila, W.H. Monalis, G.P.A. Yap, M. Ritala, and M. Lesklä "Chemical vapour deposition of In_2O_3 thin films from a tris-guanidinate indium precursor" *Dalton Trans.* **2011,** *40,* 9425.

W.Q. Han, **M.J. Ward**, and T.K. Sham "Effect of Indium Doping on the Growth and Physical Properties of Ultrathin Nanosheets of GaInN/ZnO Solid Solution" *J. Phys. Chem. C* **2011,** *115,* 3962.

M.J. Ward, P.A. Rupar, M.W. Murphy, Y.M.Yiu, K.M. Baines and T.K. Sham "Ionic nature of Ge(II)-Centered dications: a germanium *K*-edge X-ray absorption near edge structures study" *Chem. Commun.* **2010,** *46,* 7016.

W. Han, D. Su, M. Murphy, **M. Ward**, T.K. Sham, L. Wu, Y. Zhu, Y. Hu, T. Aoki "Microstructure and electronic behavior of PtPd@Pt core-shell nanowires" *J. Mater. Res.* **2010,** *25,* 711.

L. Liu, J.Y.P. Ko, **M.J. Ward**, Y.M.Yiu, T.K. Sham and Y. Zhang "XANES and XEOL investigations of SiC microcrystals and SiC nanowires" *Journal of Physics: Conference Series* **2009,** *190,* 012134.

Technical Publications

M.J. Ward, J.Y.P. Ko, T.K. Sham "XANES: A Probe of Nanowire Surface Oxide Thickness -XANES and XEOL Study of Germanium Nanowires" 2009 *Canadian Light Source Activity Report,* p.120 (2010)

M.W. Murphy, L. Bovo, **M. Ward**, L. Armelao, and T.K. Sham "XANES Studies of $Zn_{1-x}Mn_xO$ Nanopowders" 2009 *Canadian Light Source Activity Report,* p.122 (2010)

T.Z. Regier , R. Sammynaiken, J.M. Vogt, **M. Ward**, T.K. Sham "Time Resolved X-ray Excited Optical Luminescence (TRXEOL) of Nanoscaled ZnO" 2009 *Canadian Light Source Activity Report,* p.126 (2010)

Posters and Presentations

M.J. Ward, P.A. Rupar, M.W. Murphy, Y.M. Yiu, K.M. Baines, T.K. Sham "XAFS and XEOL of tetramesityldigermene – An electronic structure study of a heavy group 14 ethylene analogue" Oral presentation at XAFS 15, Pullman Beijing West Wanda Hotel and Conference Center, (Beijing, China, 2012)

M.J. Ward, W.Q. Han, T.K. Sham "GaN-ZnO solid solution nanostructures for overall water splitting – An XAFS and XEOL study" Poster presentation at XAFS 15, Pullman Beijing West Wanda Hotel and Conference Center, (Beijing, China, 2012)

M.J. Ward, T.Z. Regier, J.M. Vogt, R.A. Gordon, W.Q. Han, T.K. Sham "Time-Resolved X-ray Excited Optical Luminescence (TR-XEOL) using an Optical Streak Camera" Oral presentation at SRI 2012, Lyon Convention Center, (Lyon, France, 2012)

M.J. Ward, J.G. Smith, T.Z. Regier, W.Q. Han, T.K. Sham "2D XAFS-XEOL Spectroscopy – Some Recent Developments" Oral presentation at SRI 2012, Lyon Convention Center, (Lyon, France, 2012)

M.J. Ward, W.Q. Han, and T.K. Sham; "$(Ga_{1-x}Zn_x)(N_{1-x}O_x)$ Nanostructures: Towards the Origin of Visible Luminescence via 2D XAFS-XEOL Spectroscopy" Oral presentation at CSC 2011 conference, Palais Des Congrès de Montréal, (Montreal, QC, 2011)

M.J. Ward, and T.K. Sham; "Germanium Nanowires: The Application of Synchrotron Radiation to the Study of Nanomaterials." Poster presented at VUVX 2010 conference, University of British Columbia (Vancouver, BC, 2010)

M.W. Murphy, L. Bovo, **M.J. Ward**, W. Diebel, L. Armelao, and T.K. Sham; "XANES Analysis of $Zn_{1-x}TM_xO$ (TM= Mn, Co, and Cr) Nanopowders: Effects of concentration and processing temperature on secondary phase formation and magnetism." Poster presented at XRMS 2010 conference, Rutherford Appleton Laboratories (Didcot, Oxfordshire, UK, 2010)

T.Z. Regier, **M. Ward**, J.M. Vogt, R. Sammynaiken, T.K. Sham; "Time Resolved X-ray Excited Optical Luminescence of Nanostructured Zinc Oxide" Poster presented at CSC 2010 conference, Metro Toronto Convention Center (Toronto, ON, 2010)

M.J. Ward, G.P.A. Yap and S.T. Barry; "Indium Guanidinates as Precursors for Chemical Vapour Deposition" Poster presented at Undergraduate Research Day 2008, Carleton University (Ottawa, ON, 2008)

M.J. Ward, G.P.A. Yap and S.T. Barry; "Development of Precursors for Atomic Layer Deposition of Tin doped Indium Oxide" Oral presentation at IDW 2007 conference, University of Toronto (Toronto, ON, 2007)

Awards and Honors

Ontario Graduate Scholar ($15 000)
University of Western Ontario (Provincial) – 2012-2013

Queen Elizabeth II Graduate Scholarship in Science and Technology ($10 000)
University of Western Ontario (Provincial) – 2011-2012

Graduate Thesis Research Award ($1300)
University of Western Ontario (Institutional) – 2012

Student Presentation Award – CSC 2011 ($300)
Canadian Society of Chemistry – Industrial Division (National) – 2011
$(Ga_{1-x}Zn_x)(N_{1-x}O_x)$ Nanostructures: Towards the Origin of Visible Luminescence via 2D XAFS-XEOL Spectroscopy

ASPIRE Award (~$1500)
University of Western Ontario (Institutional) – 2010

Ontario Graduate Scholar ($15 000)
University of Western Ontario (Provincial) – 2008-2009

Christian Sivertz Scholar ($3500)
University of Western Ontario (Institutional) – 2008

NSERC Undergraduate Student Research Award ($6500)
Carleton University (National) – 2008

VWR International Prize ($100)
Carleton Undergraduate Research Day 2008 (Institutional)

1st Place Poster Chemistry ($125)
Carleton Undergraduate Research Day 2008 (Institutional)

NSERC Undergraduate Student Research Award ($6500)
Carleton University (National) – 2007

Dr. Reginald T. Elworthy Award in Physical Chemistry ($2700)
Carleton University (Institutional) – 2006-2007

Teaching Experience

The University of Western Ontario

Chem 2214b – Physical Chemistry for Life Science
Laboratory Teaching Assistant – Winter 2012, 2011, 2010, and 2009

Chem 1200b – First Year Chemistry II
Resource Room Instructor – Winter 2012

Chem 1024 – Chemistry for Engineers
Laboratory Teaching Assistant – Fall 2011 and Winter 2010
Tutorial Instructor – Winter 2009

Chem 2214b – Physical Chemistry for Life Science
Redevelopment of experiments and laboratory manual – Fall 2010

Chem 1100a – First Year Chemistry
Tutorial Instructor – Fall 2010

Chem 1050 – First Year Chemistry
Tutorial Instructor – Fall 2009

Carleton University

Chem 1000 – First Year Chemistry
Laboratory Teaching Assistant – Fall 2007 - Winter 2008

Chem 1101 – Chemistry for Engineers
Laboratory Teaching Assistant – Fall 2007

Chem 2203 – Second Year Organic Chemistry
Laboratory Teaching Assistant –Winter 2006

Professional Development

Western Certificate in University Teaching and Learning (2012*):
An intensive multi-year program designed to enhance the quality of teaching by graduate students and prepare them for a future faculty career. The program focuses on the development of teaching, presentation, and group facilitation skills through workshops, classes, and mentorship sessions.
*Expected Completion Date: February 2013

Western Conference on Science Education (2011):
Volunteer and conference attendee at the Western Conference on Science Education: A national representation of post-secondary educators from across the disciplines of science and aligned areas sharing experiences, innovations, works in progress, and research and developing ideas related to teaching and learning in science higher education (University of Western Ontario, London, ON).

Quantitative Analysis of XANES (2010):
A three day workshop using FEFF9, FDMNES, and FITIT software platforms for the analysis and theoretical modeling of XANES spectra (VUVX 2010, Vancouver, BC).

Advanced Photon Source (APS) X-ray Absorption Fine Structures Summer School (2009):
An intensive five day workshop covering XAFS related topics including sample preparation, data collection, and data processing using the Athena and Artemis software packages (Argonne National Laboratory, Argonne, IL).

Graduate Courses

Chem 9724y – Materials Analysis Using Synchrotron Radiation
GS 9500 – The Theory and Practice of University Teaching (Pass With Distinction)
Chem 9658 – Chemistry Graduate Seminar
Physics 9826 – Surface Science
Geol 898.3 – Hard X-ray Microscopy
Chem 9721 – Topics in Advanced Main Group Chemistry
Chem 9754 – Structural Chemistry of Solid Materials